

# UNCLASSIFIED

AD NUMBER
ADB199063
NEW LIMITATION CHANGE
TO Approved for public release, distribution unlimited
FROM Distribution authorized to DoD and DoD contractors only; Critical Technology; FEB 1995. Other requests shall be referred to Naval Surface Warfare Center, Dahlgren Div., Dahlgren, VA 22448-5100.
AUTHORITY
Per document marking

THIS PAGE IS UNCLASSIFIED

**DAHLGREN DIVISION  
NAVAL SURFACE WARFARE CENTER**

Dahlgren, Virginia 22448-5100

---



**NSWCDD/TR-94/343**

**TARGET TRACKING FILTER STUDY FOR  
COMMAND-ALL-THE-WAY INTERCEPTS**

**S. A. HOFFMAN AND W. D. BLAIR  
SYSTEMS RESEARCH AND TECHNOLOGY DEPARTMENT**

**FEBRUARY 1995**

Approved for public release; distribution is unlimited.

*"Change 1 Inserted"*

## ABSTRACT

In Command-All-The-Way (CAW) interceptor guidance, an interceptor missile receives all acceleration commands from guidance laws in the weapons system at the launch platform, where a radar is used to track both the missile and the target. Since the missile uses no terminal homing in CAW, highly accurate state estimates of both the interceptor missile and the target are needed for the guidance algorithms to provide acceleration commands to the interceptor missile that are sufficiently accurate to ensure intercept of the target. An Interacting Multiple Model (IMM) algorithm is considered for tracking highly maneuvering targets for support of CAW intercepts. The IMM algorithm uses multiple models with model switching governed by an underlying Markov chain to better represent the target dynamics of maneuvering targets than a single model filter. Thus, using the output state estimate from the IMM algorithm will result in better acceleration commands from the guidance algorithm to the interceptor missile than that of a single model filter. The performance of the IMM algorithm and a single model Kalman filter are compared for both maneuvering and non-maneuvering targets. The simulation was executed for varying intercept ranges. The impacts of track filtering on the radar resource requirements and adjustments to the Proportional Navigation (PN) gain were also studied through simulation experiments and the results are summarized.

## CONTENTS

<u>Chapter</u>	<u>Page</u>
1 INTRODUCTION.....	1-1
2 SINGLE-MODEL TRACK FILTERING .....	2-1
3 IMM FILTERING ALGORITHM .....	3-1
4 MOTION MODELING FOR IMM ALGORITHM.....	4-1
5 WEAPONS CONTROL SYSTEM .....	5-1
FIRE CONTROL.....	5-1
INTERCEPTOR FILTER.....	5-2
GUIDANCE.....	5-2
RADAR DWELLS.....	5-4
6 INTERCEPTOR SIMULATION.....	6-1
AERODYNAMICS AND THRUST .....	6-1
TIME-TO-GO CALCULATION .....	6-2
LIMITATIONS .....	6-2
MISS DISTANCE CALCULATION .....	6-4
7 SIMULATION RESULTS.....	7-1
8 CONCLUSIONS.....	8-1
REFERENCES .....	9-1
<u>Appendix</u>	
A AERODYNAMIC DRAG ANALYSIS.....	A-1
DISTRIBUTION .....	(1)

## CHAPTER 1

### INTRODUCTION

In an autonomous weapon system engagement, the interceptor missile is fired and often receives a midcourse correction from the weapons control system (WCS) after its radar has acquired the missile. After receiving the midcourse correction, the missile's own sensors and autonomous homing devices take command of the missile for the completion of the intercept. This type of weapon system frees the radar and ship to direct its resources to other targets. However, sensors that provide autonomous homing within the missile are put under extreme stress and are expensive. The cost of a missile system can be reduced by eliminating the transmitter on the interceptor missile and maintaining only a receiver. Thus the missile would be changed from active to passive and shipboard illuminators would be used to illuminate the target. However, the illuminators are not always available or may not be operating properly. As a backup to the shipboard illuminators, a phased array radar tracks both the incoming target and the missile to provide all necessary information for the guidance algorithms of the missile. The challenge to this method is that it mandates better tracking of maneuvering targets than the more autonomous methods.

One of the more difficult problems in target tracking involves the use of a phased array radar to track multiple targets performing high-speed maneuvers. Many of the current systems use  $\alpha$ - $\beta$  and  $\alpha$ - $\beta$ - $\gamma$  filters with gains based on target range and data rate. The  $\alpha$ - $\beta$  and  $\alpha$ - $\beta$ - $\gamma$  filters are based on a discrete-time model for target motion. The discrete-time model is given by

$$X_k = F_{k-1}X_{k-1} + G_{k-1}\omega_{k-1} \quad (1.1)$$

$$Z_k = H_kX_k + v_k \quad (1.2)$$

where  $\omega_{k-1}$  is a process noise vector with  $\omega_{k-1} \sim N(0, Q_{k-1})$ ,  $v_k$  is a measurement error vector with  $v_k \sim N(0, R_k)$ ,  $X_k$  is the state vector, and  $Z_k$  is the measurement vector. One of the problems brought forth in these single-model filtering techniques is that the gains are either too high, which results from a high  $Q_k$  and gives poor noise reduction, or too low,

which results from a low  $Q_k$  and yields poor tracking performance during target maneuvers. To improve the accuracy of the state estimates of the single-motion model filter during target maneuvers, decision-directed techniques have been employed<sup>1</sup>. When tracking with a single-model filter and using a decision-directed approach for a maneuver response, an on-line assessment of filter performance is required to detect the presence of a maneuver. A common technique for assessing filter performance involves analyzing the filter residuals (i.e., the difference between the measurement and the predicted measurement) and declaring a maneuver when the residuals exceed a threshold. One decision-directed technique for tracking maneuvering targets increases the variance of the acceleration errors,  $Q_k$ , during a maneuver to reduce the bias in the state estimates. This technique has two major problems. First, the filter response is significantly delayed because the variance of the acceleration errors is not increased until the maneuver is detected. Second, after a target stops maneuvering, the decision to reduce the acceleration errors is often delayed because the filter with a large acceleration error variance may not have a detectable bias during or after the maneuver. Another technique for improving the accuracy of the state estimates is to increase the data rate during maneuvers<sup>2</sup>. However, adjusting the data rate with a single model filter has many of the same drawbacks as the variance adjustment technique when responding to maneuvers.

The need for decision-directed logic can be avoided by modeling the dynamics of the target with multiple models, where the model switching is a finite-state Markov chain. Such a system can be represented as

$$X_k = F_{k-1}(M_k)X_{k-1} + G_{k-1}(M_k)w_{k-1}(M_k) \quad (1.3)$$

with observations

$$Z_k = H_k(M_k)X_k + v_k(M_k) \quad (1.4)$$

where  $X_k$  is the system state and  $M_k$  is the model in effect during the sampling period ending at time  $t_k$ . The model  $M_k$  is one of  $n$  hypothesized models,  $M^1, \dots, M^n$ , for the system.

The optimal approach to estimating the state of the system in Eqs. (1.3) and (1.4) requires that every possible sequence of models from the initial observation through the most recent measurement be considered. Thus, for  $r$  models, the optimal approach requires  $r^k$  filters for processing the  $k^{th}$  observation. This is shown graphically in Figure 1-1 for the first three observations and two models, where open squares denote a model 1 update; the open circles denote a model 2 update; and  $X_{3|3}^{lj}$  denotes the state estimate for time  $t_3$  based on model  $l$  at  $t_1$ , model  $j$  at  $t_2$ , and model  $i$  at  $t_3$ . For the example in Figure 1-1, the

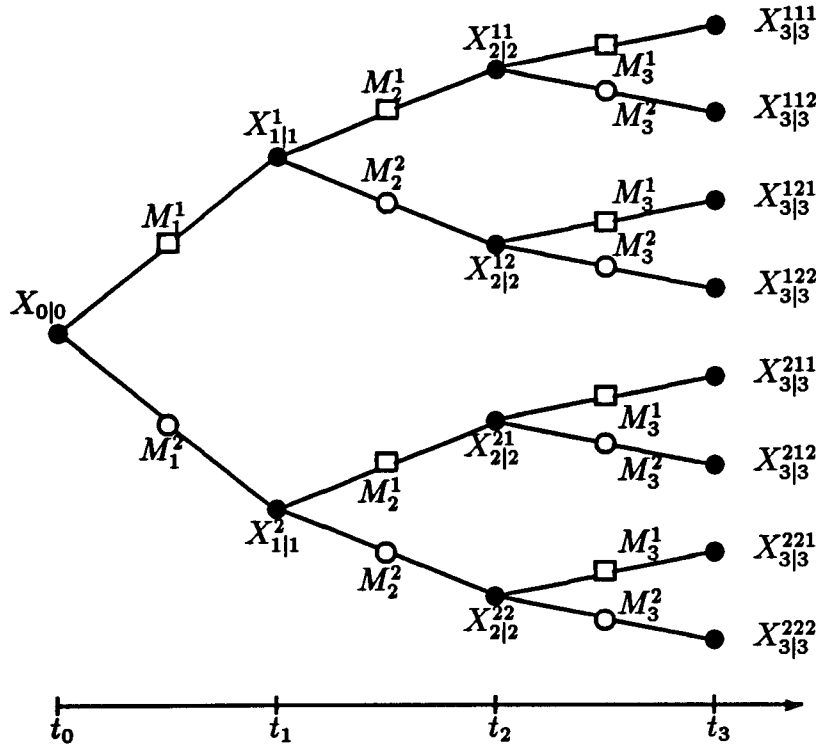


Figure 1-1. Optimal Approach To State Estimation

probability density  $f[\cdot]$  of the state given measurements  $Z^3 = \{Z_3, Z_2, Z_1\}$  is represented by

$$f[X_3|Z^3] = \sum_{i=1}^r \sum_{j=1}^r \sum_{l=1}^r f[X_3|M_3^i, M_2^j, M_1^l, Z^3] P\{M_3^i, M_2^j, M_1^l|Z^3\} \quad (1.5)$$

where  $P\{\cdot\}$  denotes probability, and  $M_k^j$  denotes model  $j$  at time  $k$ . The mean and error covariance are given by

$$X_{3|3} = \sum_{i=1}^r \sum_{j=1}^r \sum_{l=1}^r X_{3|3}^{lij} P\{M_3^i, M_2^j, M_1^l|Z^3\} \quad (1.6)$$

$$P_{3|3} = \sum_{i=1}^r \sum_{j=1}^r \sum_{l=1}^r P\{M_3^i, M_2^j, M_1^l|Z^3\} \left[ P_{3|3}^{lij} + (X_{3|3}^{lij} - X_{3|3})(X_{3|3}^{lij} - X_{3|3})^T \right] \quad (1.7)$$

Since  $r^k$  filters are required to process the  $k^{th}$  measurement, this optimal approach is not practical and efficient management of the multiple hypotheses is critical to limiting the computational requirements while maintaining performance capabilities. The Interacting Multiple Model (IMM) algorithm is an effective technique for hypothesis management<sup>3,4</sup>. The results of previous investigations indicate that the IMM algorithm is the superior technique for tracking maneuvering targets when the computational requirements and performance of

other techniques, such as the General Pseudo-Bayesian (GPB1 and GPB2) or Fixed Model, are considered<sup>4,5</sup>. The IMM consists of a filter for each model, a model probability evaluator, an estimate mixer at the input of the filters, and an estimate combiner at the output of the filters. The output state estimate is a probabilistic sum of the individual filter estimates and represents the relative performance of each model. The output error covariance also better reflects the tracking performance than a single-model filter because it is calculated to match the mixed Gaussian density based on the output of the individual filters. Studies have shown that the IMM algorithm provides a more flexible and accurate method of tracking maneuvering targets than single-model filters that need decision-directed logic<sup>6,7,8</sup>.

The focus of this report is the superiority of the performance of multiple-model filtering algorithms over that of single-model filters. This improvement in the filtered estimates of the target and the interceptor yields more accurate acceleration commands for the interceptor missile, which result in lower miss distances. In addition, the IMM algorithm requires fewer radar resources to achieve miss distances lower than that of single-model filters. A secondary focus of the report is Proportional Navigation guidance schemes that are used and their affect on the miss distance.

This report is organized in the following manner. First, in Chapter 2, the single model track filter is presented along with commonly used motion models. The IMM filtering algorithm and specialized motion models for the IMM algorithm are then discussed in Chapters 3 and 4, respectively. Chapter 5 describes the WCS used in the CAW simulation. A description of the target-interceptor simulation, including guidance and limitations, is given in Chapter 6. In Chapter 7, simulation results are presented to display the reduction of the miss distance achieved by incorporating two and three model IMM algorithms rather than single-model filters. The results of the simulation study suggest a potential for a large savings in cost if an interceptor missile, without the expense of a transmitter, were designed for CAW. Conclusions are also given in Chapter 8. The aerodynamic drag analysis performed for the interceptor missile model are given in Appendix A.



## CHAPTER 2

### SINGLE-MODEL TRACK FILTERING

The Kalman filter algorithm is commonly used to estimate the state and error covariance of the system given in Eqs. (1.1) and (1.2). The equations for the Kalman filter are outlined as follows:

Time Update:

$$X_{k|k-1} = F_{k-1}X_{k-1|k-1} \quad (2.1)$$

$$P_{k|k-1} = F_{k-1}P_{k-1|k-1}(F_{k-1})^T + G_{k-1}Q_{k-1}(G_{k-1})^T \quad (2.2)$$

Measurement Update:

$$S_k = H_k P_{k|k-1} (H_k)^T + R_k \quad (2.3)$$

$$K_k = P_{k|k-1} (H_k)^T (S_k)^{-1} \quad (2.4)$$

$$\tilde{Z}_k = Z_k - H_k X_{k|k-1} \quad (2.5)$$

$$X_{k|k} = X_{k|k-1} + K_k \tilde{Z}_k \quad (2.6)$$

$$P_{k|k} = [I - K_k H_k] P_{k|k-1} \quad (2.7)$$

where  $X_{i|l}$  and  $P_{i|l}$  denote the state estimate and error covariance at time  $i$  given measurements through time  $l$ . Two types of discrete-time models that are commonly used for target tracking are the Constant Velocity (CV) and Constant Acceleration (CA) models, which are given by

$$F_k = \begin{bmatrix} B_k & 0_{j \times j} & 0_{j \times j} \\ 0_{j \times j} & B_k & 0_{j \times j} \\ 0_{j \times j} & 0_{j \times j} & B_k \end{bmatrix} \quad G_k = \begin{bmatrix} D_k & 0_{j \times 1} & 0_{j \times 1} \\ 0_{j \times 1} & D_k & 0_{j \times 1} \\ 0_{j \times 1} & 0_{j \times 1} & D_k \end{bmatrix} \quad (2.8)$$

with

$$B_k^{CV} = \begin{bmatrix} 1 & T \\ 0 & 1 \end{bmatrix} \quad D_k^{CV} = \begin{bmatrix} 0.5T^2 \\ T \end{bmatrix} \quad (2.9)$$

$$B_k^{CA} = \begin{bmatrix} 1 & T & T^2/2 \\ 0 & 1 & T \\ 0 & 0 & 1 \end{bmatrix} \quad D_k^{CA} = \begin{bmatrix} T^3/6 \\ T^2/2 \\ T \end{bmatrix} \quad (2.10)$$

where  $j$  is the length of  $D_k$ . The state at time  $k$  is

$$X_k = [x_k \quad \dot{x}_k \quad y_k \quad \dot{y}_k \quad z_k \quad \dot{z}_k]^T \quad (2.11)$$

or

$$X_k = [x_k \quad \dot{x}_k \quad \ddot{x}_k \quad y_k \quad \dot{y}_k \quad \ddot{y}_k \quad z_k \quad \dot{z}_k \quad \ddot{z}_k]^T \quad (2.12)$$

where Eqs. (2.11) and (2.12) are used for the CV and CA models, respectively.

Radar measurements are in spherical coordinates while the tracking is usually performed in Cartesian coordinates. For spherical measurements, the measurement error covariance  $R_k$  can be approximated in Cartesian coordinates by

$$R_k = U \begin{bmatrix} \sigma_R^2 & 0 & 0 \\ 0 & R^2 \sigma_B^2 & 0 \\ 0 & 0 & R^2 \sigma_E^2 \end{bmatrix} U^T = U R_{RBE} U^T \quad (2.13)$$

where  $U$  is an orthogonal matrix given by

$$U = \begin{bmatrix} \cos E \sin B & \cos E \cos B & -\sin E \sin B \\ \cos E \cos B & -\cos E \sin B & -\sin E \cos B \\ \sin E & 0 & \cos E \end{bmatrix} \quad (2.14)$$

### CHAPTER 3

#### IMM FILTERING ALGORITHM

In the IMM approach to state estimation, the target dynamics are represented by multiple models that are each hypothesized to be correct. The output state estimate and error covariance are computed under each possible model hypothesis during the current sample period. For  $n$  models, a total of  $n$  hypotheses are considered through  $n$  filters operating in parallel with each filter using a different combination of the previous model-conditioned estimates. The IMM algorithm consists of a filter for each model, a model probability evaluator, an estimate mixer at the input of the filters, and an estimate combiner at the output of the filters. The block diagram of an IMM algorithm with two models is given in Figure 3-1, where  $X_{k|k}$  is the state estimate based on both models,  $X_{k|k}^j$  is the state estimate for time  $k$  based on model  $j$ ,  $\Lambda_k$  is the vector of model likelihoods at time  $k$ , and  $\mu_k$  is the vector of model probabilities at time  $k$  when all the likelihoods have been considered. With the assumption that the model switching is governed by an underlying Markov chain, the mixer uses the model probabilities and the model switching probabilities to compute a mixed estimate for each filter. At the beginning of a filtering cycle, each filter uses a mixed estimate and a measurement to compute a new estimate and a likelihood for the model within the filter. The likelihoods, prior model probabilities, and the model switching probabilities are then used to compute new model probabilities. The overall state estimate is then computed with the new state estimates and their model probabilities.

The IMM algorithm for filtering with  $n$  models is outlined in the following five steps.

#### Step 1: Mixing of the State Estimates

The filtering process starts with the prior state estimates  $X_{k-1|k-1}^i$ , state error covariances  $P_{k-1|k-1}^i$ , and the associated probabilities  $\mu_{k-1}^i$  for each model. The mixed state estimate for  $M_k^i$  is computed as

$$X_{k-1|k-1}^{0j} = \sum_{i=1}^n X_{k-1|k-1}^i \mu_{k-1}^{ij} \quad (3.1)$$

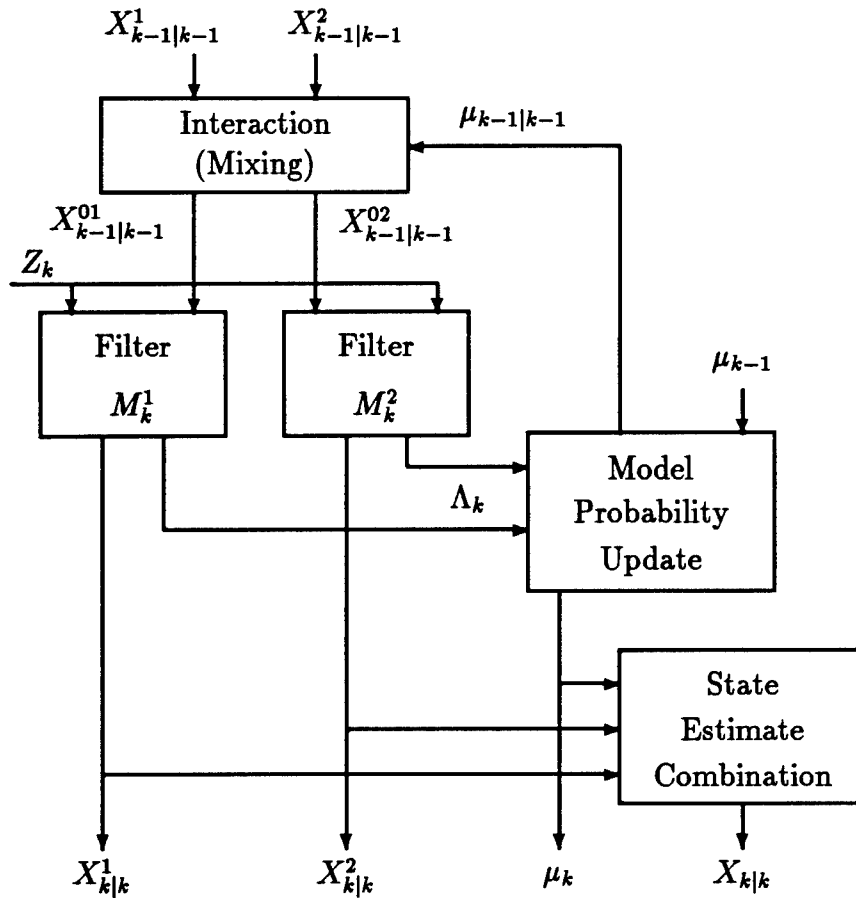


Figure 3-1. Block Diagram of the IMM Algorithm

where

$$\mu_{k-1|k-1}^{ij} = \frac{1}{\bar{c}_j} p_{ij} \mu_{k-1}^i \quad (3.2)$$

and the normalization constant  $\bar{c}_j$  is given by

$$\bar{c}_j = \sum_{i=1}^n p_{ij} \mu_{k-1}^i \quad (3.3)$$

and  $p_{ij}$  is the assumed transition probability for switching from model  $i$  to model  $j$ . The mixed covariance for  $M_k^j$  is computed as

$$P_{k-1|k-1}^{0j} = \sum_{i=1}^n \left[ P_{k-1|k-1}^i + (X_{k-1|k-1}^i - X_{k-1|k-1}^{0j})(X_{k-1|k-1}^i - X_{k-1|k-1}^{0j})^T \right] \mu_{k-1|k-1}^{ij} \quad (3.4)$$

#### Step 2: Model-Conditioned Updates

The Kalman filtering equations provide the model-conditioned updates. For  $M_k^j$

$$X_{k|k-1}^j = F_{k-1}^j X_{k-1|k-1}^{0j} \quad (3.5)$$

$$P_{k|k-1}^j = F_{k-1}^j P_{k-1|k-1}^{0j} (F_{k-1}^j)^T + G_{k-1}^j Q_{k-1}^j (G_{k-1}^j)^T \quad (3.6)$$

$$S_k^j = H_k^j P_{k|k-1}^j (H_k^j)^T + R_k^j \quad (3.7)$$

$$K_k^j = P_{k|k-1}^j (H_k^j)^T (S_k^j)^{-1} \quad (3.8)$$

$$\tilde{Z}_k^j = Z_k - H_k^j X_{k|k-1}^j \quad (3.9)$$

$$X_{k|k}^j = X_{k|k-1}^j + K_k^j \tilde{Z}_k^j \quad (3.10)$$

$$P_{k|k}^j = [I - K_k^j H_k^j] P_{k|k-1}^j \quad (3.11)$$

### Step 3: Model Likelihood Computations

The likelihood of  $M_k^j$  is computed with the filter residuals  $\tilde{Z}_k^j$ , the covariance of the filter residuals  $S_k^j$ , and the assumption of Gaussian statistics. The likelihood of  $M_k^j$  is given by

$$\Lambda_k^j = \frac{1}{\sqrt{\det(2\pi S_k^j)}} \exp[-0.5(\tilde{Z}_k^j)^T (S_k^j)^{-1} \tilde{Z}_k^j] \quad (3.12)$$

### Step 4: Model Probabilities Update

The model probabilities  $\mu_k^j$  are updated as

$$\mu_k^j = \frac{1}{c} \Lambda_k^j \bar{c}_j \quad (3.13)$$

where

$$c = \sum_{j=1}^n \Lambda_k^j \bar{c}_j \quad (3.14)$$

### Step 5: Combination of State Estimates

The state estimate and error covariance for output are given by

$$X_{k|k} = \sum_{j=1}^n X_{k|k}^j \mu_k^j \quad (3.15)$$

$$P_{k|k} = \sum_{j=1}^n \mu_k^j \left[ P_{k|k}^j + (X_{k|k}^j - X_{k|k})(X_{k|k}^j - X_{k|k})^T \right] \quad (3.16)$$

## CHAPTER 4

### MOTION MODELING FOR IMM ALGORITHM

In this report, two different combinations of models are considered for the IMM algorithm. The first IMM algorithm consists of a CV model and a CA model, which forms the CVCA track filter. A three-model IMM algorithm for tracking maneuvering targets is also used. The motion models are CV, Exponentially Increasing Acceleration (EIA), and three-dimensional turning rate (3DTR), and are combined to form the CVEIA3DTR track filter. A common configuration of the IMM algorithm is a CV model and two Constant Acceleration (2CA) models which forms the CV2CA filter. However, the CV2CA track filter does not provide the tracking performance attained by the CVEIA3DTR filter for many weapons control applications<sup>8</sup>. The elements of the CV model state are position and velocity as given in Eq. (2.11), while the elements for the CA, EIA, and 3DTR models are position, velocity, and acceleration as given in Eq. (2.12). The discrete-time CV model is given in Eq. (2.9), while the discrete-time CA model is given in Eq. (2.10). The EIA and 3DTR discrete-time models are given by

$$F_k^i = \begin{bmatrix} B_k^i & 0_{j \times j} & 0_{j \times j} \\ 0_{j \times j} & B_k^i & 0_{j \times j} \\ 0_{j \times j} & 0_{j \times j} & B_k^i \end{bmatrix} \quad G_k^i = \begin{bmatrix} D_k^i & 0_{j \times 1} & 0_{j \times 1} \\ 0_{j \times 1} & D_k^i & 0_{j \times 1} \\ 0_{j \times 1} & 0_{j \times 1} & D_k^i \end{bmatrix} \quad (4.1)$$

with

$$B_k^{EIA} = \begin{bmatrix} 1 & T & \alpha^{-2}(e^{\alpha T} - 1 - \alpha T) \\ 0 & 1 & \alpha^{-1}(e^{\alpha T} - 1) \\ 0 & 0 & e^{\alpha T} \end{bmatrix} \quad D_k^{EIA} = \begin{bmatrix} \alpha^{-3}(e^{\alpha T} - 1 - \alpha T - 0.5(\alpha T)^2) \\ \alpha^{-2}(e^{\alpha T} - 1 - \alpha T) \\ \alpha^{-1}(e^{\alpha T} - 1) \end{bmatrix} \quad (4.2)$$

$$B_k^{3DTR} = \begin{bmatrix} 1 & \omega^{-1}\sin(\omega T) & \omega^{-2}(1 - \cos(\omega T)) \\ 0 & \cos(\omega T) & \omega^{-1}\sin(\omega T) \\ 0 & -\omega\sin(\omega T) & \cos(\omega T) \end{bmatrix} \quad D_k^{3DTR} = \begin{bmatrix} 0.167T^3 \\ 0.5T^2 \\ T \end{bmatrix} \quad (4.3)$$

where  $j$  is the length of  $D_k^i$ . The  $\alpha$  is a positive constant corresponding to a "correlation time constant" for the acceleration and yields a model with a pole outside the unit circle. The  $\omega$  is a turning rate and is computed from the 3DTR state estimates as the magnitude of the acceleration divided by the speed of the target. A constant acceleration model can be attained with the EIA model or 3DTR model by setting the  $\alpha$  or  $\omega$  to a value much less

than one.

A kinematic constraint (KC) for constant speed targets can be used as additional information about the motion of constant speed, maneuvering targets to reduce the errors in the estimates due to the time-varying accelerations<sup>8,9</sup>. Using the KC tends to force the acceleration estimates to change in a manner that is consistent with the dynamics of the target. The speed of a target is given by

$$S = (\dot{x}^2 + \dot{y}^2 + \dot{z}^2)^{1/2} \quad (4.4)$$

For a target moving at constant speed

$$\frac{dS}{dt} = 0 \quad \text{or} \quad \dot{x}\ddot{x} + \dot{y}\ddot{y} + \dot{z}\ddot{z} = V \cdot A = 0 \quad (4.5)$$

where  $V$  and  $A$  are the target velocity and acceleration vectors, respectively. The KC is incorporated into the filter as a pseudomeasurement<sup>9</sup>. The pseudomeasurement equation is given by

$$\frac{V_{k|k}}{S_{k|k}} \cdot A_k + \mu_k = 0 \quad (4.6)$$

where

$$V_{k|k} = [\dot{x}_{k|k} \quad \dot{y}_{k|k} \quad \dot{z}_{k|k}] \quad S_{k|k} = (\dot{x}_{k|k}^2 + \dot{y}_{k|k}^2 + \dot{z}_{k|k}^2)^{1/2} \quad (4.7)$$

and  $\mu_k \sim N(0, R_k^\mu)$ . The  $\mu_k$  is a white Gaussian error process to account for the uncertainty in both  $V_{k|k}$  and the KC. Since the initial estimates of  $V_{k|k}$  may be poor,  $R_k^\mu$  is initialized with a very large value and allowed to decrease as

$$R_k^\mu = r_1(\delta)^k + r_0 \quad (4.8)$$

where  $0 < \delta < 1$ ,  $r_1$  is a constant chosen large for initialization, and  $r_0$  is a constant chosen for steady-state conditions.

The filtering equations for utilizing the KC are given below with  $X_{k|k}^c$  denoting the state estimate after the KC is applied, and  $P_{k|k}^c$  denoting the associated state error covariance. The filtering equations are followed by

$$X_{k|k}^c = [I - K_k^c C_k] X_{k|k} \quad (4.9)$$

$$P_{k|k}^c = [I - K_k^c C_k] P_{k|k} \quad (4.10)$$

where

$$K_k^c = P_{k|k} C_k^T [C_k P_{k|k} C_k^T + R_k^\mu]^{-1} \quad (4.11)$$

$$C_k = \frac{1}{S_{k|k}} [0 \quad 0 \quad \dot{x}_{k|k} \quad 0 \quad 0 \quad \dot{y}_{k|k} \quad 0 \quad 0 \quad \dot{z}_{k|k}] \quad (4.12)$$

Simulation results demonstrating the benefits of using the KC are given in References 8,9, and 10. When the KC is used in an IMM algorithm, it is applied to the state estimate and error covariance of a particular model after the mixing process and after the measurement update.



## CHAPTER 5

### WEAPONS CONTROL SYSTEM

The WCS includes fire control, the filter for the interceptor missile, the guidance algorithm, and an algorithm to determine the number of dwells for the radar. The WCS was modeled strictly for CAW intercepts. The CAW intercept zone ranged from roughly 20 km down to 13 km and is a user input for the simulation. The missile can be launched either vertically or have its body axis aligned with the vector created by the Predicted Intercept Point (PIP). In the simulation, if the missile is launched vertically, the missile must reach an altitude of 30 m before pitching over until its velocity vector is directed at the PIP. The missile continues its flight toward the initial PIP until it is acquired by the radar and can receive midcourse guidance commands. For the studies, radar acquisition of the missile occurs at a range of 2000 m.

#### FIRE CONTROL

For the purposes of the simulation studies, it is desirable to intercept the target at a specified range. In order for the intercept to occur at a specified range from the launch platform, both the time of flight for the interceptor missile to reach the desired intercept range,  $T_{int}$ , and the time of flight for the target to reach the desired intercept range,  $T_{tar}$  must be calculated. Once  $T_{tar} \leq T_{int}$ , an initial PIP is calculated and the interceptor is fired from the launch platform.  $T_{int}$  and  $T_{tar}$  are calculated as

$$T_{int} = \frac{R_{dir}}{V_{int}^{ave}} \quad (5.1)$$

$$T_{tar} = \frac{R_{k|k}^{tar} - R_{dir}}{V_{k|k}^{tar}} \quad (5.2)$$

where  $R_{dir}$  is the desired intercept range,  $V_{int}^{ave}$  is the average interceptor missile velocity during the sustain phase of flight,  $R_{k|k}^{tar}$  is the filtered estimate of the target range, and  $V_{k|k}^{tar}$

is the filtered estimate of the target velocity.

## INTERCEPTOR FILTER

Tracking of the interceptor is accomplished through the use of a CV Kalman filter where the time update takes into account the commanded acceleration of the missile. Thus, the time update equation for the filter, Eq.(2.1) was modified according to

$$X_{k|k-1} = F_{k-1}X_{k-1|k-1} + E_k\ddot{Y}_k^* \quad (5.3)$$

where

$$E_k = \begin{bmatrix} .5T^2 & 0 & 0 \\ T & 0 & 0 \\ 0 & .5T^2 & 0 \\ 0 & T & 0 \\ 0 & 0 & .5T^2 \\ 0 & 0 & T \end{bmatrix} \quad (5.4)$$

and  $\ddot{Y}_k^* = [\ddot{x}_k^* \ \ddot{y}_k^* \ \ddot{z}_k^*]^T$  is the commanded acceleration generated at the launch platform. Eqs. (2.2) to (2.7) of the Kalman filter equations remain unchanged.

## GUIDANCE

As previously stated, the Surface-to-Air-Missile (SAM) receives all acceleration commands from the WCS on the launching platform. The filtered estimates of both the target and the missile are then used to calculate the commanded acceleration using the following PN guidance law<sup>1</sup>. The commanded acceleration is calculated according to

$$\ddot{Y}^* = \frac{n}{R^4} \vec{R} \cdot \dot{\vec{R}} [(\vec{R} \cdot \dot{\vec{R}}) \vec{R} - R^2 \dot{\vec{R}}] \quad (5.5)$$

where  $\ddot{Y}^*$  is the commanded acceleration,  $n$  is a numerical gain, and  $\vec{R} = \vec{R}_t - \vec{R}_m$  is the position vector between the target and the missile. Eq. (5.5) gives an acceleration perpendicular to the line of sight of the target from the missile, which has a nonvanishing component in the direction of the missile velocity, and thus may require an input or a loss of energy. The numerical gain  $n$  determines how rapidly the missile will respond to a maneuver by the target. The greater the value of  $n$ , the larger the magnitude of the commanded accelerations  $\ddot{Y}^*$ , thus the missile responds more rapidly to a target maneuver. The missile receives more mild acceleration commands with a lower value of  $n$ . Maintaining a large  $n$  throughout the intercept may cause the missile to expend a significant amount of energy

responding to noisy measurements that appear to be target maneuvers. Therefore, methods to adjust the gain  $n$  are advantageous to minimize the amount of energy expended by the missile. In the simulation studies, the numerical gain  $n$  was set in numerous ways. In all cases,  $n$  was set to a constant until the time-to-go before intercept,  $T_{tgo}$ , reaches a set value,  $T_{set}$ , typically around 6 s. Five options for setting the value of  $n$  were considered. The first option involves leaving the numerical gain  $n$  constant for the entire intercept. The second option linearly increases the numerical gain from the constant value chosen  $n=n_{min}$  to some specified maximum value  $n=n_{max}$  as  $T_{tgo}$  goes from  $T_{set}$  to 0. The value of the numerical gain at some value  $T_{set} > T_{tgo} > 0$  was calculated as

$$n_{tgo} = -\left(\frac{n_{max} - n_{min}}{T_{set}}\right)T_{tgo} + n_{max} \quad (5.6)$$

The third option incorporates the idea that the target uses PN to guide toward its goal, which is assumed to be the launch platform. The acceleration of the target is usually limited so that it does not lose lock on its goal. By assuming PN for the target, a maximum acceleration of the target,  $A_{max}$ , and a numerical gain  $n = n_{tar}$  for the target, a cone in which the target may maneuver was defined. For the time in which  $T_{tgo} > T_{set}$ , the numerical gain of the interceptor remains relatively low so that it does not respond too rapidly to the target maneuvers since the target has to turn back to its goal and essentially into the interceptor missile. As  $T_{set} > T_{tgo} > 0$ , the numerical gain for the interceptor missile was linearly increased so that the interceptor will respond more rapidly in the end game. The assumed acceleration of the target needed to reach its goal was calculated as

$$\vec{A}_{tar} = \frac{n_{tar}}{R_0^4} \vec{R}_0 \cdot \dot{\vec{R}}_0 [(\vec{R}_0 \cdot \dot{\vec{R}}_0) \vec{R}_0 - R_0^2 \dot{\vec{R}}_0] \quad (5.7)$$

where  $n_{tar}$  is an assumed value of the numerical gain of the target, and  $\vec{R}_0 = \vec{R}_t - \vec{R}_l$  is the position vector between the target and the launch platform. The numerical gain for the interceptor missile varies according to the acceleration needed by the target to reach its goal. Based on the premise that the higher the acceleration needed by the target to reach its goal, the more likely the target is to maneuver toward the goal to not place itself outside its structural or seeker limitations. As the acceleration needed by the target increases, the numerical gain of the interceptor will be maintained at a low level, knowing that the target has to turn towards the launch platform, and towards the interceptor missile. However, in the end-game, the numerical gain of the interceptor is increased to be prepare the interceptor for any last second maneuver by the target. A method by which the numerical gain of the interceptor increases as a function of the square of the ratio of  $\|\vec{A}_{tar}\|$  to some assumed

maximum acceleration  $A_{max}$  was selected. For  $T_{tgo} > T_{set}$ , the numerical gain for the interceptor missile was calculated as

$$n_0 = (n_{max} - n_{min}) \left( \frac{\|\vec{A}_{tar}\|}{A_{max}} - 1 \right)^2 + n_{min} \quad (5.8)$$

where  $n_{max}$  and  $n_{min}$  were a preset maximum and minimum value of the numerical gain  $n$ , respectively.

Once  $T_{set} > T_{tgo} > 0$ , the numerical gain calculated in Eq. (5.8) is increased in the following manner to respond more quickly to target maneuvers in the end game. Thus,

$$n_{tgo} = -\left( \frac{n_{max} - n_0}{T_{set}} \right) T_{tgo} + n_{max} \quad (5.9)$$

The last two options for the numerical gain  $n$  are restricted to use with the IMM filtering algorithm and is based on the model probability of the nonmaneuvering, CV, model. In essence, when the CV model probability is high, the target is not likely to be maneuvering and a low value of  $n$  is used. In contrast, when the CV model probability is low, the target is likely to be maneuvering, and a high value of  $n$  is used.

The fourth option calculates  $n$  as a linear function of the CV model probability. The numerical gain is then calculated as

$$n = -(n_{max} - n_{min})\mu_{cv} + n_{max} \quad (5.10)$$

where  $\mu_{cv}$  is the CV model probability.

The final option uses the same premise as the fourth option, but rather than a linear function of the CV model probability, a cosine function is used. This was chosen to allow the numerical gain  $n$  to maintain a lower value when the CV model probabilities are dominant than the linear function given in Eq. (5.10). In addition, the numerical gain  $n$  will increase more rapidly when the CV model probability is not dominant. The calculation for the numerical gain is

$$n = n_{min} + \Delta n \quad (5.11)$$

where

$$\Delta n = (\cos(\mu_{cv}\pi) + 1) \frac{(n_{max} - n_{min})}{2} \quad (5.12)$$

RADAR DWELLS

The radar has specified standard deviations in the measurements of range, bearing and elevation. To reduce the effective measurement errors, the number of dwells on the target,  $N$ , can be increased and the resultant measurement is the average of the  $N$  dwells. This can be particularly advantageous in the end game where the inaccuracies of the tracking when using only single dwell measurements may not provide acceleration commands with sufficient accuracy to ensure a successful intercept. In the simulation, several techniques for choosing the number of dwells to be used were available to the user. The first option involved maintaining single dwell measurements for the entire intercept. For the second option, the number of dwells can be calculated so that the covariance of the  $c$  component of the predicted intercept point,  $\sigma_{fc}^2$ , is below a specified value.

The number of dwells was increased only in the end game. The number of dwells were initially increased to bring the filtered error covariance down linearly from the initial value at time  $T_{set} + 1$  s to a level that provides a  $\sigma_{fc}^2 = (10r_{min})^2$  at time  $T_{set}$ , where  $r_{min}$  is a desired standard deviation of the miss distance at intercept (e.g.,  $r_{min} = 2$  m). Once  $T_{tgo} < T_{set}$ , the number of dwells are increased to bring the predicted positional error covariance down quadratically from the value of  $(10r_{min})^2$  at time  $T_{set}$  to  $r_{min}^2$  at intercept. Thus, for the time  $T_{set} < T_{tgo} \leq T_{set} + 1$ , the calculated value of the filtered variance of the predicted position,  $\sigma_{fc}^2$ , for each coordinate is calculated as

$$\sigma_{fc}^2 = \left( (\sqrt{P_{k|k_c}^i} - 10r_{min})(T_{tgo} - T_{set}) + 10r_{min} \right)^2 \quad (5.13)$$

where  $P_{k|k_c}^i$  is the initial positional element of the filtered error covariance for each coordinate at the first data point at time  $T_{tgo} = T_{set} + 1$ . For the time  $0 < T_{tgo} \leq T_{set}$ , it was desired to bring down the value of  $\sigma_{fc}^2$  quadratically to a value of  $(10r_{min})^2$  at time  $T_{set}$ . Thus,  $\sigma_{fc}^2$  for each coordinate is calculated as

$$\sigma_{fc}^2 = \left( (10r_{min} - r_{min}) \left( \frac{T_{tgo}}{T_{set}} \right)^3 + r_{min} \right)^2 = \left( 9r_{min} \left( \frac{T_{tgo}}{T_{set}} \right)^3 + r_{min} \right)^2 \quad (5.14)$$

To calculate the number of dwells, the predicted error covariance matrix for each coordinate,  $P_{k|k-1}^c$ , is defined as

$$P_{k|k-1}^c = \begin{bmatrix} p_{11} & p_{12} \\ p_{12} & p_{22} \end{bmatrix} \quad (5.15)$$

The gain  $K_k^c$  is then calculated as

$$K_k^c = P_{k|k-1}^c H_k^T [H_k P_{k|k-1}^c H_k^T + \frac{\sigma_v^2}{N_c}]^{-1} \quad (5.16)$$

where  $N_c$  is the number of dwells, and  $H_k = [1 \ 0]$ . Substituting Eq. (5.15) and  $H_k$  into Eq. (5.16),  $K_k^c$  is found to be

$$K_k^c = \frac{1}{p_{11} + \sigma_v^2/N_c} \begin{bmatrix} p_{11} \\ p_{12} \end{bmatrix} \quad (5.17)$$

Knowing the measurement update equation for the error covariance as defined in Eq. (2.7), the filtered error covariance  $P_{k|k}$  can be predicted forward in time by  $T_{tgo}$ . Needing only the positional element of the predicted covariance, the following equation is obtained

$$\begin{bmatrix} 1 & T_{tgo} \end{bmatrix} P_{k|k} \begin{bmatrix} 1 \\ T_{tgo} \end{bmatrix} = \begin{bmatrix} 1 & T_{tgo} \end{bmatrix} \left( [I - K_k H_k] P_{k|k-1}^c \right) \begin{bmatrix} 1 \\ T_{tgo} \end{bmatrix} \quad (5.18)$$

The left hand side of Eq. (5.18) is the calculated value of the predicted error covariance  $\sigma_{fc}^2$  as defined in Eqs.(5.13) and (5.14) and dependent on  $T_{tgo}$ . The right hand side of Eq. (5.18) is calculated to be

$$\sigma_{fc}^2 = p_{11} - \frac{p_{11}^2}{p_{11} + \sigma_v^2/N_c} + 2T_{tgo} \left( p_{12} - \frac{p_{11}p_{12}}{p_{11} + \sigma_v^2/N_c} \right) + T_{tgo}^2 \left( p_{22} - \frac{p_{12}^2}{p_{11} + \sigma_v^2/N_c} \right) \quad (5.19)$$

Rearranging Eq. (5.19), the number of dwells for each coordinate is calculated as

$$N_c = \sigma_v^2 \left( \frac{p_{11} + 2T_{tgo}p_{12} + T_{tgo}^2p_{22} - \sigma_{fc}^2}{T_{tgo}^2(p_{12}^2 - p_{11}p_{22}) + p_{11}\sigma_{fc}^2} \right) \quad (5.20)$$

Setting  $\sigma_v^2 = \sigma_a^2 R_{k|k-1}^2$  where  $\sigma_a$  is the standard deviation of the angular measurement error and  $R_{k|k-1}$  is the predicted range, the number of dwells for the next measurement is the maximum of the three calculated values ( $N_x, N_y, N_z$ ) rounded up to the nearest integer.

The preceding equations generate the number of dwells for a CV track filter. For a track filter where target accelerations are estimated, the predicted error covariance matrix for each coordinate,  $P_{k|k-1}^c$ , is defined as

$$P_{k|k-1}^c = \begin{bmatrix} p_{11} & p_{12} & p_{13} \\ p_{12} & p_{22} & p_{23} \\ p_{13} & p_{23} & p_{33} \end{bmatrix} \quad (5.21)$$

Substituting Eq. (5.21) into Eq. (5.16), the gain  $K_k^c$  is found to be

$$K_k^c = \frac{1}{p_{11} + \sigma_v^2/N_c} \begin{bmatrix} p_{11} \\ p_{12} \\ p_{13} \end{bmatrix} \quad (5.22)$$

The filtered error covariance  $P_{k|k}$  is then predicted forward in time by  $T_{tgo}$ . Needing only the positional element of the predicted covariance,

$$\begin{bmatrix} 1 & T_{tgo} & .5T_{tgo}^2 \end{bmatrix} P_{k|k} \begin{bmatrix} 1 \\ T_{tgo} \\ .5T_{tgo}^2 \end{bmatrix} = \begin{bmatrix} 1 & T_{tgo} & .5T_{tgo}^2 \end{bmatrix} \left( [I - K_k H_k] P_{k|k-1}^c \right) \begin{bmatrix} 1 \\ T_{tgo} \\ .5T_{tgo}^2 \end{bmatrix} \quad (5.23)$$

The left hand side of Eq. (5.23) is  $\sigma_{f_c}^2$  as defined in Eqs. (5.13) and (5.14) and dependent on  $T_{tgo}$ . The right hand side of Eq. (5.23) is calculated to be

$$\sigma_{f_c}^2 = p_{11} - \frac{p_{11}^2}{p_{11} + \sigma_v^2/N_c} + 2T_{tgo} \left( p_{12} - \frac{p_{11}p_{12}}{p_{11} + \sigma_v^2/N_c} \right) + T_{tgo}^2 \left( p_{22} + p_{13} - \frac{p_{11}p_{13} + p_{12}^2}{p_{11} + \sigma_v^2/N_c} \right) + \dots$$

$$T_{tgo}^3 \left( p_{23} - \frac{p_{12}p_{13}}{p_{11} + \sigma_v^2/N_c} \right) + \frac{T_{tgo}^4}{4} \left( p_{33} - \frac{p_{13}^2}{p_{11} + \sigma_v^2/N_c} \right) \quad (5.24)$$

Rearranging Eq. (5.24), the number of dwells for each coordinate is calculated as

$$N_c = \sigma_v^2 \left( \frac{p_{11} + 2T_{tgo}p_{12} + T_{tgo}^2(p_{22} + p_{13}) + T_{tgo}^3p_{23} + T_{tgo}^4(p_{33}/4) - \sigma_{f_c}^2}{T_{tgo}^2(p_{12}^2 - p_{11}p_{22}) + T_{tgo}^3(p_{12}p_{13} - p_{11}p_{23}) + T_{tgo}^4(p_{13}^2 - p_{11}p_{33})/4 + p_{11}\sigma_{f_c}^2} \right) \quad (5.25)$$

Setting  $\sigma_v^2 = \sigma_a^2 R_{k|k-1}^2$ , the number of dwells for the next measurement is the maximum of the three calculated values ( $N_x, N_y, N_z$ ) rounded up to the nearest integer. When tracking with the IMM algorithm, the number of dwells for each coordinate is calculated under each model and is weighted by the model probabilities. Thus,

$$N_c = \sum_{j=1}^n \mu_j N_c^j \quad (5.26)$$

where  $N_c^j$  is the number of dwells for model  $j$  in coordinate  $c$ .

The third option sets the number of dwells to 10 for the duration of the time  $T_{tgo} \leq T_{set}$ . The fourth option is limited in application to the IMM algorithms. Using the model probabilities, the number of dwells can be adjusted according to whether or not the model probabilities suggest that the target is maneuvering or not maneuvering over the time interval  $T_{tgo} \leq T_{set}$ . The number of dwells,  $N$ , is set to  $N = 4$  when the model probability of the non-maneuvering model, CV model, is  $\mu_{cv} > .5$ , otherwise  $N = 10$ .

## CHAPTER 6

### INTERCEPTOR SIMULATION

The target-interceptor simulation is representative of an intercept of an airborne target by a surface-to-air missile (SAM). The SAM can either be launched vertically or be pointed in the direction of the PIP. Since the onboard homing devices of the SAM remain inactive, it receives all acceleration commands from guidance laws computed within the weapons system, where the target and missile states are estimated from the phased array radar measurements of their positions.

#### AERODYNAMICS AND THRUST

The aerodynamics of the missile are limited to the aerodynamic drag of the missile body. The drag created by the winglets and control surfaces are not taken into account. The drag on the missile body is evaluated for subsonic, transonic, and supersonic flow. The calculation of the force of drag includes skin friction drag, forebody pressure drag, base pressure drag, and the drag due to lift. A complete study of the drag calculations are presented in the appendix. The thrust profile of the interceptor is defined by a boost phase of 9 s with a thrust of 15000 lb., and a sustain phase of 35 s with a thrust of 5000 lb.

The trajectory of the missile is calculated from the acceleration commands, the acceleration due to the thrust, and the acceleration due to the drag using a fourth-order Runge-Kutta technique. With the thrust profile and calculated accelerations due to drag, the interceptor has an average velocity of 700 m/s at intercept. The skid-to-turn autopilot (i.e., no rolling motion) for the SAM is defined by

$$A_p = \ddot{Y}_k^*(1 - F) + \ddot{Y}_{k-1}(F) \quad (6.1)$$

$$F = e^{(-dt/(2T_p))} \quad (6.2)$$

where  $\ddot{Y}_k^* = [\ddot{x}_k^* \quad \ddot{y}_k^* \quad \ddot{z}_k^*]^T$  is the commanded acceleration,  $A_p$  is the predicted acceleration of the missile,  $\ddot{Y}_{k-1}$  is the measured acceleration at time  $k-1$ ,  $dt$  is the integration step size,



and  $T_p$  is the autopilot time constant for the SAM.

## TIME-TO-GO CALCULATION

For several of the parameters previously discussed, the time-to-go,  $T_{tgo}$ , before intercept is required. The filtered positional and velocity estimates were used to calculate  $T_{tgo}$ .  $T_{tgo}$  is calculated as

$$T_{tgo} = \frac{\|\vec{R}\|}{\|\vec{V}_{tm}\|} \quad (6.3)$$

where  $\vec{R} = \vec{R}_t - \vec{R}_m$  is the position vector between the target and the missile, and  $\vec{V}_{tm}$  is the relative velocity vector of the target to the missile. This vector is calculated as

$$\|\vec{V}_{tm}\| = \|\vec{V}_t\|\cos\theta_t + \|\vec{V}_m\|\cos\theta_m \quad (6.4)$$

where  $\vec{V}_t$  and  $\vec{V}_m$  are the velocity vectors of the target and missile, respectively, and  $\theta_t$  and  $\theta_m$  are the headings of the target and missile with respect to the range vector between the target and the interceptor, respectively. The headings are found through the following equations

$$\cos\theta_t = -\frac{(\vec{V}_t \cdot (\vec{R}_t - \vec{R}_m))}{\|\vec{V}_t\| \|\vec{R}_t - \vec{R}_m\|} \quad (6.5)$$

$$\cos\theta_m = -\frac{(\vec{V}_m \cdot (\vec{R}_m - \vec{R}_t))}{\|\vec{V}_m\| \|\vec{R}_t - \vec{R}_m\|} \quad (6.6)$$

## LIMITATIONS

A limitation that needs to be placed on the interceptor missile is the structural limitation of the airframe. This is accomplished through the use of a maximum acceleration of the missile,  $g_{max}$ . The magnitude of the commanded accelerations is tested against the maximum to ensure that it does not exceed the maximum allowed. If the magnitude of the commanded acceleration exceeds the maximum, the commanded acceleration  $\ddot{Y}^*$  is reset to

$$\ddot{Y}^* = g_{max} \frac{\ddot{Y}_i^*}{\|\ddot{Y}_i^*\|} \quad (6.7)$$

where  $\ddot{Y}_i^*$  is the initial commanded acceleration which would have exceeded the maximum allowed.

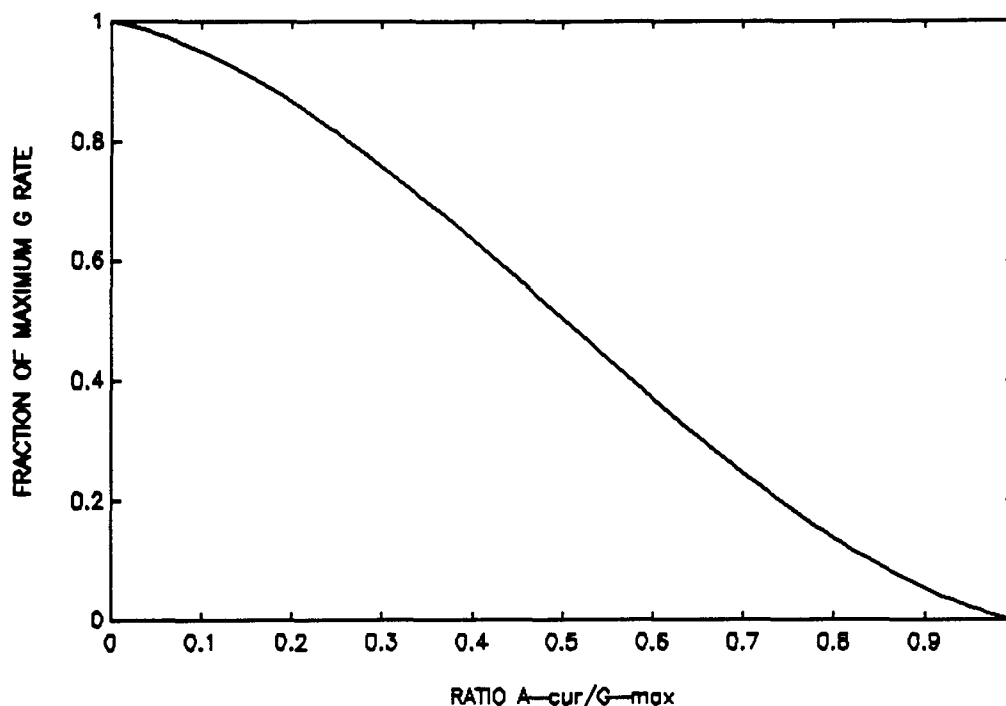


Figure 6-1. "g" rate polynomial

Even if the commanded accelerations are set to some maximum, the missile may already be pulling several "g's" in a sharp turn towards the target, and the application of the commanded accelerations may exceed that which the missile is capable. To accommodate this possibility, a function that describes an acceleration rate, or "g" rate, for the missile when the missile is currently performing a stressful maneuver was developed. For the simulation, the "g" rate was designed as a third-order polynomial, which limits the "g's" the missile can pull as a function of the magnitude of the current missile acceleration. The third-order polynomial used for the simulation is graphed in Figure 6-1 and is found to be

$$\dot{g}_{cur} = \dot{g}_{max}(1.83A_{rat}^3 - 2.56A_{rat}^2 - 0.27A_{rat} + 1) \quad (6.8)$$

$$A_{rat} = \frac{||\vec{A}_{cur}||}{g_{max}} \quad (6.9)$$

where  $||\vec{A}_{cur}||$  is the magnitude of the current acceleration,  $\dot{g}_{max}$  is the maximum "g" rate achievable by the missile when in unaccelerated flight, and  $\dot{g}_{cur}$  is the current achievable "g" rate. By implementing Eq. (6.8), the achievable "g" rate of the missile is zero when the missile is currently pulling its limit of  $g_{max}$ .

In addition to the structural limitation of the missile, an aerodynamic limitation is also placed on the missile. The angle of attack  $\alpha$ , the angle between the relative wind and the

roll axis in the body frame of the missile, is limited to 35 deg. The aerodynamic qualities of the missile are discussed in more detail in the appendix.

## MISS DISTANCE CALCULATION

The termination of the intercept simulation occurs when the range of the interceptor missile exceeds that of the target. To determine the miss distance between the interceptor and target, a discrete-time, constant acceleration model is executed at the time interval of  $dt=1/1000$  s on both the true interceptor state and the true target state over the period of time that the relative range between the target and the interceptor is less than 2000 m. At each of the time increments, the relative range between the target and the interceptor is calculated. The miss distance is determined to be the minimum of the calculated values of the relative range.

## CHAPTER 7

### SIMULATION RESULTS

Performance comparisons that include the CVCA with the kinematic constraint, the CVEIA3DTR with the kinematic constraint, the CV track filter, and the CV track filter switching to the CA track filter at  $T_{tgo} = T_{set}$  are presented. Four separate targets were examined where the desired intercept point ranged from approximately 7 to 20 km. The first target was a constant height, constant velocity target as shown in Figure 7-1 (please note that all figures are given at the end of the text). The velocity of the target was set to 300 m/. The second target was a constant height, mildly weaving target, where the maximum peak accelerations were approximately 5 m/s<sup>2</sup>. The second target is displayed in Figure 7-2. The third target and fourth targets are representative of more maneuverable targets. The third target, shown in Figure 7-3, performs nearly constant speed weaves with peak accelerations of 30 m/s<sup>2</sup>. The fourth target is representative of a high speed, highly maneuverable target. The fourth target has a velocity of approximately 600 m/s and performs a weaving maneuver with accelerations of 60 m/s<sup>2</sup>, as shown in Figure 7-4.

The third and fourth targets were evaluated on the basis of finding the most difficult point along the trajectory to intercept. The most difficult point to intercept is the point which causes the interceptor missile to perform the most stressful maneuver to intercept the target. The most difficult point to intercept for each of the respective trajectories is displayed in Figure 7-5. The graphs in Figure 7-5 are just a portion of the entire trajectory, the point at which the weaves are initiated is marked to obtain a sense of scale. Point A represents the most difficult point to intercept for both targets. To obtain the most difficult point along the target trajectory to intercept, numerous intercept simulations along the target trajectory were executed. The positions of these points are rather intuitive. For a given interceptor missile and target, the most stress is induced on the missile by the guidance system when the angle between the velocity vector of the interceptor missile and the PIP is at its greatest. For both the third and fourth targets, when the target has completed a turn and begins the next turn, the location of the PIP alters greatly. This movement in the PIP

causes an acceleration with a large magnitude to be commanded to the interceptor missile, particularly in the end game. To ensure the intercept occurred at the most difficult point to intercept, the target trajectories were translated in the horizontal plane. A second order, critically-damped system with a natural frequency of 2 rad/s was used to model the target response to acceleration commands.

For the simulations, the interceptor missile was launched with its body axis aligned with the vector created by the initial PIP. The standard deviation of the measurement in range was 5 m, the standard deviation of the bearing and elevation was set to 0.001 rad. A sample intercept of Target 4 is shown in Figure 7-6. The target trajectory is shown from the time the interceptor is launched. The commanded responses of the interceptor due to the maneuvers of the target are readily apparent. Figure 7-7 displays the interceptor velocity profile and acceleration profile for the sample intercept. The impact of the commanded acceleration on the speed of the missile is observed in the last 5 s before intercept. The large accelerations required on the interceptor missile cause the missile to fly in an attitude which increases the drag, thus decreasing the missile velocity. The large acceleration incurred on the missile for approximately the first 9 s is the boost stage of the missile. For the remainder of the missile flight, the acceleration on the missile is in direct response to the weaves of the target. Note that in each response to a target maneuver, the peak magnitude of acceleration is increasing as the relative range between the target and interceptor is decreasing. The sample intercept was executed for both the CVCA and CVEIA3DTR filtering algorithms. To display the agility of the IMM in switching from model to model as the target maneuvers, the model probabilities over the last 30 s of the intercept are displayed in Figure 7-8. In both cases, before the target begins its weaving maneuver, the CV model probability is dominant. As the target begins its weave, the maneuver models respond accordingly, switching to CA model for the CVCA filter, or to the EIA model and proceeding to the 3DTR model for the CVEIA3DTR filter.

For the Monte Carlo experiments, the interceptor missile was launched with its body axis aligned with the vector created by the initial PIP. The missile has an initial thrust of 15000 lb. for the boost phase which lasts 9 s. The sustain phase of the missile lasts 30 s with 5000 lb. of thrust. The autopilot time constant for the missile was  $T_p = 0.17$  s. The data rate for the tracking radar was set to 4 Hz. The standard deviation of the radar measurement in range was 5 m, while the standard deviation of the bearing and elevation was 0.001 rad. The interceptor missile was tracked with the CV track filter with a process error covariance  $Q_k = 144 I_3 \text{ m}^2/\text{s}^4$ , where  $I_3$  is a 3 x 3 identity matrix.

The target was tracked with four different types of filters: a CV track filter, a CV track filter switching to a CA track filter at  $T_{tgo} = T_{set}$ , denoted as the CV-CA filter, a CVCA IMM track filter with kinematic constraint, and the CVEIA3DTR IMM track filter with the kinematic constraint. The process error covariances of the filters take into account the necessity of designing for a worst case scenario, which in CAW intercepts is a highly maneuvering target. The process error covariance for the CV track filter was  $Q_k = 3600 I_3 \text{ m}^2/\text{s}^4$ . The CV-CA track filter had process error covariances of  $Q_k^{cv} = 3600 I_3 \text{ m}^2/\text{s}^4$  and  $Q_k^{ca} = 900 I_3 \text{ m}^2/\text{s}^6$ . The CVCA with kinematic constraint has process error covariances of  $Q_k^{cv} = 25 I_3 \text{ m}^2/\text{s}^4$ ,  $Q_k^{ca} = 400 I_3 \text{ m}^2/\text{s}^6$ , and a KC variance of  $(500(0.9)^k + 2.4)$ . The initial model probabilities were  $\mu_0 = [0.9 \ 0.1]^T$  with model switching probabilities

$$\Pi = \begin{bmatrix} 0.97 & 0.03 \\ 0.05 & 0.95 \end{bmatrix} \quad (7.1)$$

The CVEIA3DTR with the kinematic constraint has process error covariances of  $Q_k^{cv} = 1 I_3 \text{ m}^2/\text{s}^4$ ,  $Q_k^{eia} = 676 I_3 \text{ m}^2/\text{s}^6$ , and  $Q_k^{3dtr} = 25 I_3 \text{ m}^2/\text{s}^6$  and  $\alpha = 0.89 \text{ Hz}$  for the EIA model and a KC variance of  $(500(0.9)^k + 2.4)$ . The initial model probabilities were  $\mu_0 = [0.9 \ 0.05 \ 0.05]^T$  with model switching probabilities

$$\Pi = \begin{bmatrix} 0.97 & 0.03 & 0 \\ 0 & 0.7 & 0.3 \\ 0.05 & 0 & 0.95 \end{bmatrix} \quad (7.2)$$

The measuring stick used to evaluate the performance of the track filters was the miss distance between the interceptor and the target. An average of the miss distances over the Monte Carlo experiments is calculated along with the values in which 90 percent and 98 percent of the miss distances fell.

The first set of simulations were executed against the four targets with the PN guidance numerical gain  $n$  remaining constant at  $n=4.0$ , 1 dwell on the target and interceptor during the intercept, and the data rate was 4 Hz. The time at which the CV-CA filter switched from the CV track filter to the CA track filter was set to  $T_{set}=8.0 \text{ s}$ . The results of Target 1 are given in Figure 7-9, which shows that all of the track filters perform reasonably well. However, the two IMM filtering techniques do provide lower miss distances. The CV-CA track filter did not perform as well due to assuming constant acceleration over the last 10 s when the target is in fact flying at a constant velocity. Figure 7-10 displays the results for Target 2. Once again the CVCA and the CVEIA3DTR track filters outperform their counterparts. The average miss distances are relatively high as compared to that of Target 1 for all the track filters. A possible explanation may be the combination of an extremely mild maneuver, angular measurement error, and relatively slow data rate. The results of

the intercepts of Target 3 are given in Figure 7-11. The CV-CA track filter maintains an average miss distance similar to that of the CVCA and CVEIA3DTR track filters. However, the CVCA and CVEIA3DTR track filters maintain a lower 98 percent miss distance over all the intercept ranges. The results from Target 4, shown in Figure 7-12, display the CVCA and CVEIA3DTR track filters achieve a dramatic miss distance reduction over that of the CV and CV-CA track filters over all the intercept ranges. As expected, the CV track filter does not provide good performance against the highly maneuvering target.

As shown, the two IMM filtering techniques provide superior performance over of their single-model counterparts. However, the miss distances given by each of the track filters for any of the maneuvering targets must be improved in order to provide a successful intercept. In keeping with the notion of designing for the worst-case scenario, ideas to reduce the miss distance were executed against Target 4. Once the best combination of options for each track filter was found for the highly maneuvering target, Monte Carlo experiments against the other targets were executed. Altering the numerical gain  $n$  for the PN guidance commanded acceleration was tested to examine its affect on the miss distance. The details of each particular option are described in Chapter 6. For the single-model track filters, the options for the numerical gain  $n$  were to either remain constant, Option 1, linearly increase proportional to  $T_{tgo}$  when  $T_{tgo} \leq T_{set}$ , Option 2, or as a function of an assumed acceleration of the target, Option 3. The IMM track filters have additional options available because of the model probabilities. These options include a linear function of  $\mu_{cv}$ , Option 4, and a cosine function of  $\mu_{cv}$ , Option 5. The four track filters were executed against Target 4 with the number of dwells set to 1. The maximum value that the numerical gain was allowed to be set to was  $n_{max}=4.6$  while the minimum was set to  $n_{min}=3.8$ . If the option to remain constant was chosen, the numerical gain was set to  $n=4.0$ . Figure 7-13 displays the results for the CV track filter. Though the options that alter the numerical gain of the commanded accelerations provide an improvement, neither Option 2 nor 3 appeared superior over the other. The results for the CV-CA track filter are presented in Figure 7-14. Both of the options for adjusting the numerical gain provide lower miss distances over the shorter intercept ranges. Over the longer intercept ranges, the average miss distance using either Option 2 or 3 is similar to that of keeping the gain constant, Option 1. Options 2 and 3 do not provide as low of 90 percent miss distances over the longer intercept ranges yet they maintain similar 98 percent miss distances. Figure 7-15 and Figure 7-16 display the results for the CVCA and CVEIA3DTR track filters. For both IMM tracking filters, all of the options that adjust the numerical gain  $n$  provide reductions in the miss distances. However, none of the options appears to provide a significant improvement over any of the other options. Based

on having consistently the lowest 98 percent miss distance, the numerical gain Option 3 was chosen to be the guidance scheme for the remaining Monte Carlo experiments.

In addition to adjusting the numerical gain of the PN guidance commanded acceleration, ideas discussed in Chapter 5 to adjust the number of radar dwells on both the target and the interceptor to reduce the effective angular measurement error were implemented. For the single model track filters, the options are to maintain a single dwell for the duration of the intercept, calculate the number of dwells needed through the method described in Chapter 5 at time  $T_{tgo} \leq T_{set}$  with a maximum allowable number of dwells set to  $N_{max} = 10$ , or to increase the number of dwells from 1 to 10 over the time  $T_{tgo} \leq T_{set}$ . In addition to these options, the IMM track filters have the option to vary the number of dwells to either 4 or 10, depending on the model probabilities. For all the experiments,  $T_{set}=4$  s. The results of adjusting the number of dwells against Target 4 are given in Figures 7-17 through 7-20.

Figure 7-17 displays the results of the various dwell options using the CV track filter. It is readily apparent that increasing the number of dwells during the end game dramatically improves the performance achieved through the CV track filter. The method by which the number of dwells is calculated provides the lowest average miss distance. This is due to the number of dwells being increased at time  $T_{set} + 1$ , rather than  $T_{set}$ , to bring the positional term of the error covariance matrix to a value of  $10r_{min}$ . The extra time with increased dwells yields a lower miss distance. The results for the CV-CA track filter are presented in Figure 7-18. Once again, increasing the dwells over the end game provides for a significant improvement in the miss distances. Figure 7-19 displays the results for the CVCA track filter. The CVCA track filter displays a marked improvement in the miss distances using any of the three alternative methods. However, the method by which the number of dwells is calculated provides the lowest miss distances. The results for the CVEIA3DTR track filter, Figure 7-20, are similar to that of the CVCA track filter. This is due to the additional second of increased dwells when the dwells are calculated, as explained earlier.

The final set of Monte Carlo experiments incorporated the options that resulted in the lowest miss distances for the various track filters. The process error covariances for the track filters remained unchanged along with the initial model probabilities and model switching probabilities for the two IMM track filters. The number of dwells for the  $T_{tgo} \leq 4.0$  s for all the track filters were calculated as described in Chapter 5. The numerical gain  $n$  for the PN guidance command acceleration was set according to an assumed acceleration of the target, Option 3 as previously discussed.



The results of the Monte Carlo experiments on all the various targets are provided in Figure 7-21 through Figure 7-26. The miss distances provided by the track filters against Target 1 are shown in Figure 7-21. The IMM algorithms provide lower miss distances than either of the single-model filters. In Figure 7-22, the results for the mildly weaving target, Target 2, are shown. Once again, the IMM algorithms provide lower miss distances than the single-model filters. However, the miss distances for Target 2 are significantly higher than Target 1. In comparing the results of Target 2 against those of Targets 3 and 4, Figures 7-23 and 7-24, respectively, the miss distances achieved against Target 2 are the highest of all the targets. Since the maneuvers of Target 2 are so mild, the maneuvers may be discounted as noise. Thus, the filters do not detect the maneuver right away. The results of all the targets display the superiority of the multiple model algorithms over that of their single-model counterparts. Figure 7-25 displays the average number of dwells per measurement used by the various track filters over the time  $T_{tgo} \leq T_{set} + 1$  for Target 1 and Target 2 while Figure 7-26 displays the same information for Target 3 and Target 4. It is observed that the IMM track filters provide the lower miss distances with less radar dwells than the single model counterparts. The combination of multiple-model tracking algorithms, increasing the number of dwells during the end game, and adjusting the numerical gain of the PN guidance command acceleration provided superior performance to that of single-model track filters with similar alterations in the number of dwells and numerical gain  $n$ .

It is interesting to note that the mildly weaving target, Target 2, resulted in the largest miss distances. The target tracking filters were designed with relation to a worst-case scenario, a high-speed, highly-maneuvering target, Target 4. The slow-speed, mildly-maneuvering target is one in which further study is needed. It must also be noted that the miss distances are not only a function of the performance of the tracking filter, but are also inherently related to the fidelity of the interceptor missile model. The interceptor missile is a five degree of freedom simulation that does not take into account any rolling motion. Therefore, though the filtered state estimates of the target and the interceptor may be improved, enhancing the commanded accelerations of the interceptor missile, the resulting response of the interceptor missile to the commanded accelerations is not at the level as that of a six degree of freedom model. In essence, the miss distances presented are strictly for evaluation of differing target tracking filters and their relative performance to one another and the miss distance can only be reduced to the fidelity level of the interceptor missile model.

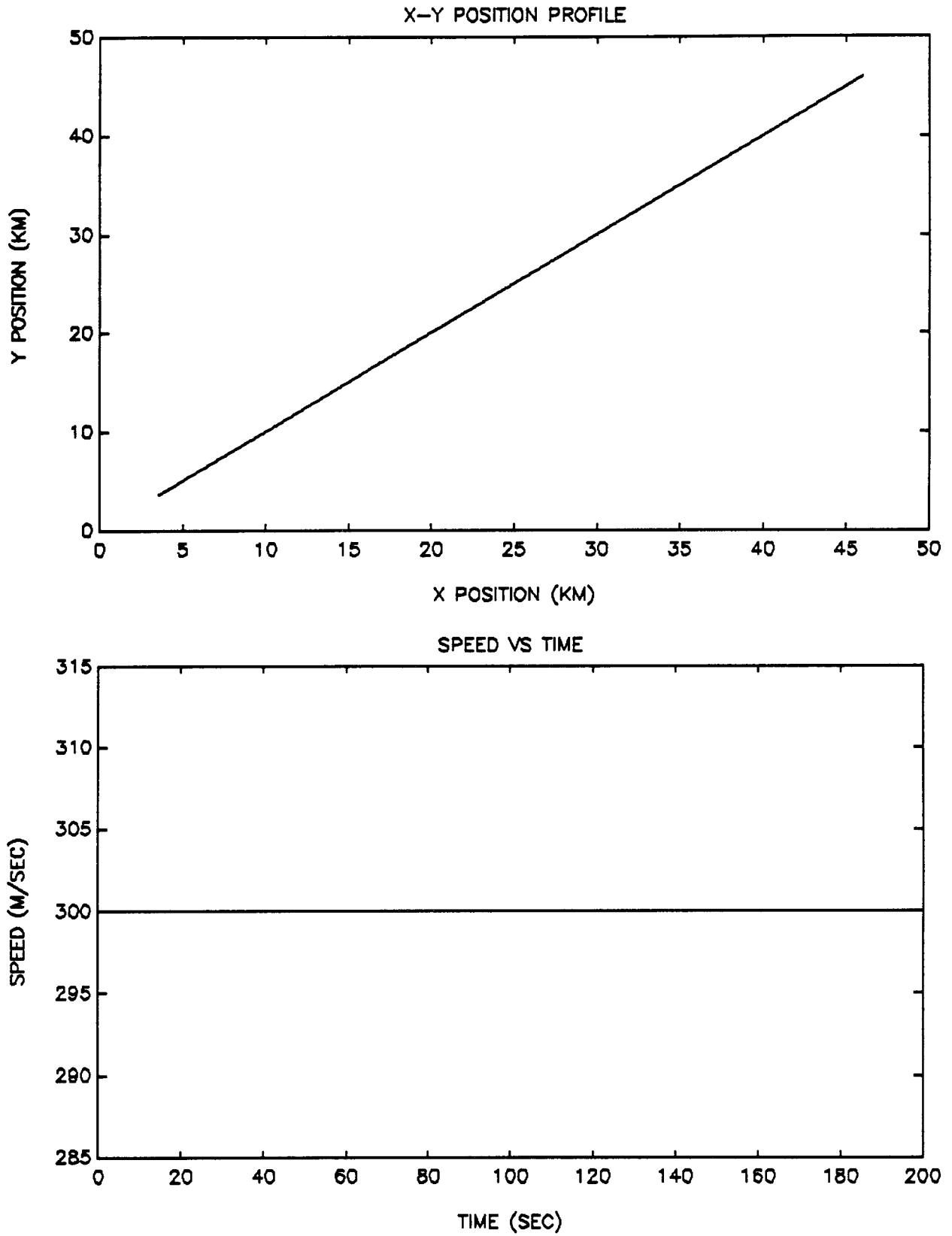


Figure 7-1. Constant Velocity Target Profile (Target 1)

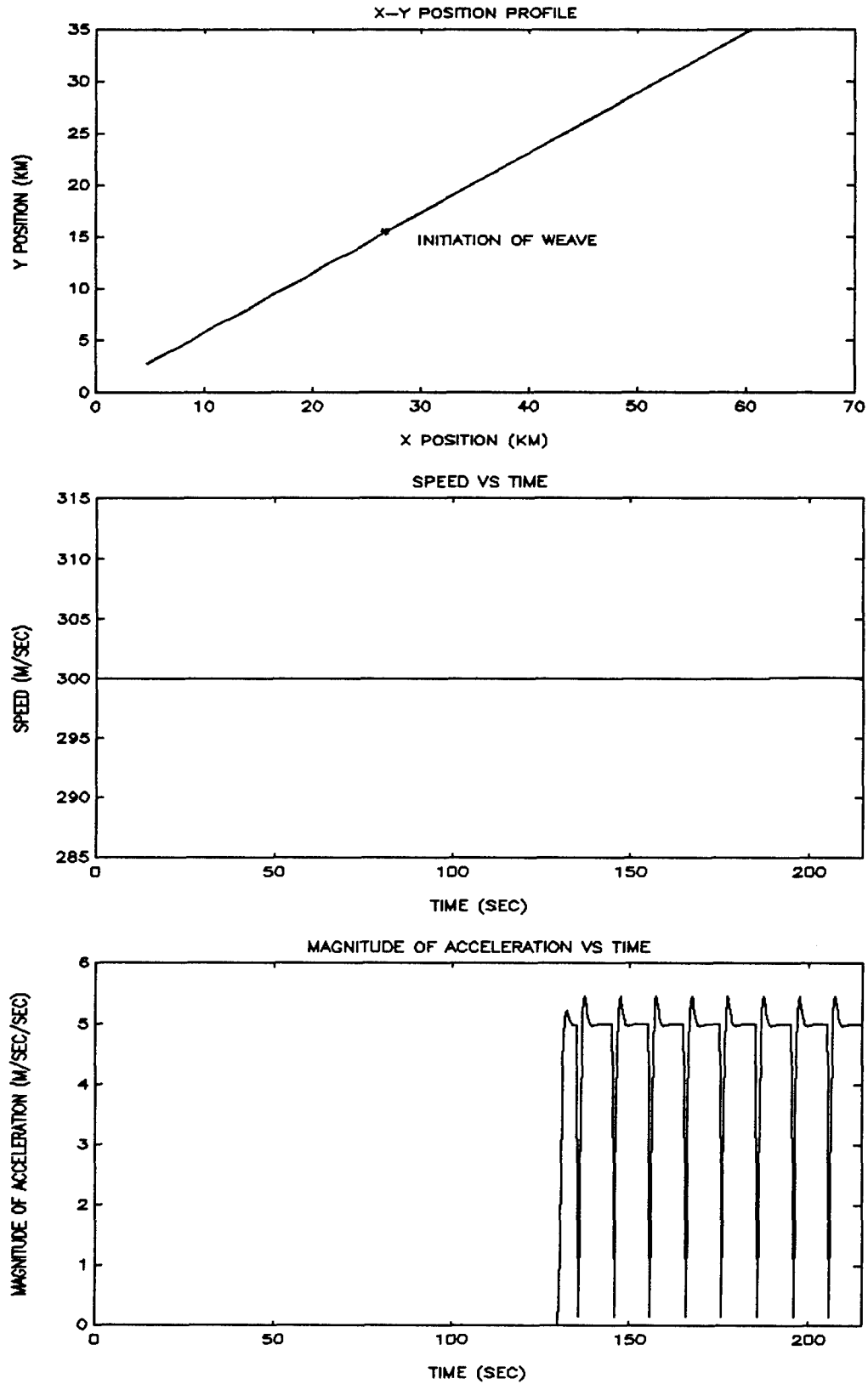


Figure 7-2. Mildly Weaving Target (Target 2)

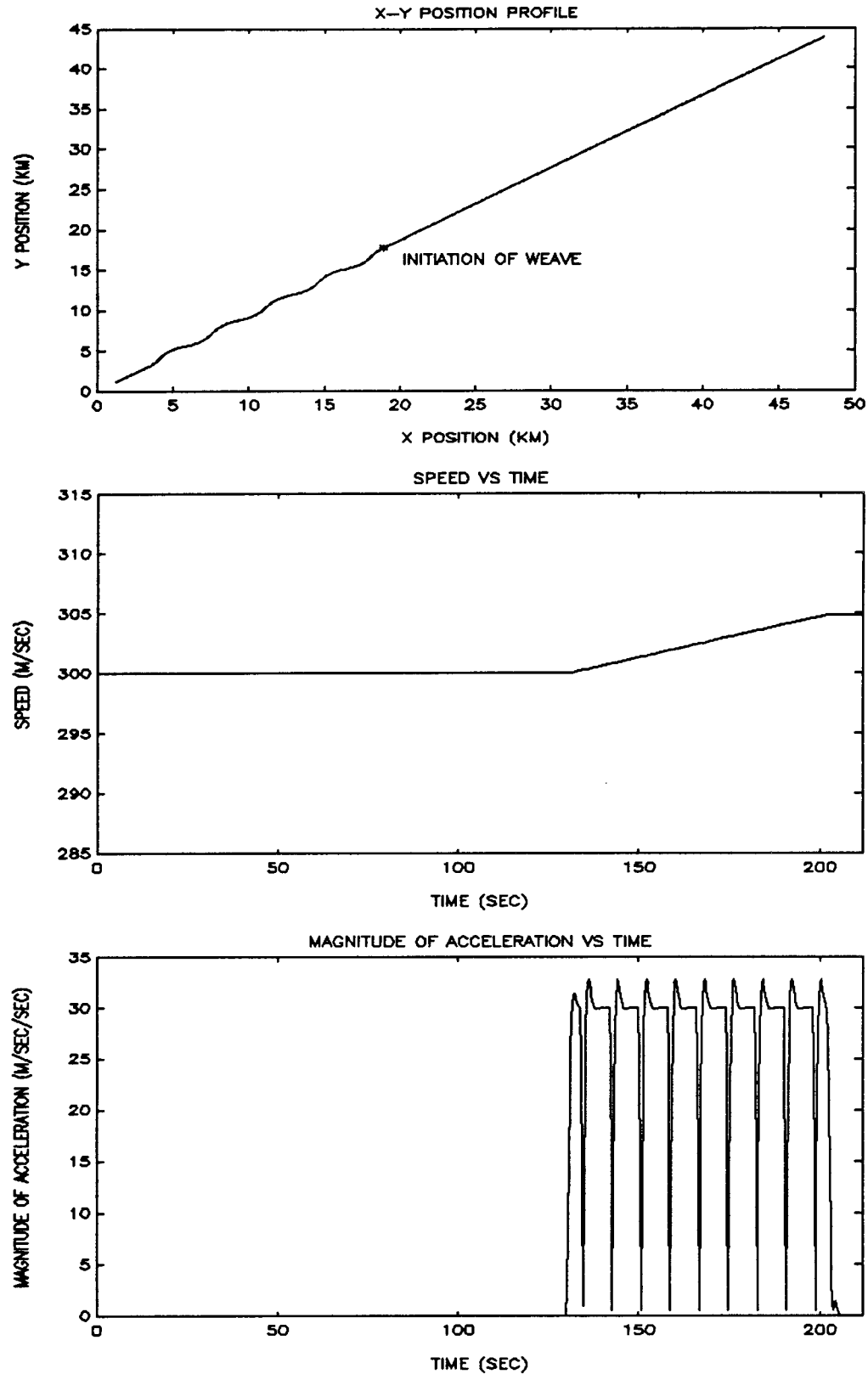


Figure 7-3. Weaving Target (Target 3)

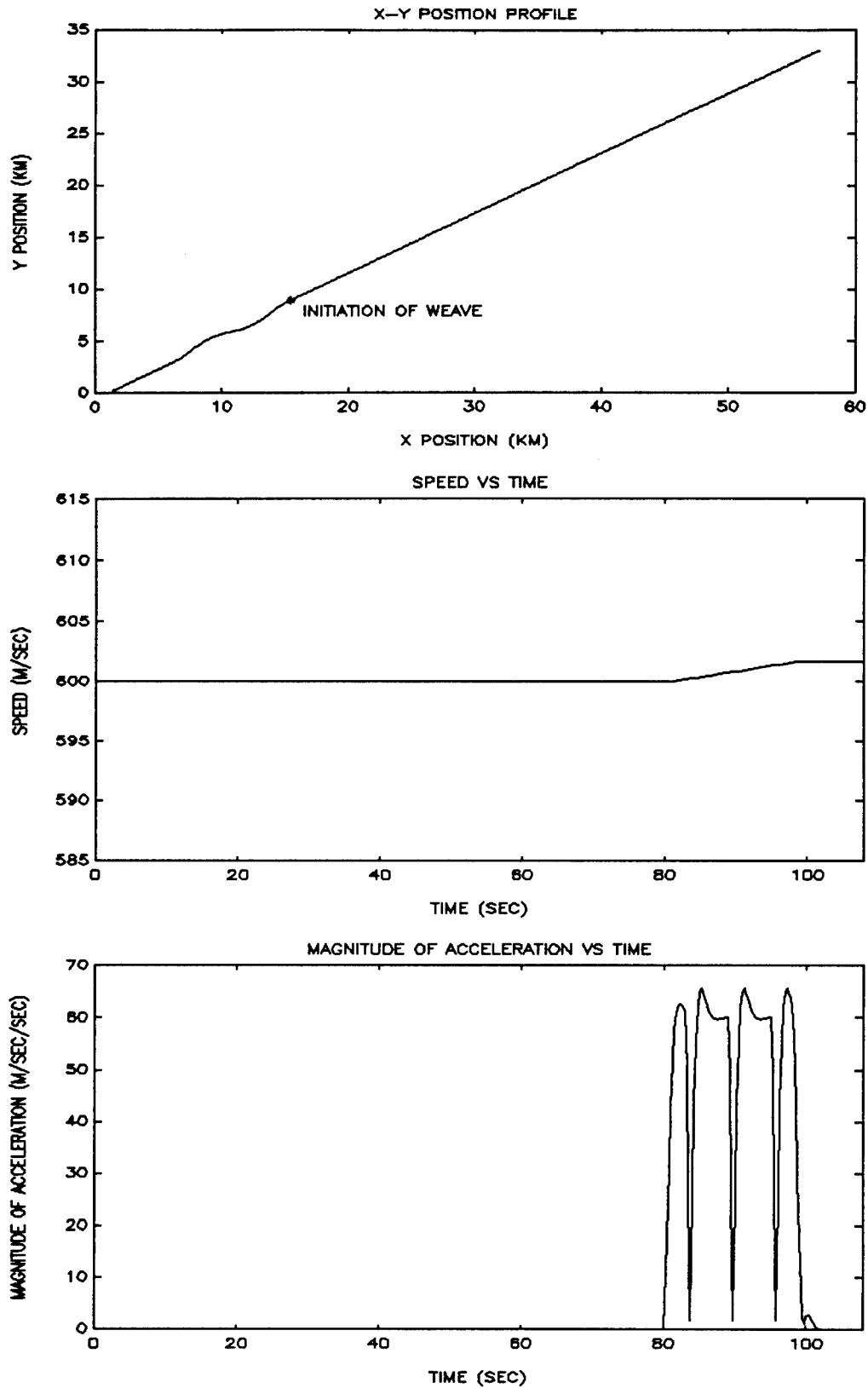


Figure 7-4. High Speed Weaving Target (Target 4)

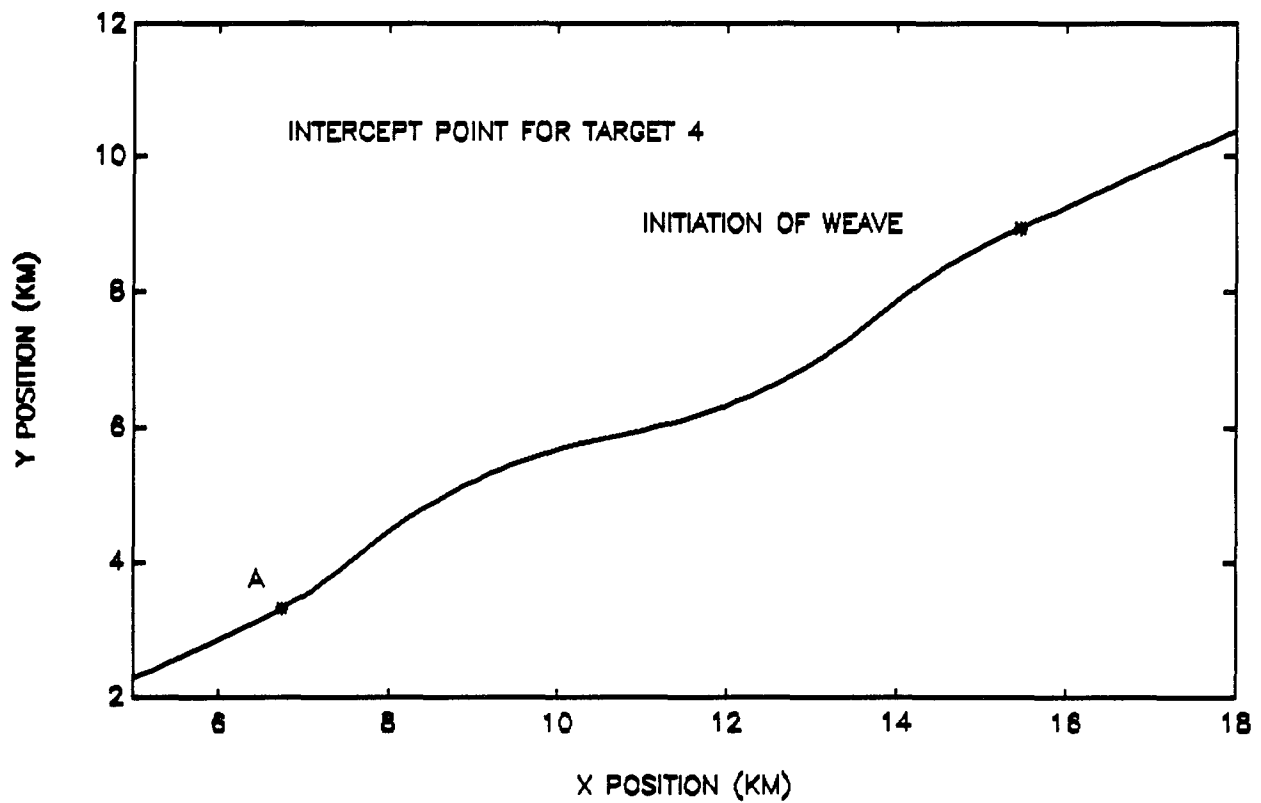
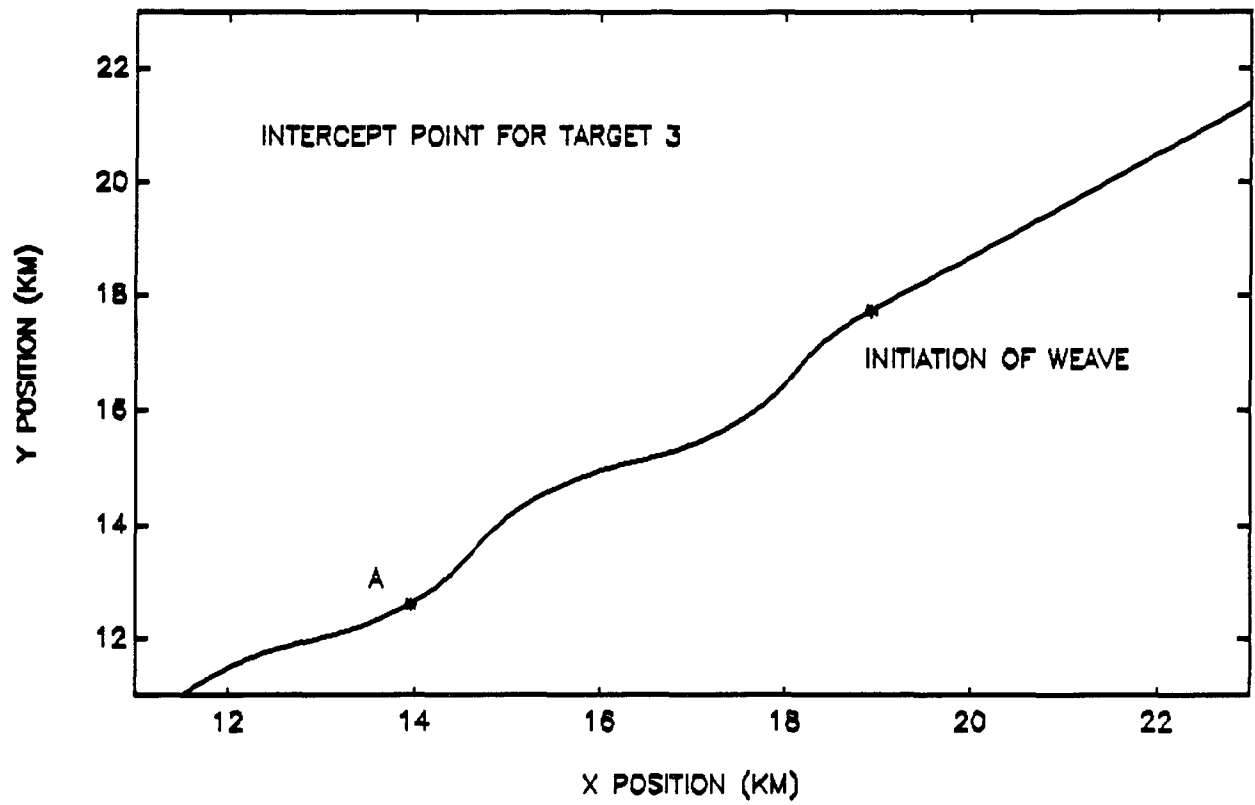


Figure 7-5. Toughest Intercept Points

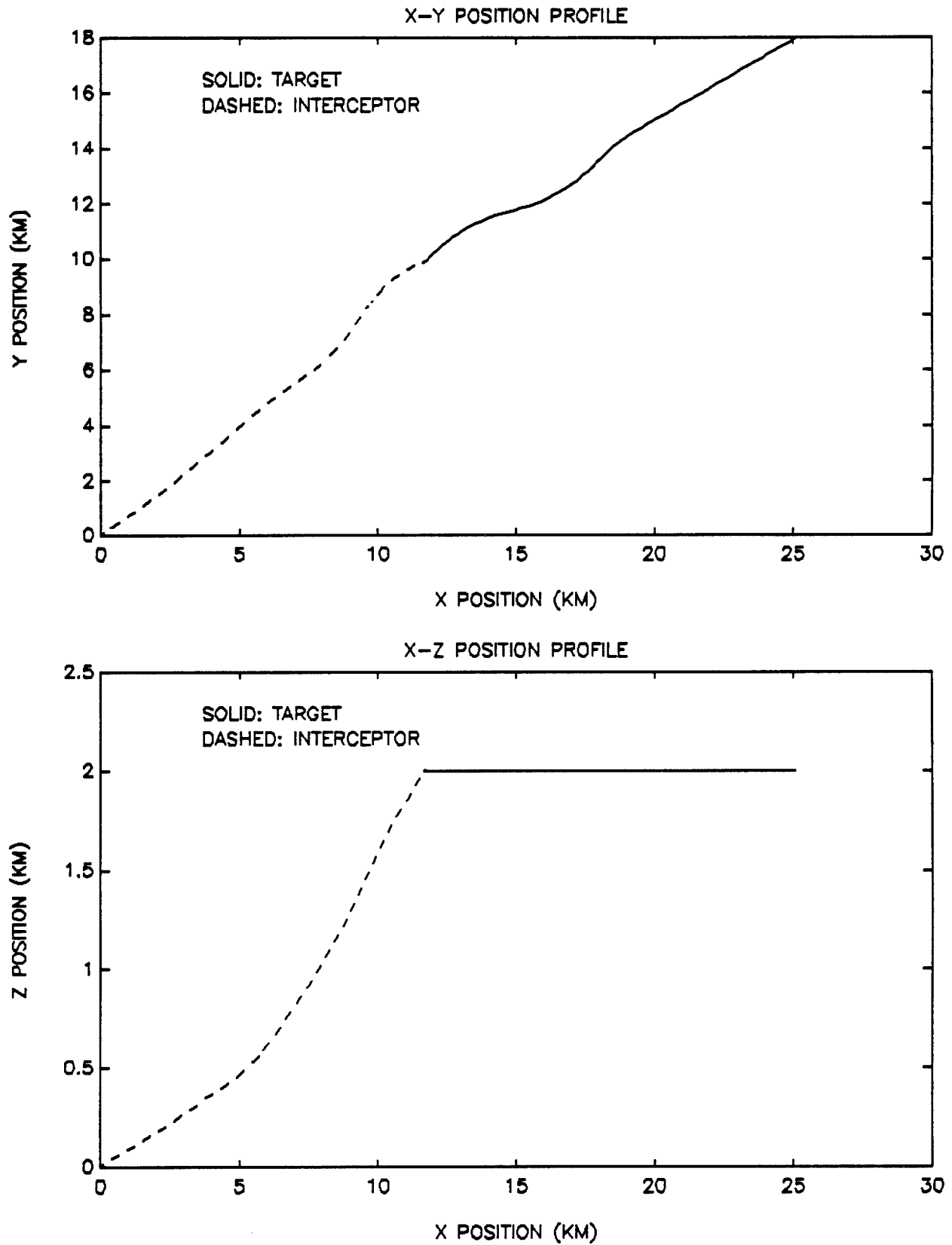


Figure 7-6. Sample Intercept of Target 3

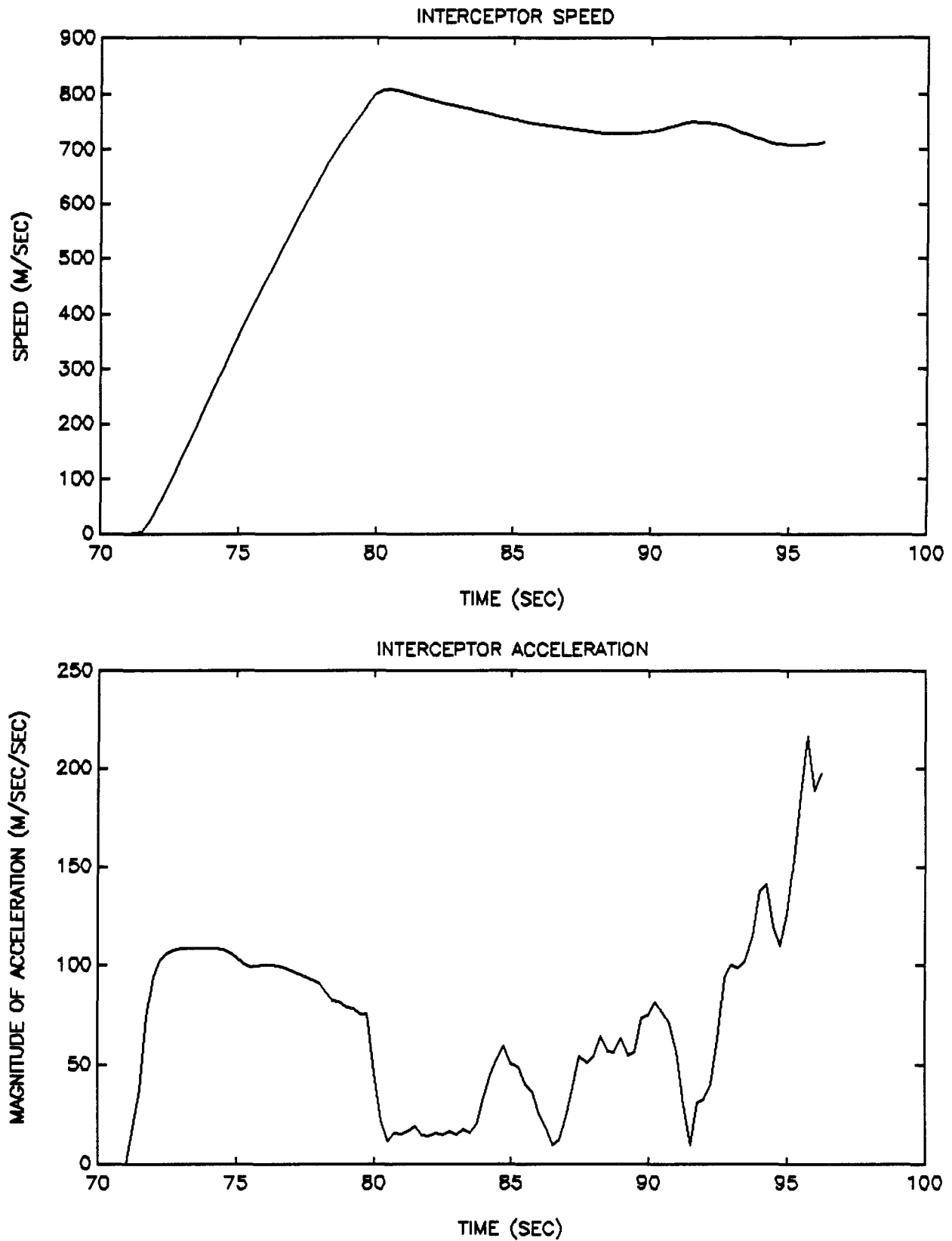


Figure 7-7. Velocity and Acceleration Profiles of Sample Intercept



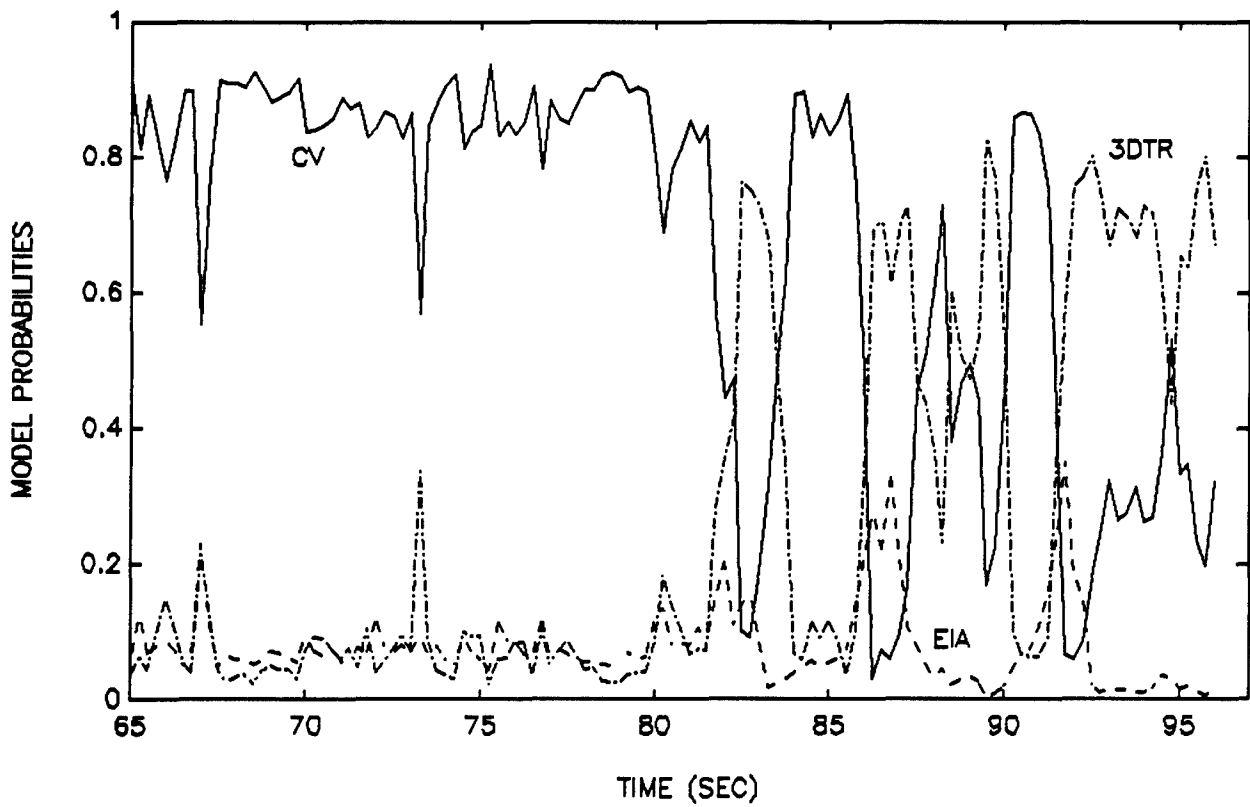
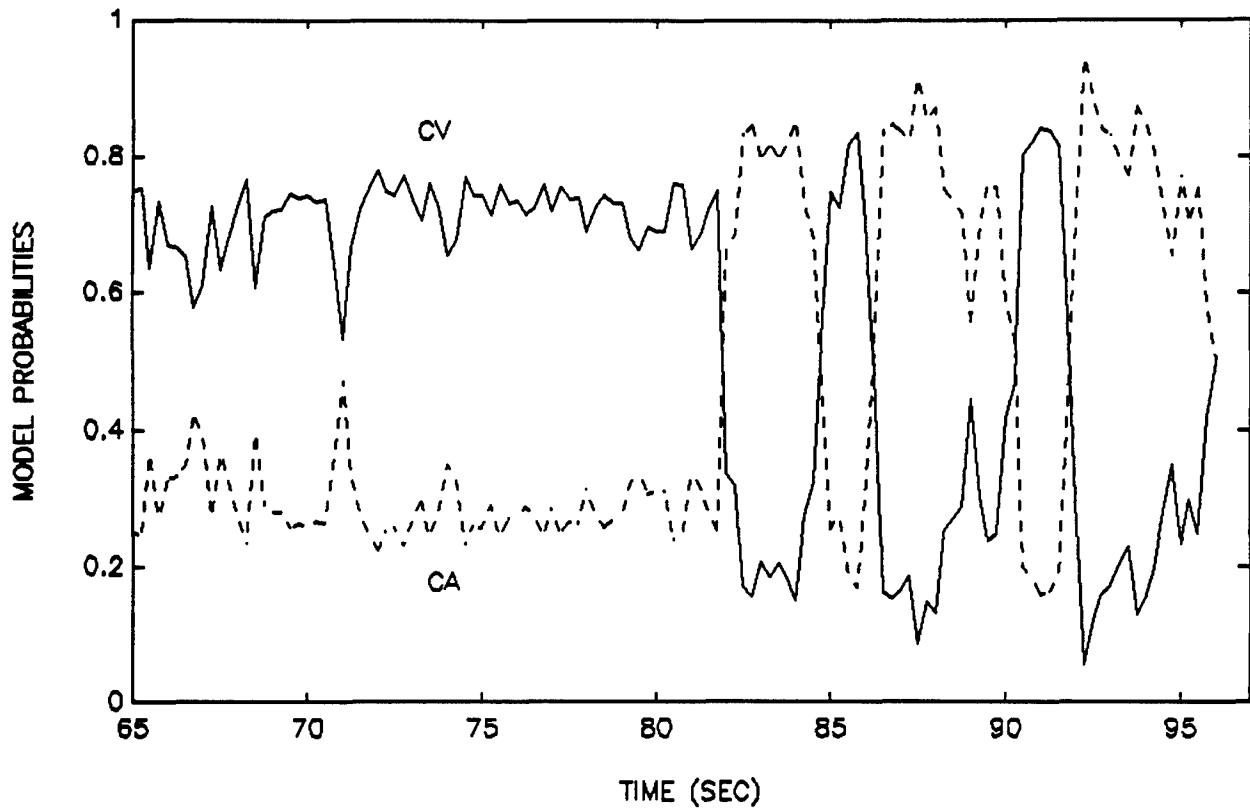


Figure 7-8. Sample Model Probabilities for CVCA and CVEIA3DTR

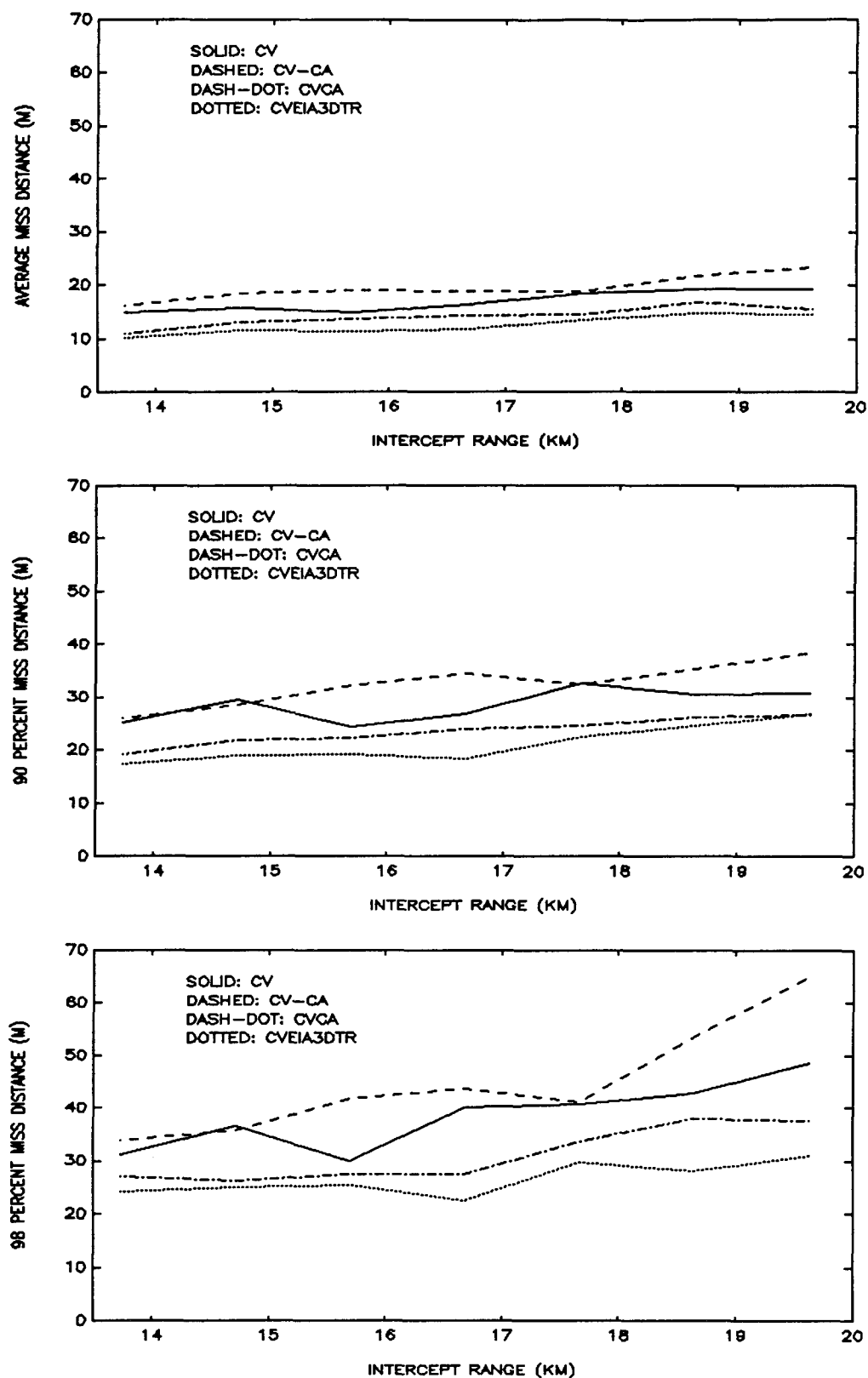


Figure 7-9. Initial Miss Distances for Target 1

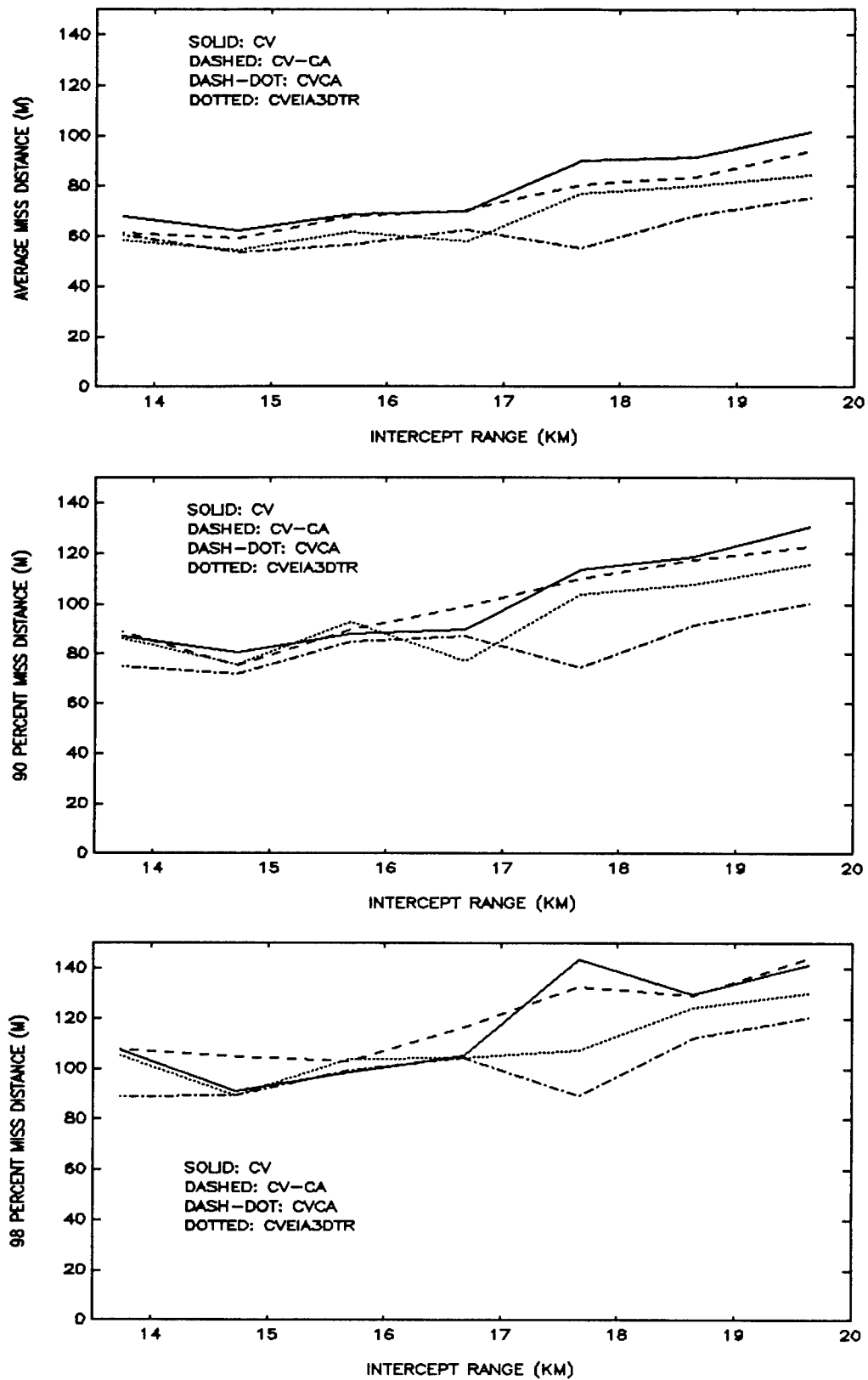


Figure 7-10. Initial Miss Distances for Target 2

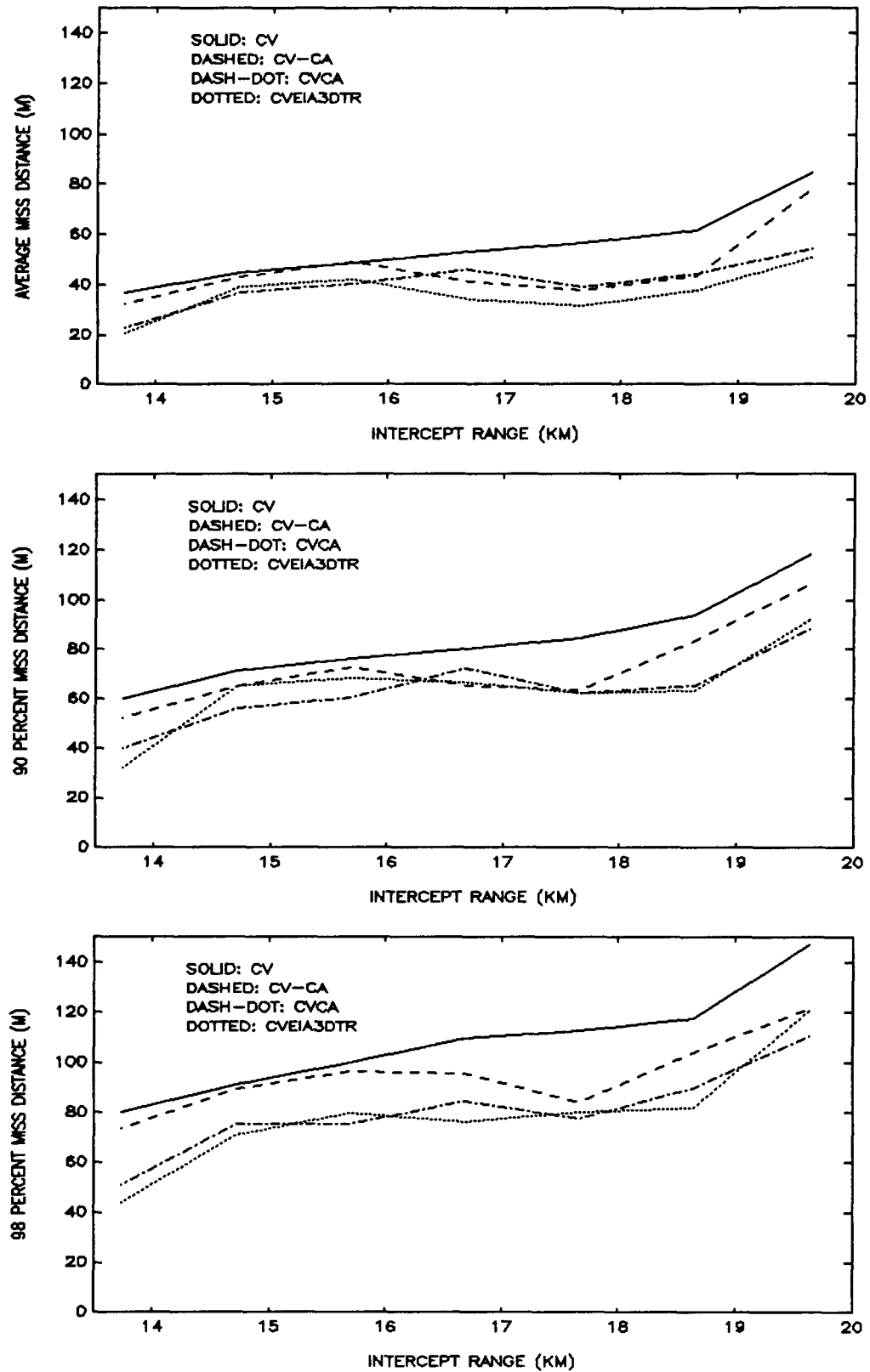


Figure 7-11. Initial Miss Distances for Target 3

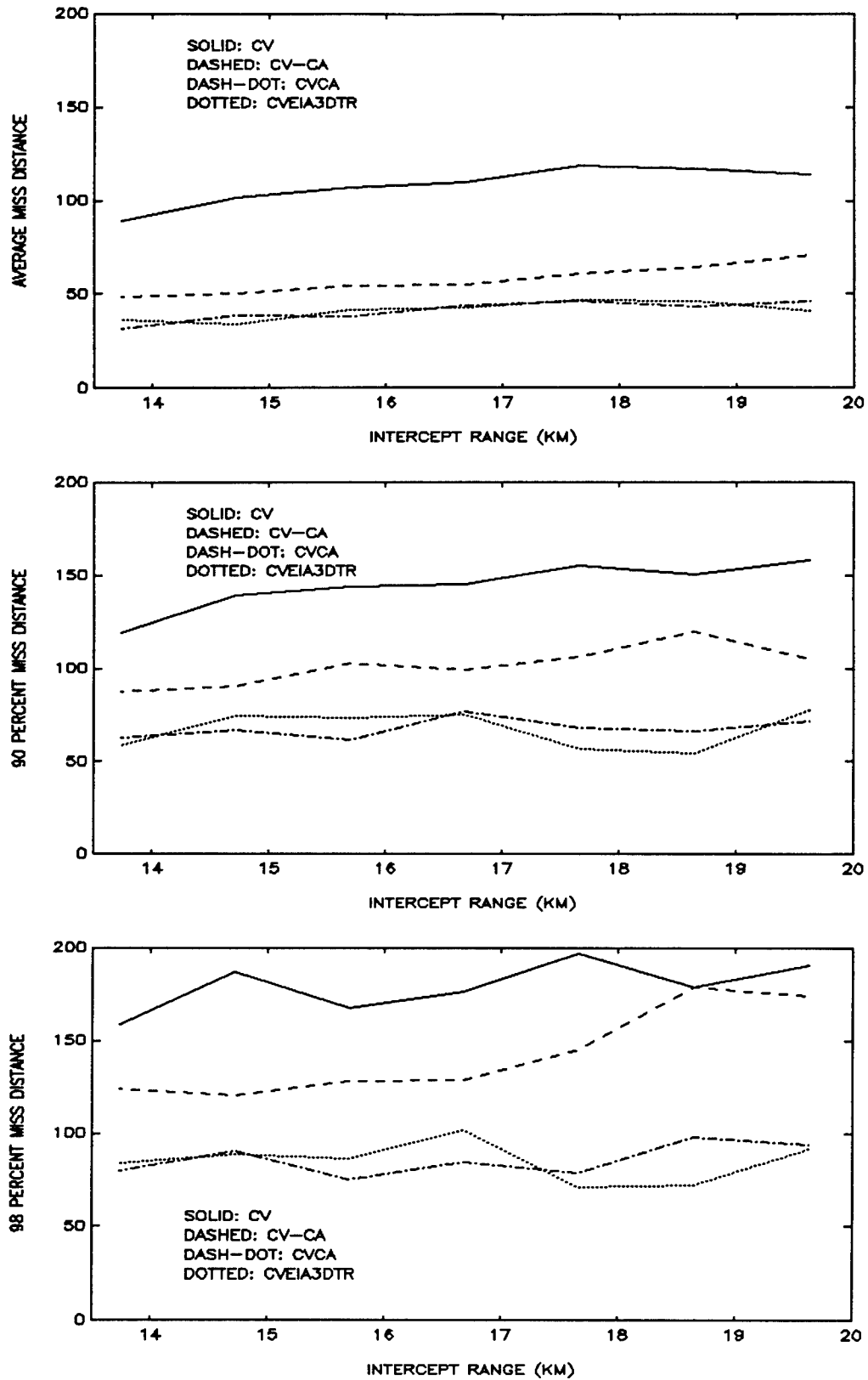


Figure 7-12. Initial Miss Distances for Target 4

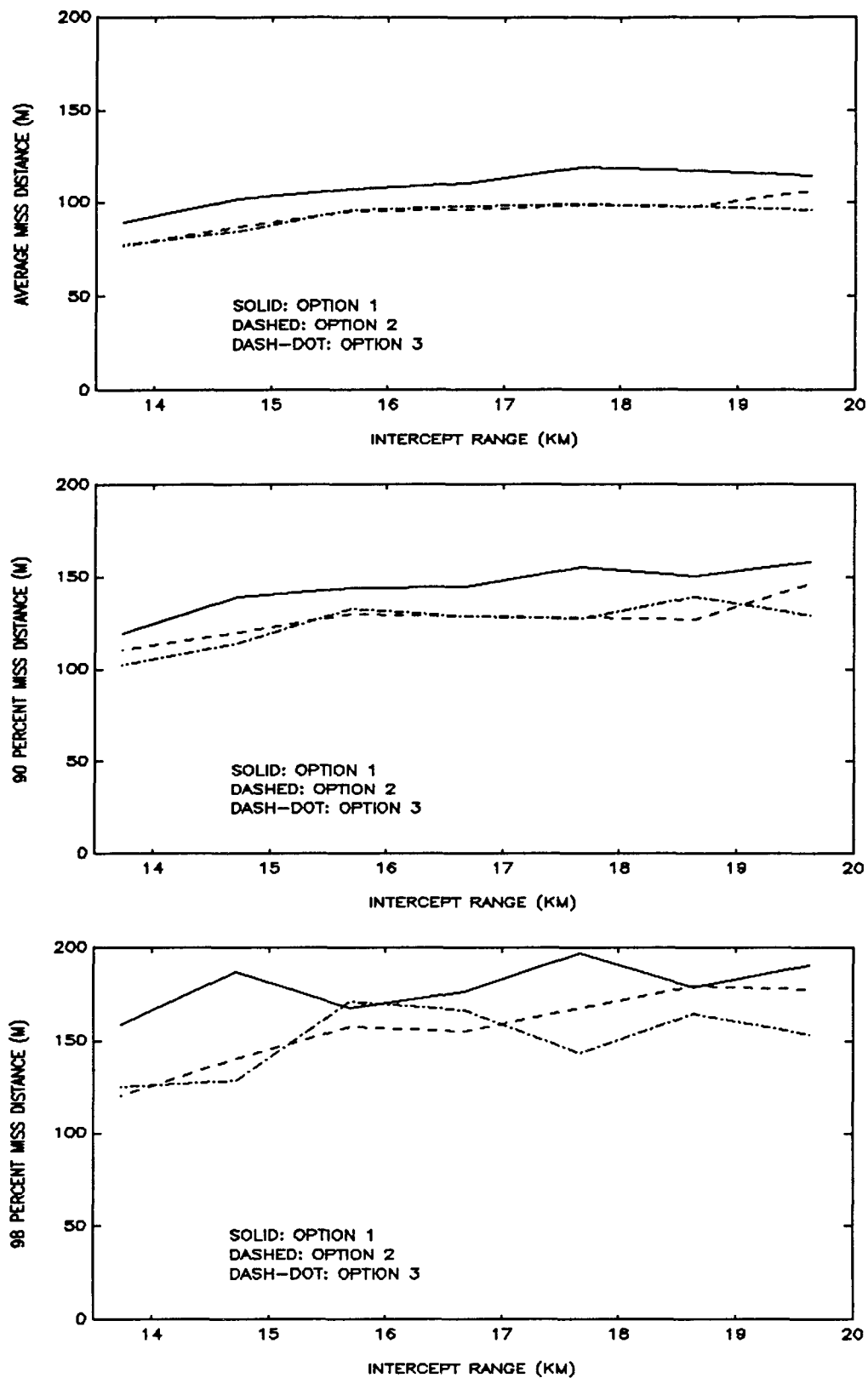


Figure 7-13. Various PN Guidance Options, CV Filter, Target 4

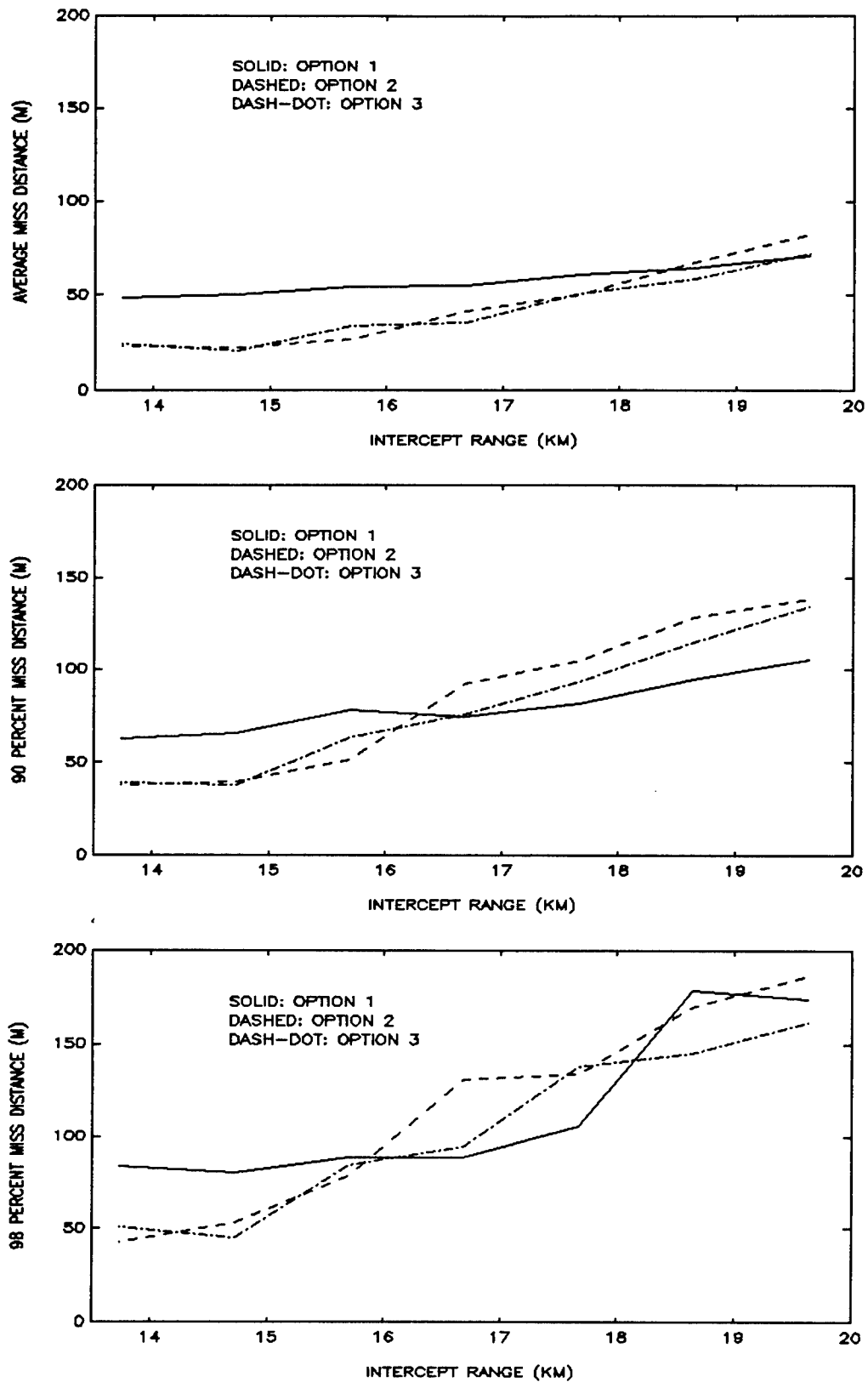


Figure 7-14. Various PN Guidance Options, CV-CA Filter, Target 4

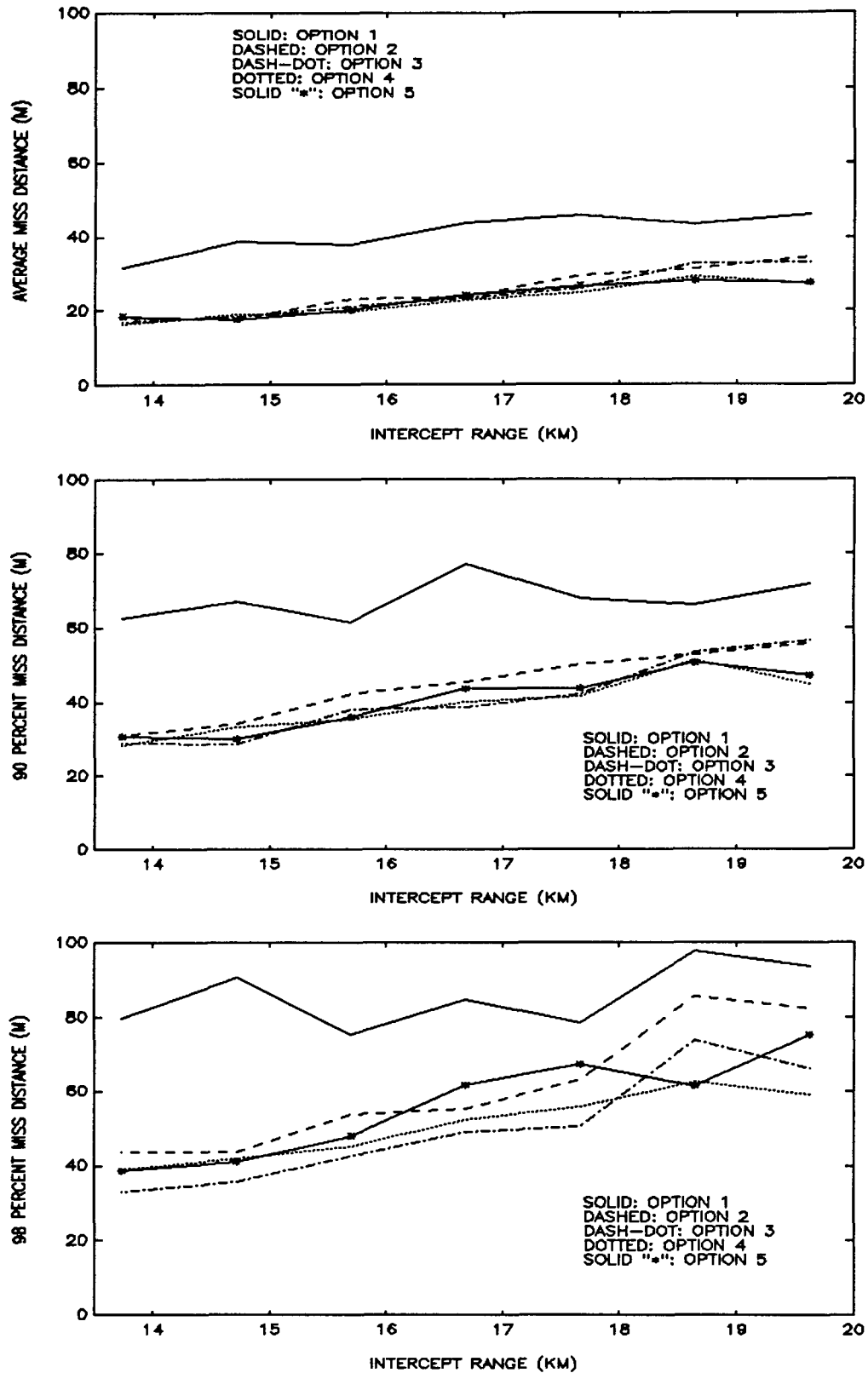


Figure 7-15. Various PN Guidance Options, CVCA Filter, Target 4



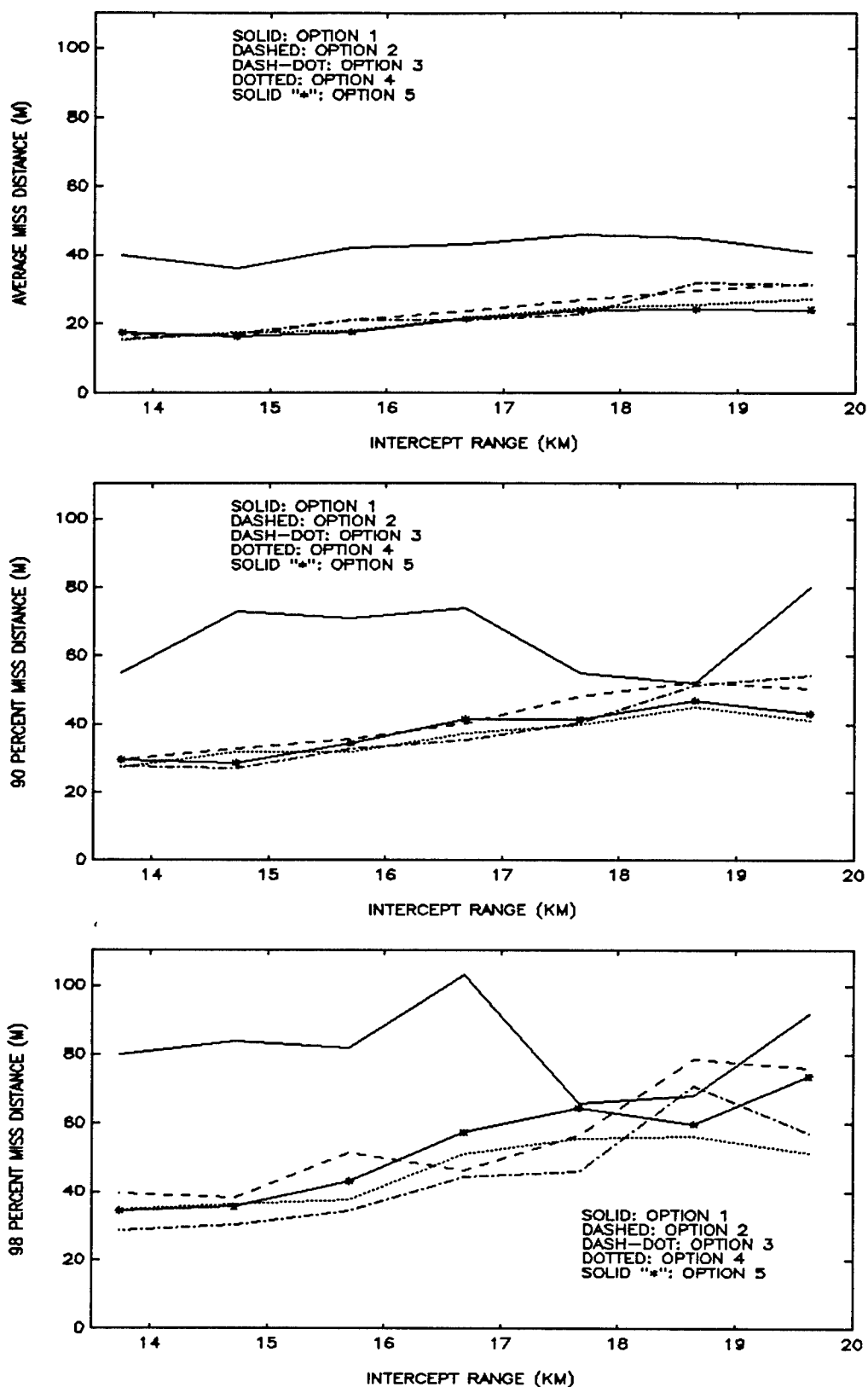


Figure 7-16. Various PN Guidance Options, CVEIA3DTR Filter, Target 4

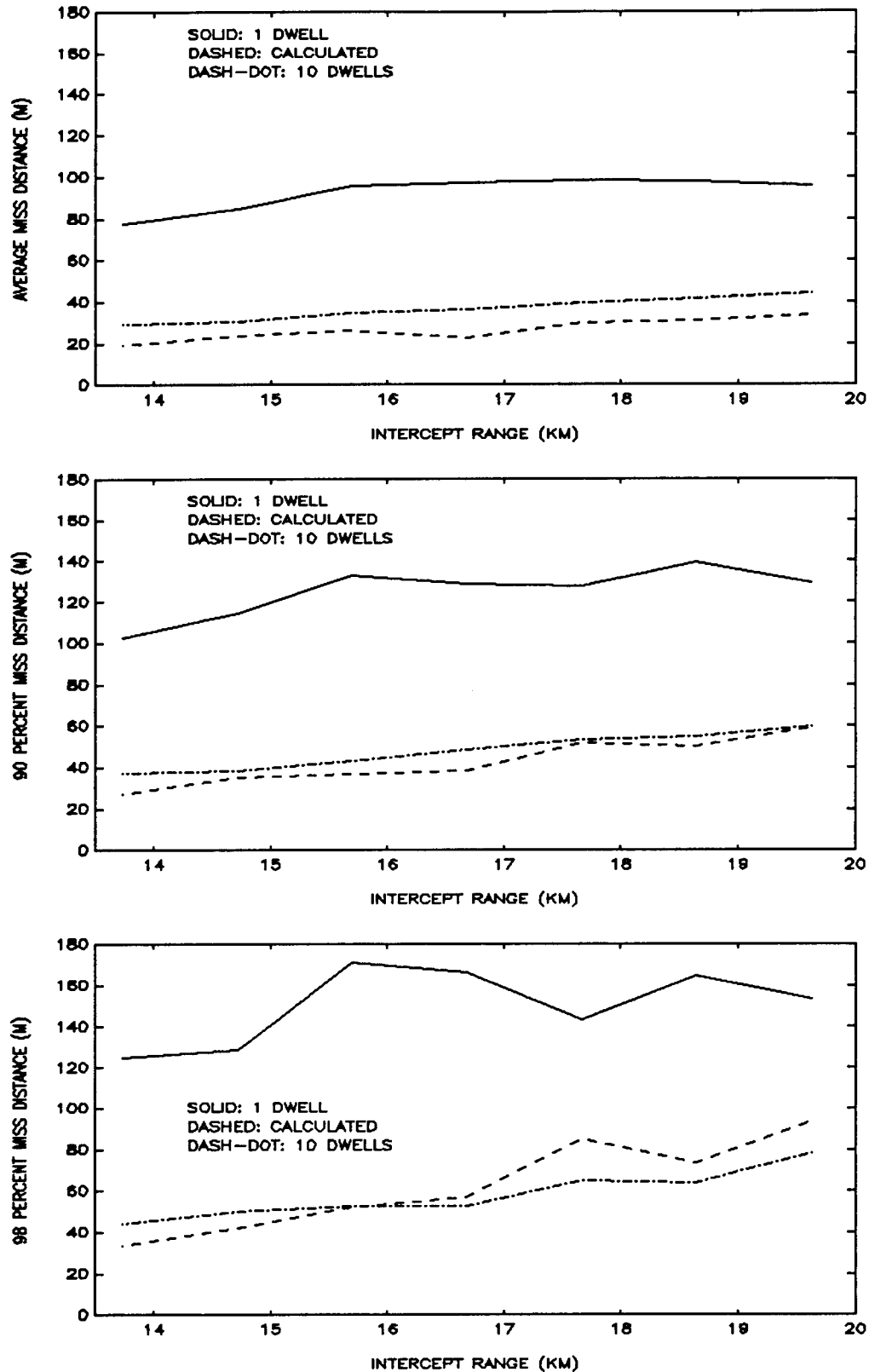


Figure 7-17. Various Dwell Options, CV Filter, Target 4

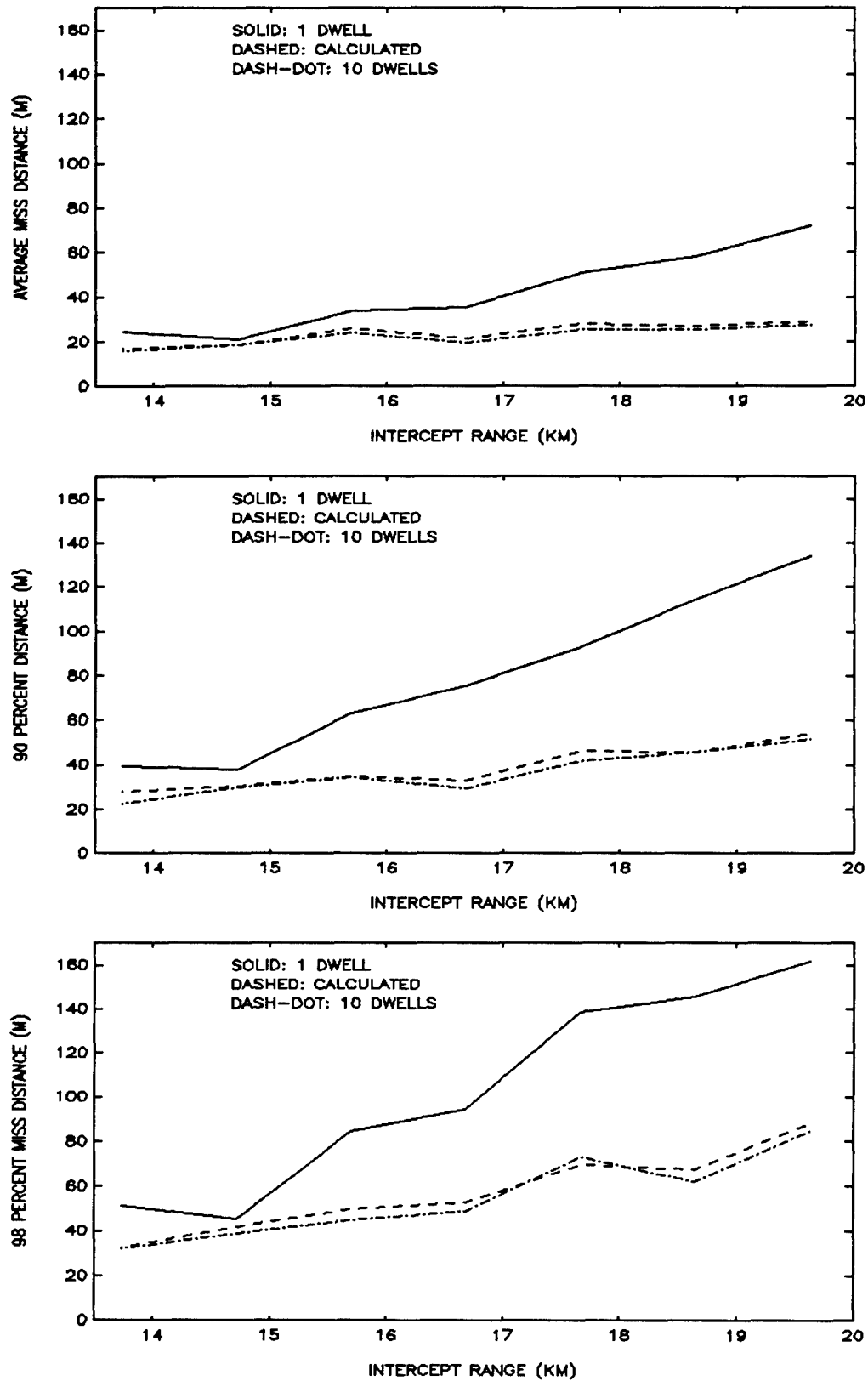


Figure 7-18. Various Dwell Options, CV-CA Filter, Target 4

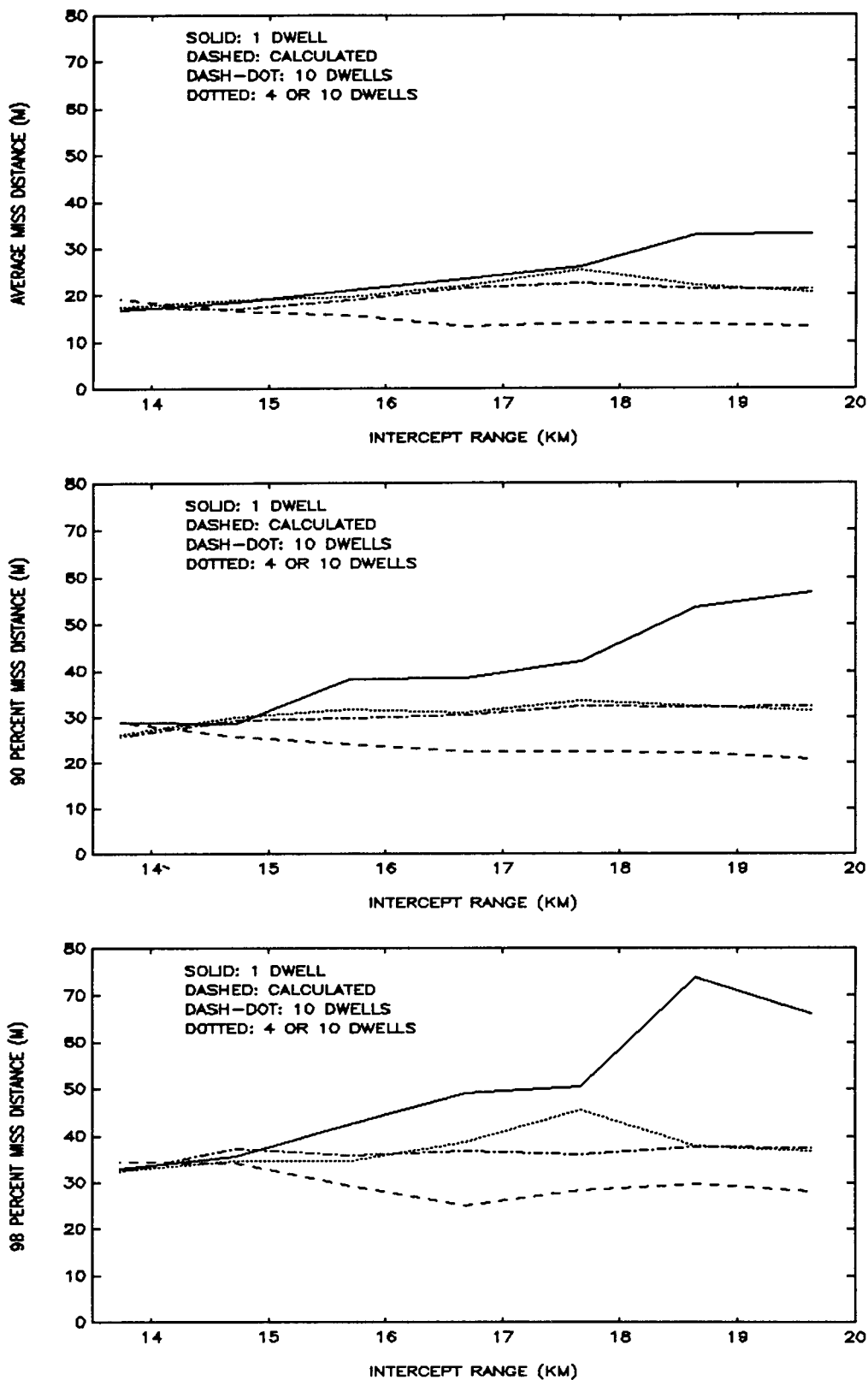


Figure 7-19. Various Dwell Options, CVCA Filter, Target 4

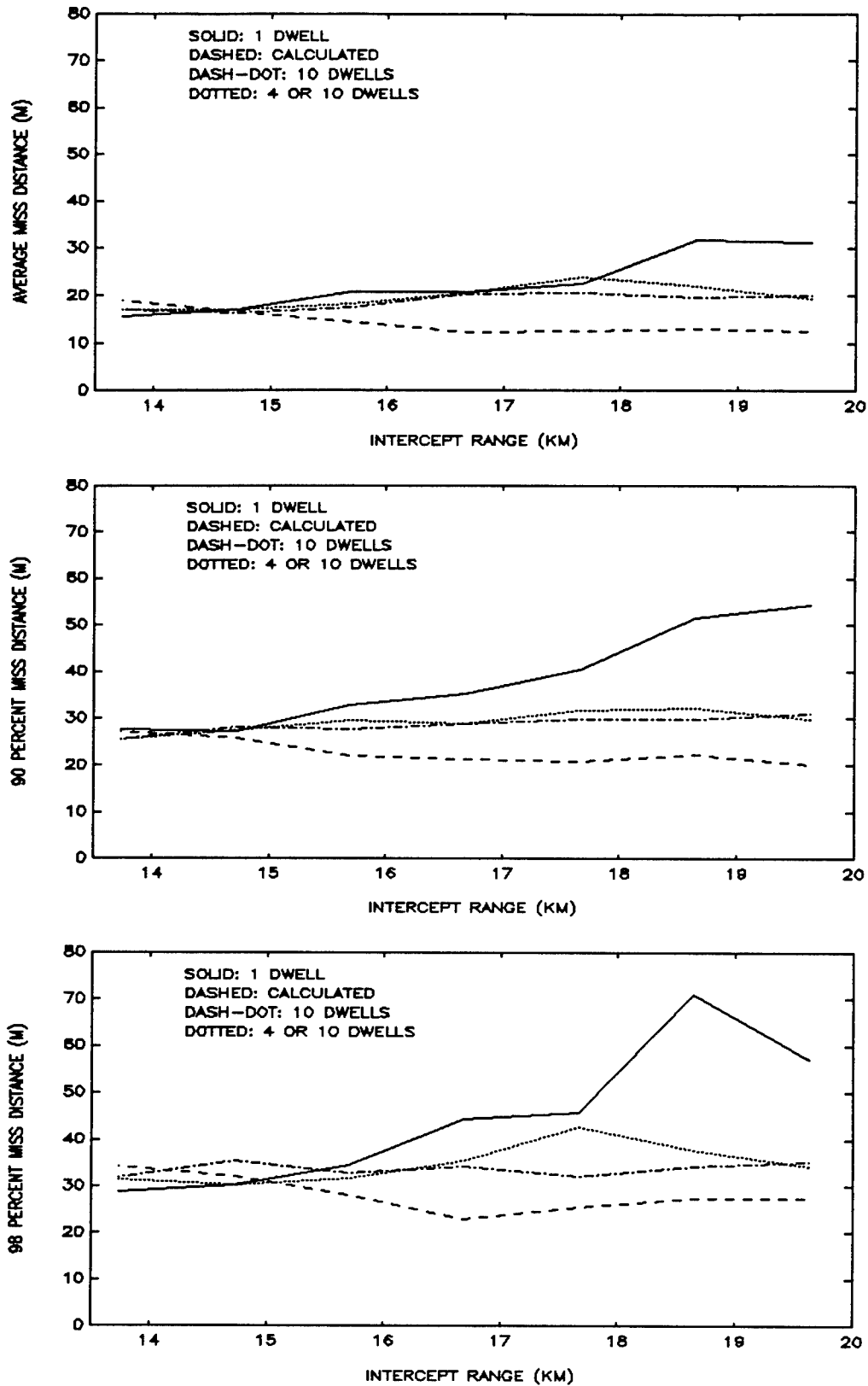


Figure 7-20. Various Dwell Options, CVEIA3DTR Filter, Target 4

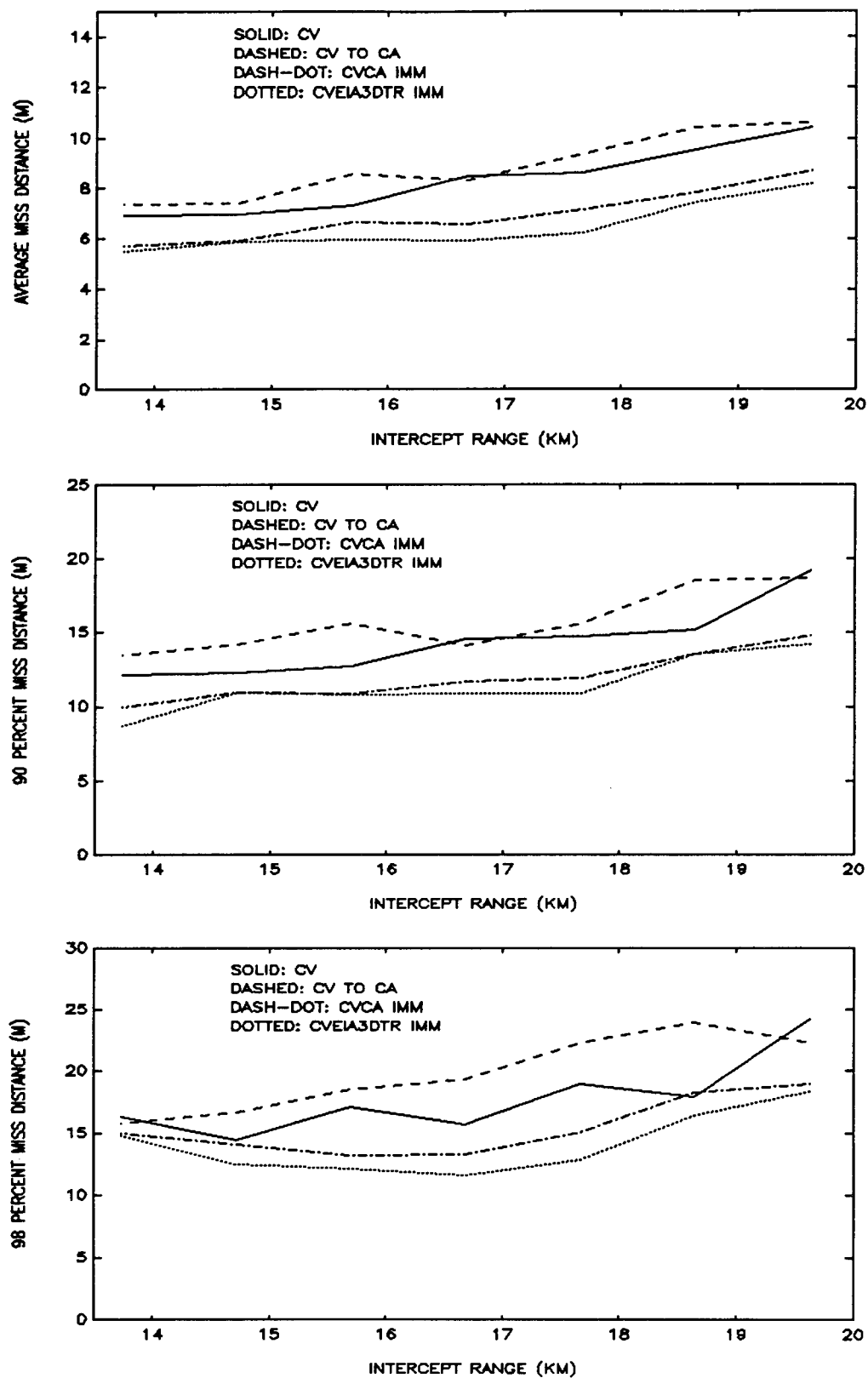


Figure 7-21. Miss Distances for Target 1

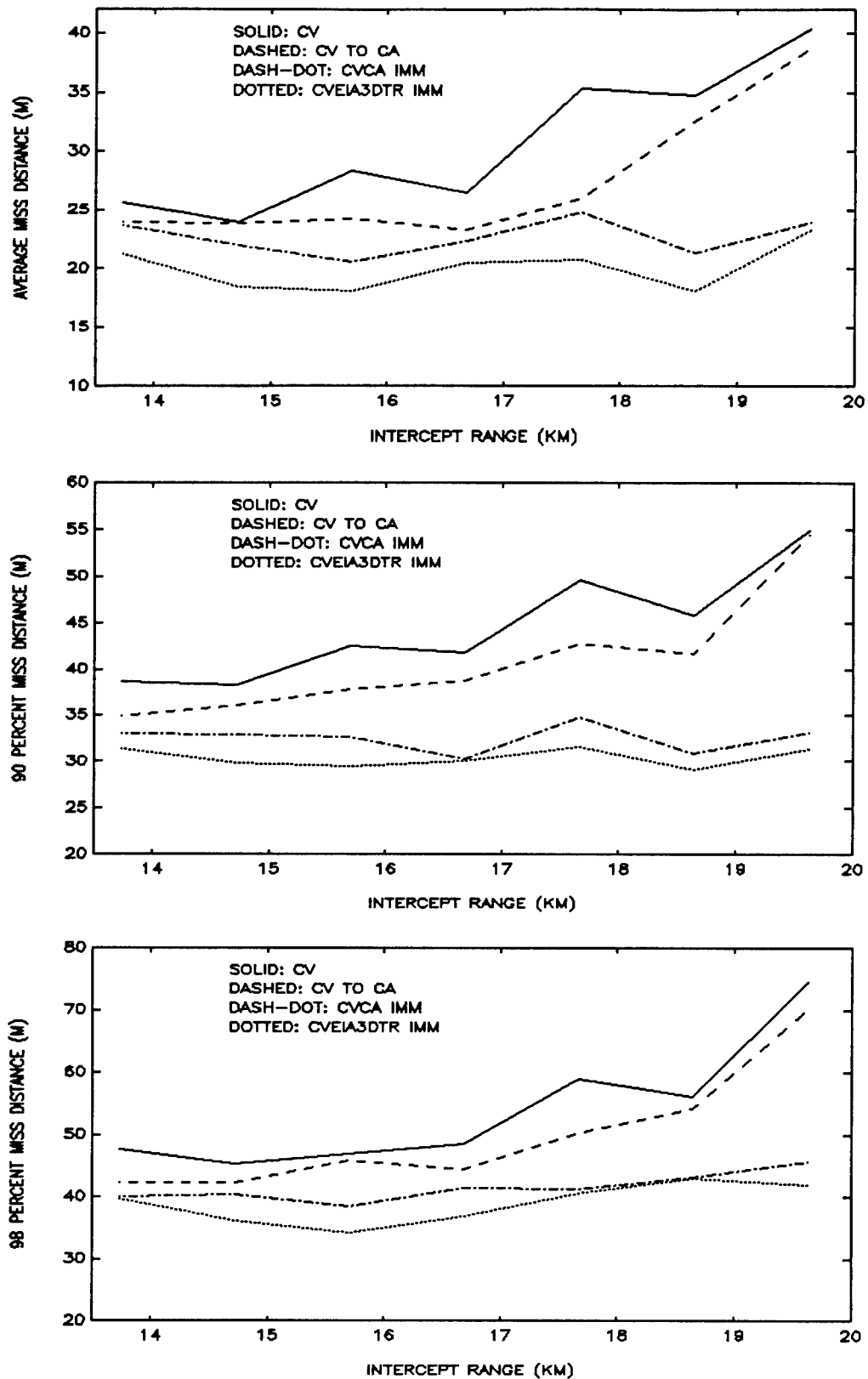


Figure 7-22. Miss Distances for Target 2

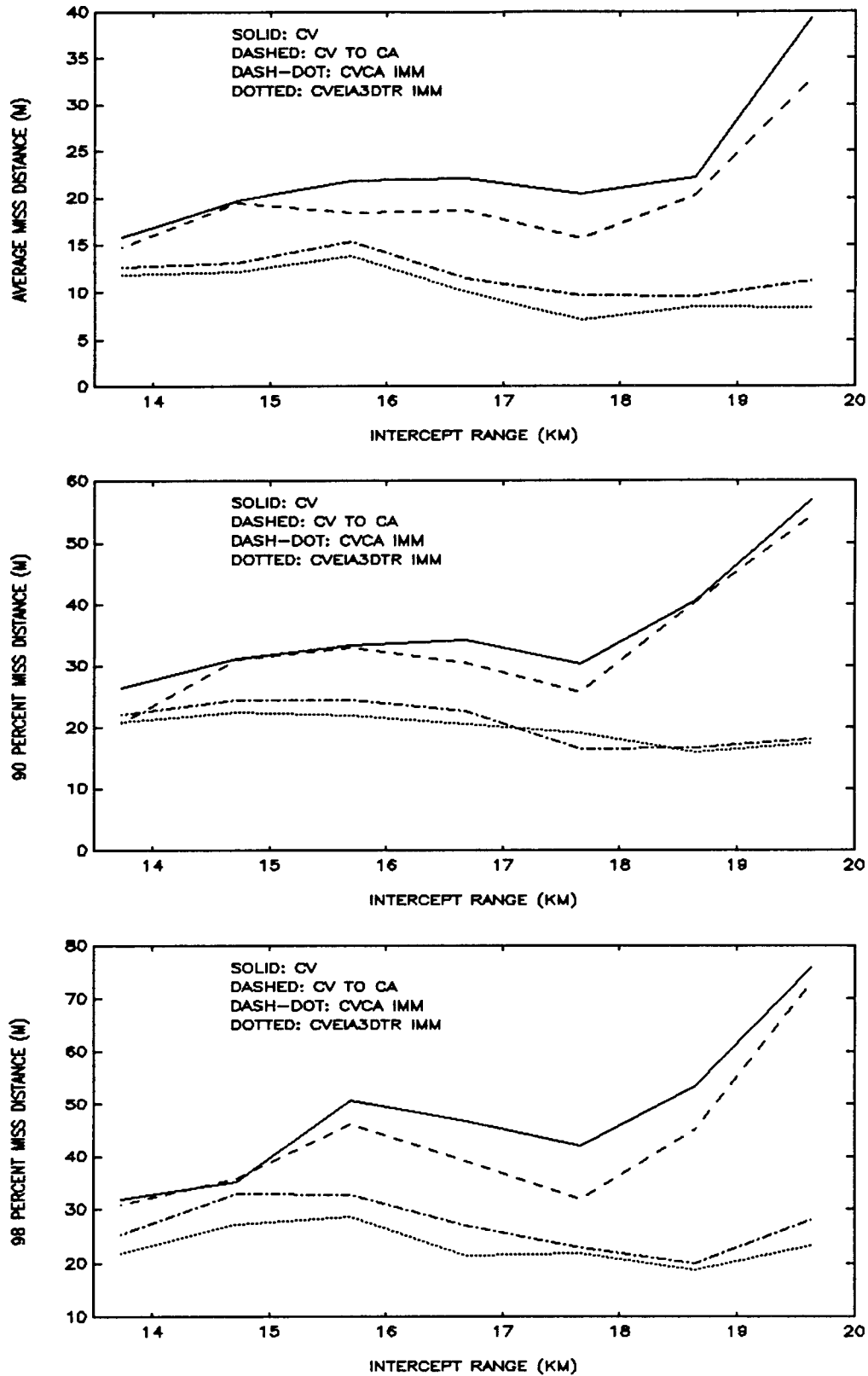


Figure 7-23. Miss Distances for Target 3



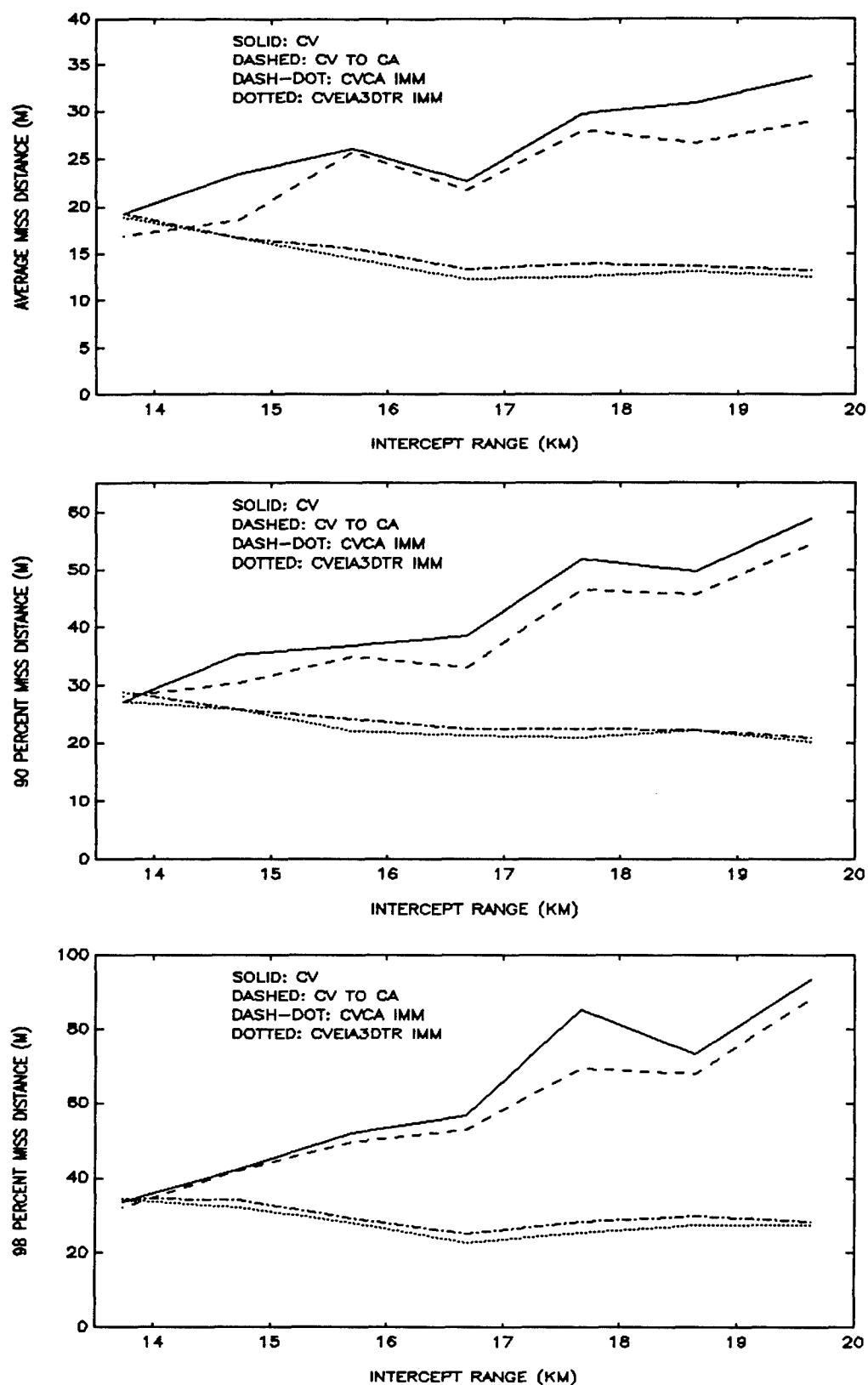


Figure 7-24. Miss Distances for Target 4

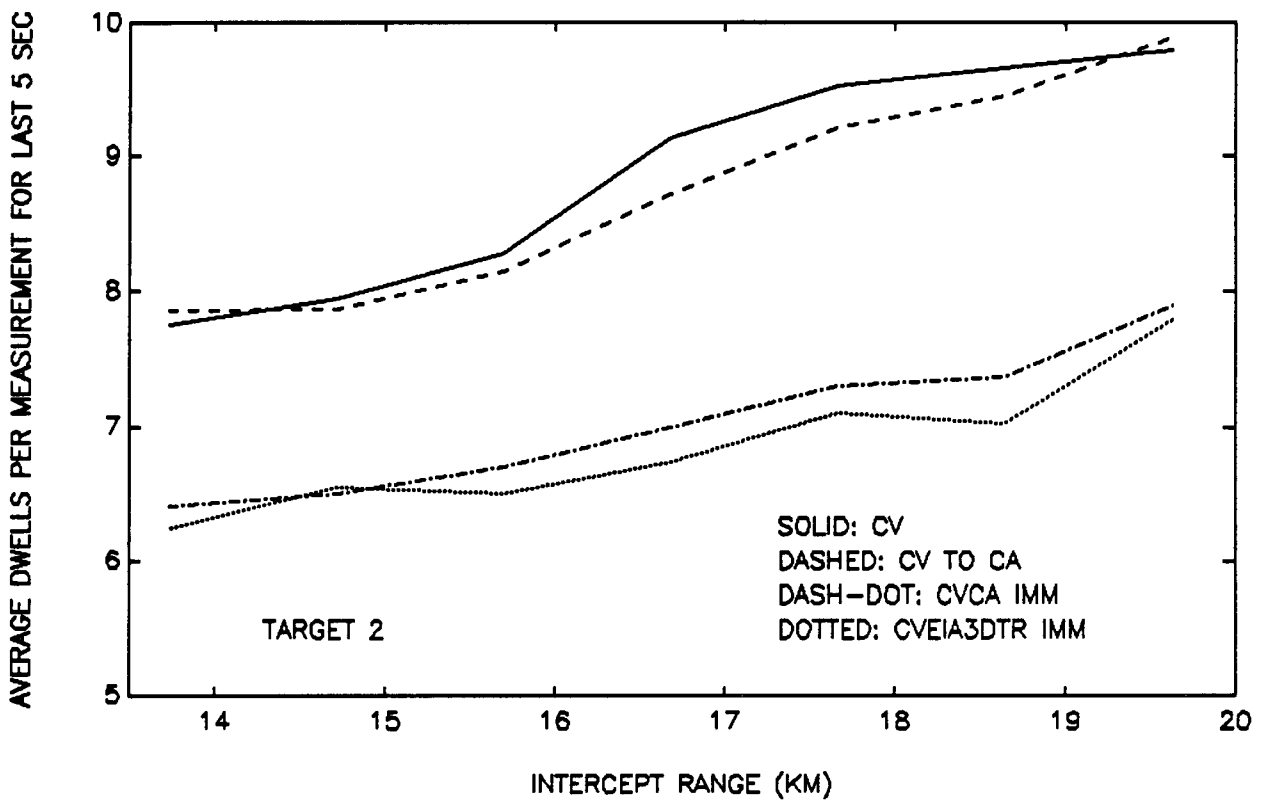
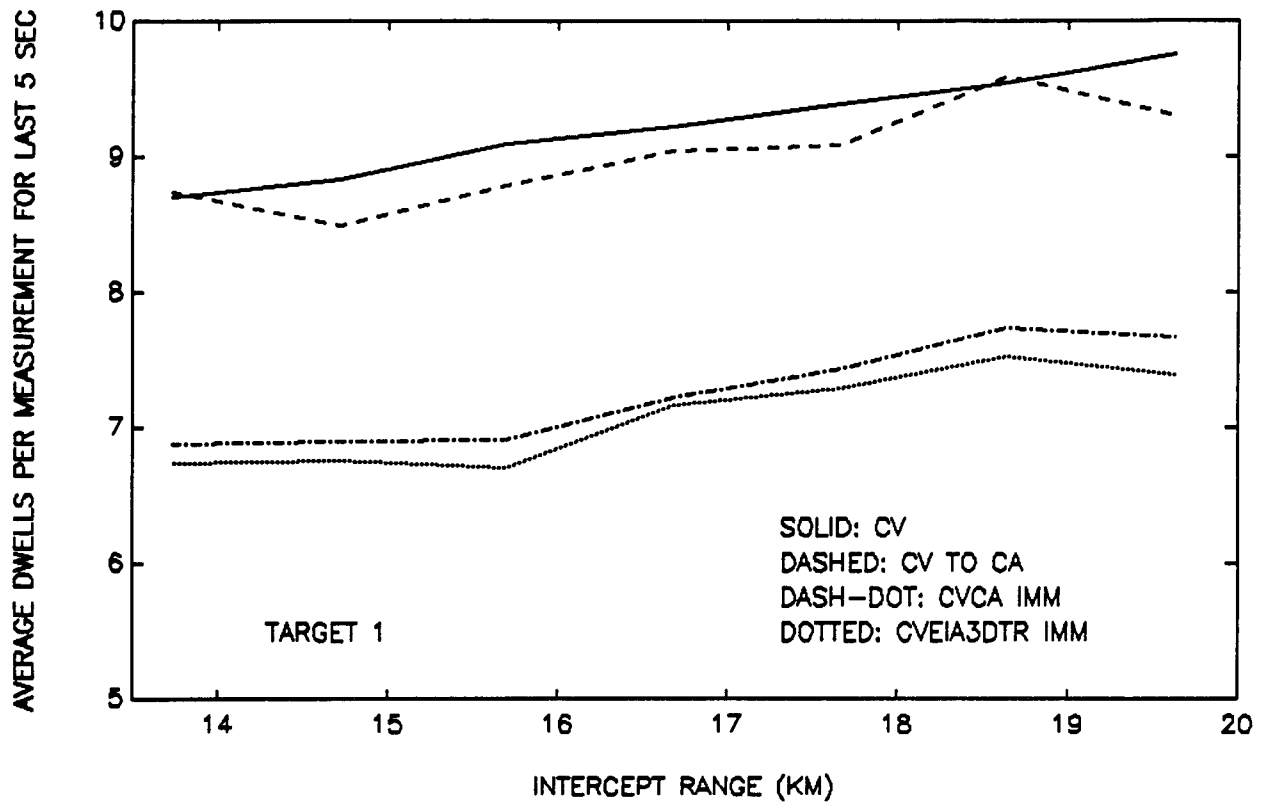


Figure 7-25. Average Number of Dwells Per Measurement for Target 1 and Target 2

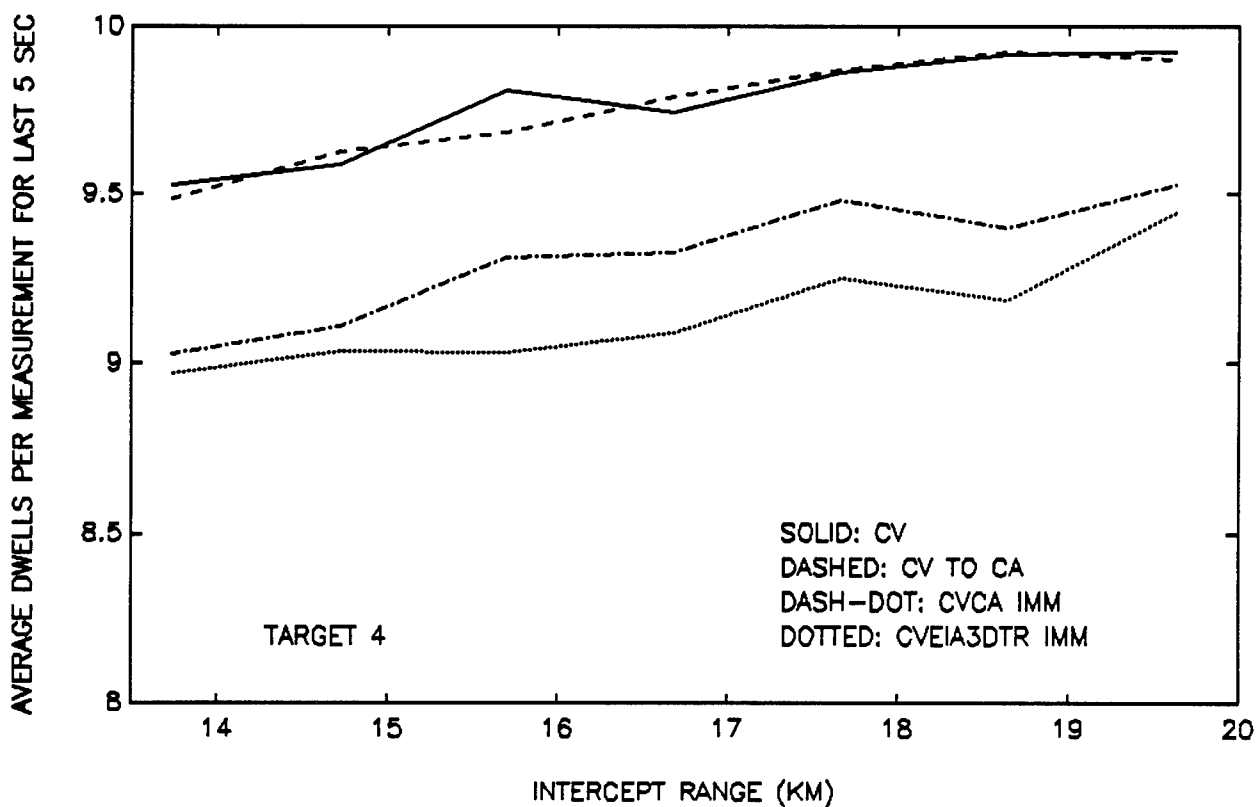
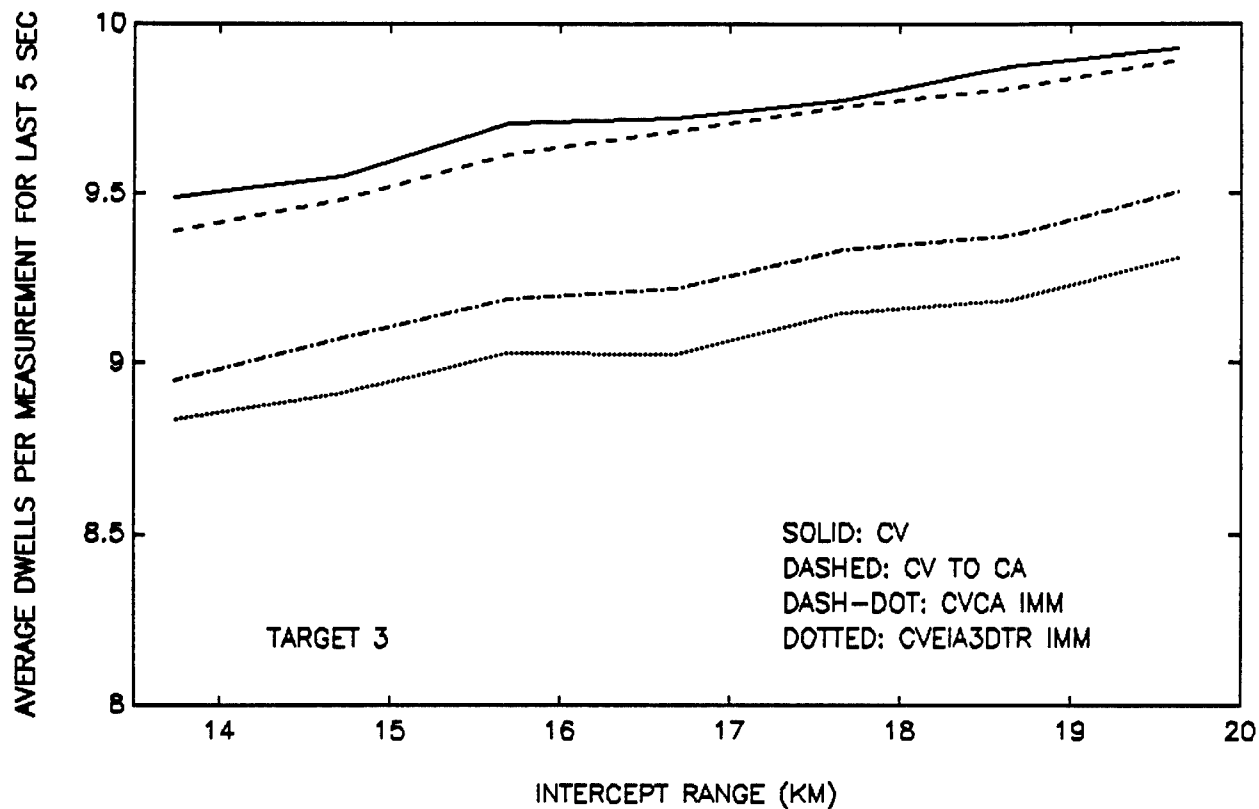


Figure 7-26. Average Number of Dwells Per Measurement for Target 3 and Target 4

## CHAPTER 8

### CONCLUSIONS

The IMM algorithm has been presented for tracking targets in support of CAW intercepts. Two separate IMM tracking filters, a two-model IMM track filter, CVCA, and a three-model IMM track filter, CVEIA3DTR, were tested against two single-model track filters, a CV track filter and a CV track filter switching to a CA track filter during the end game. The IMM tracking filters use multiple motion models with model switching governed by an underlying Markov chain to better represent the target dynamics than a single-model track filter. In CAW intercepts, better tracking leads to more accurate acceleration commands and, thus, lower miss distances are incurred. Initial results against both maneuvering and nonmaneuvering targets, Figures 7-9 through 7-12, indicate that the IMM tracking filters provided smaller miss distances than that of the single-model track filters. To further reduce the miss distance so that the probability of a successful intercept can be increased, numerous guidance techniques and various methods to increase the number of radar dwells during the end game were tested against the most stressful target, Target 4 (Figure 7-4).

All of the different guidance techniques that were tested involved an adjustment of the numerical gain in a PN guidance law given in Eq. (5.5). Increasing the numerical gain yields acceleration commands that are to respond quickly to any target maneuver. However, maintaining a high numerical gain throughout the intercept results in acceleration commands that are in response to noise in the measurements, causing a significant amount of energy of the missile to be expended unnecessarily. By controlling the numerical gain with various techniques, a reduction in the miss distance is achieved. All the methods for adjusting the gain resulted in smaller miss distances, which were 20 m less than the average miss distance without gain adjustment. The method by which the numerical gain was adjusted as a function of an assumed target maximum acceleration, and the assumption that the launch platform is the goal of the target was chosen to be used for the rest of the simulation study. This method yielded slightly smaller average miss distances, and slightly smaller 90 percent and 98 percent miss distances. The 90 percent and 98 percent miss distances are the

distances in which 90 percent and 98 percent of the miss distances were within, respectively.

The different methods tested to increase the number of radar dwells during the end game dramatically reduced all the miss distances. These results are displayed in Figures 7-17 through 7-20. Increasing the number of dwells to  $N$  reduces the standard deviation of the measurement error by  $\sqrt{N}$ . For example, the standard deviation of the angular measurement error used for the simulation studies was  $\sigma_a=0.001$  rad. When the number of dwells are increased to  $N=10$ , the effective angular measurement error is  $\sigma_a=0.001/\sqrt{10}$ . This results in better measurements and thus more accurate acceleration commands to the missile. A method by which the number of dwells  $N$  is calculated as a function of the positional elements of the error covariance matrix (discussed in Chapter 5) proved to yield the lowest miss distances. Using this technique, the IMM track filters not only provided lower miss distances than the single-model track filters, but achieved these lower miss distances with fewer dwells than their single-model counterparts.

Figures 7-21 through 7-24 display the miss distances for each track filter against each target. The IMM track filters provide smaller miss distances for each target. The improvement in the miss distances when using either of the IMM track filters over that of the single-model track filters for the maneuvering targets, Targets 2, 3 and 4, are dramatic. For all the targets, the IMM algorithms achieved these lower miss distances with fewer radar dwells than the single-model track filters. This is seen in Figures 7-25 and 7-26. For the nonmaneuvering target, Target 1, the IMM tracking filters requested approximately 7 dwells per measurement on average, while the single model track filters requested roughly 9 dwells per measurement on average. For the high-speed, highly-maneuvering target, Target 4, both the IMM tracking filters needed just over 9 dwells per measurement on average, and the single model track filters needed nearly 10 dwells per measurement on average. The maximum number of dwells allowed for the simulation was set to 10 dwells per measurement. However, the average miss distance for the IMM track filters is approximately 15 m over all the intercept ranges, while the single-model track filters, CV and CV-CA, have an average miss distance that increases as the intercept range increases, from roughly 20 to 24 m and 17 to 30 m, respectively. With a much greater difference in the respective miss distances, the same trend is observed in the 90 percent and 98 percent miss distances. The reduction in the number of dwells needed by the IMM tracking filters over that of the single-model tracking filters results in a savings of radar energy. This radar energy could then be used to track or search for other targets.

The miss distances presented are for comparison of the relative performance of tracking filters against one another. Systems designed for CAW intercepts would typically have a

smaller standard deviation of the angular measurement error than the  $\sigma_a=0.001$  rad used for the simulation study. Thus, a few additional simulation executions were conducted in which the standard deviation of the angular measurement error was set to  $\sigma_a=0.0005$  rad. Preliminary indications are that this decrease in the angular error cut the miss distances approximately in half. In addition, the number of dwells per measurement in the end game is significantly reduced. An acceptable level of miss distance could be defined by the effective kill radius of the interceptor missile. Due to the smaller miss distances achieved when using the IMM algorithms, incorporating the IMM algorithm into CAW systems will yield a higher probability of kill than the single-model counterparts for a given level of sensor performance.

The IMM algorithm has clearly shown its superiority over the single-model counterparts for target tracking for CAW intercepts. Further research possibilities include implementing other motion models into the IMM framework. Other areas of study would be the use of adaptive sampling techniques with respect to the sample period, and additional examination of guidance techniques.

## REFERENCES

1. Bar-Shalom, Y., and Li, X.R., *Estimation and Tracking: Principles, Techniques, and Software* Artech House, Inc., Boston, 1993.
2. Blackman, S.; Broida, T.J.; and Carter, M.F., *Applications of a Phased Array Antenna in a Multiple Maneuvering Target Environment*, Proceedings of the 20th IEEE Conf. on Dec. and Cont., San Diego, CA, Dec 1981, pp. 1413-1418.
3. Blom, H.A.P., and Bar-Shalom, Y. *The Interacting Multiple Model Algorithm for Systems with Markovian Switching Coefficients*, IEEE Transactions on Automatic Control, vol. AC-33, Aug 1988.
4. Bar-Shalom, Y.; Chang, C.Y.; Blom, H.A.P. *Tracking a Maneuvering Target Using Input Estimation Versus the Interacting Multiple Model Algorithm*, IEEE Trans. Aero. Elect. Syst., AES-25, 1989, pp. 296-300.
5. Tugnait, J.C. *Detection and Estimation for Abruptly Changing Systems*, Automatica, 1982, pp. 607-615.
6. Blair, W.D.; Watson, G.A.; and Hoffman, S.A., *Benchmark Problem for Beam Pointing Control of Phased Array Radar Against Maneuvering Targets*, Proc. of American Control Conference, Baltimore, MD 29 June - 1 July, 1994.
7. Blair, W.D., and Watson, G.A. *IMM Algorithm for Solution to Benchmark Problem for Tracking Maneuvering Targets*, Proc. of SPIE Acquisition, Tracking, and Pointing VIII, Orlando, FL, Apr 1994.
8. Watson, G.A., and Blair, W.D. *IMM Algorithm for Tracking Targets that Maneuver Through Coordinated Turns*, Proc. of SPIE Signal and Data Processing of Small Targets 1992, Orlando, FL, Apr 1992, pp. 236-247.
9. Blair, W.D.; Watson, G.A.; and Alouani, A.T. *Use of Kinematic Constraint for Tracking Constant Speed Maneuvering Targets*, Naval Surface Warfare Center, NAVSWC TR 91-561, Dahlgren, VA.
10. Blair, W.D., and Watson, G.A. *IMM Algorithm and Aperiodic Data*, Proc. of SPIE Acquisition, Tracking, and Pointing VI, Orlando, FL, Apr 1992, pp. 83-89.
11. Guelman, M., "The Closed-Form Solution of True Proportional Navigation," 1976, *IEEE Transactions on Aerospace and Electronics Systems*, Vol. 12, No. 4, pp. 472-482.

**APPENDIX A**  
**AERODYNAMIC DRAG ANALYSIS**



In the CAW simulation, the interceptor missile flight is obtained through the implementation of a fourth-order Runge-Kutta technique. The acceleration due to drag affects the flight of the interceptor missile, and is thus incorporated into the simulation.

The force of drag on a missile is the sum total of the drag forces due to skin friction, forebody pressure, base pressure, and drag due to lift. The drag due to the winglets and control surfaces, though significant, are not considered. This is done to simplify the missile design, which can now be approximated as a slender, circular body. Quantities of the atmosphere, such as the air pressure, density, temperature and viscosity need to be calculated to obtain a more accurate model of the drag. Each of these quantities vary with altitude. As altitude increases, temperature and viscosity decreases. Pressure and density also decrease as altitude increases. The functions for the atmospheric quantities were incorporated into the calculation for drag through the use of polynomial fitting of data found in a standard atmospheric table.

The force of drag must be analyzed for each of the different speed regions of interest. These regions are supersonic flow, subsonic flow, and transonic flow. The first region to be evaluated is the region of supersonic flow.

## SUPERSONIC FLOW

Skin friction drag is a function of the density, temperature, and viscosity of the surrounding fluid, in addition to the Mach number of the fluid with respect to the missile. In incompressible fluid flow, Bernoulli's principle states that as long as no momentum is added or taken away from a given stream of fluid, the sum of the static and dynamic pressures remain a constant. As a result, the dynamic pressure  $q_0 = .5\rho V^2$ , where  $\rho$  is the density of the fluid and  $V$  is the relative velocity of the fluid over the missile, is converted into a static pressure differential; which has magnitude  $.5\rho V^2$  at every stagnation point. However, in supersonic flow, the fluid is compressible. In a compressible fluid, the temperature changes as a function of pressure, and an exchange of kinetic energy to heat energy takes place. Therefore, constant total energy replaces Bernoulli's constant. Upon obtaining a certain speed, a portion of the kinetic energy of the fluid particles is transformed to heat. The equation for the change in temperature of the fluid is, from Reference A-1,

$$\frac{\Delta T}{T_{amb}} = 0.5(\gamma - 1)(V^2 - w^2)/(c)^2 \quad (A.1)$$

where  $T_{amb}$  is the ambient absolute temperature,  $w$  is local velocity at a given point,  $\gamma$  is

the specific heat ratio, and  $c$  is the speed of sound for the conditions of the ambient fluid. Since the surrounding fluid is air, the value of  $\gamma = 1.4$ . Eq. (A.1) can be rewritten as

$$\frac{\Delta T}{T_{amb}} = .2 M^2 \left( 1 - \left( \frac{w}{V} \right)^2 \right) \quad (A.2)$$

where  $M = V/c$  is the Mach number. A stagnation point has zero local velocity  $w$ , so

$$\Delta T = .2 T_{amb} M^2 \quad (A.3)$$

Because of this increase in temperature within the boundary layer as the Mach number increases, the skin friction drag tends to decrease as a function of Mach number. This is explained in the following manner. On the surface of the missile, the tangential fluid flow is zero. The temperature is consequently increased as shown in Eq. (A.3). The average density within the boundary layer of the missile is reduced accordingly in the proportion of  $\rho \sim 1/T_{bl}$ , where  $T_{bl}$  is the temperature of the boundary layer. Thus, from Reference A-1,

$$\frac{\rho_{amb}}{\rho_{bl}} = \frac{T_{amb}}{T_{bl}} = \frac{1}{(1 + OM^2)} \quad (A.4)$$

where  $O$  is a suitable integration constant. The skin friction drag is also a function of viscosity,  $\mu$ , which is roughly

$$\frac{\mu_{bl}}{\mu_{amb}} = \frac{T_{bl}}{T_{amb}} \quad (A.5)$$

There are two types of boundary layers, laminar and turbulent. In most applications, the boundary layer surrounding the missile will initially be laminar; upon reaching a high Reynolds number, in the vicinity of  $1 \times 10^6$ , the boundary layer is considered turbulent. The Reynolds number,  $Re$ , at a point is defined as

$$Re = \frac{\rho_0 V_0 D}{\mu_0} \quad (A.6)$$

where  $D$  is the distance from the leading edge of the body. Due to the high velocities encountered in supersonic flow, it is assumed that the Reynolds number will be great enough to cause a turbulent boundary layer a short distance behind the leading edge of the missile. Thus the entire boundary layer will be treated as though it were turbulent.

The drag force,  $D_f$ , due to skin friction is approximated in Reference A-1 by

$$D_f \sim \frac{\rho}{Re^{1/6}} \sim \mu^{1/6} \rho^{5/6} \sim \frac{\left( \frac{T_{bl}}{T_{amb}} \right)^{1/6}}{\left( \frac{T_{bl}}{T_{amb}} \right)^{5/6}} = \left( \frac{T_{bl}}{T_{amb}} \right)^{-2/3} \sim \left( \frac{1}{1 + OM^2} \right)^{2/3} \quad (A.7)$$

A more accurate solution without experimentation is extremely difficult. There are more than a dozen different theoretical solutions for skin friction drag in a turbulent boundary layer. This makes the constant  $O$  difficult to analyze. According to Reference A-1, an appropriate value is  $O = 0.15$ . Also, for  $O = 0.15$ , the exponent 0.58 rather than  $2/3 = 0.66$  is used. This is based on experiments conducted on different bodies at various Reynolds numbers with the condition of no heat transfer taking place between the missile skin and the surrounding fluid. Substituting these values into Eq. (A.7) and rewriting the drag in terms of coefficients of drag yields the following:

$$c_{f_e} = (1 + 0.15M^2)^{-0.58} c_{f_i} \quad (A.8)$$

where  $c_{f_e}$  is the computed supersonic skin friction drag coefficient, and  $c_{f_i}$  is the coefficient of drag due to skin friction for incompressible, subsonic flow. This coefficient will be described in the section on incompressible, subsonic flow.

For this evaluation, the missile in question is assumed to be a cylinder with a conical nose section. The forebody pressure drag depends on two independent factors, the semi-apex angle of the nose cone, and the Mach number. Since the drag on the forebody at supersonic speeds is inherently due to the increase of pressure across the shock wave, the correlation of the Mach number to the forebody pressure drag can then be found through the calculation of the pressure coefficient. Applying the hypersonic similarity law, the drag coefficient of a cone, based on the base area of the cone, is equal to the usual pressure coefficient

$$c_{d_w} = \frac{p - p_0}{p_0} \frac{p_0}{q_0} = \frac{p - p_0}{p_0} \left( \frac{\gamma}{2} M_0^2 \right)^{-1} \quad (A.9)$$

Thus, as the Mach number increases, the coefficient of drag decreases. A more difficult problem is the correlation of the cone semi-apex angle to the calculation of drag. Drag coefficients as a function of Mach number and the cone semi-apex angle, is shown in Figure A-1. These drag coefficients, obtained from Missile Aerodynamics, Reference A-2, are the result of experimentation and testing the results against the hypersonic similarity parameter theory. The correlation between the experimental results and the expected results was excellent for cones of semi-apex angle of less than 30 deg and up to a speed of Mach 8. However, the correlation suffers when either of these two parameters are exceeded.

The next type of drag to be analyzed is base pressure drag. To examine base pressure drag, an understanding of the viscous flow about the base needs to be understood. Figure A-2 is shown to aid in the explanation of the base pressure drag.

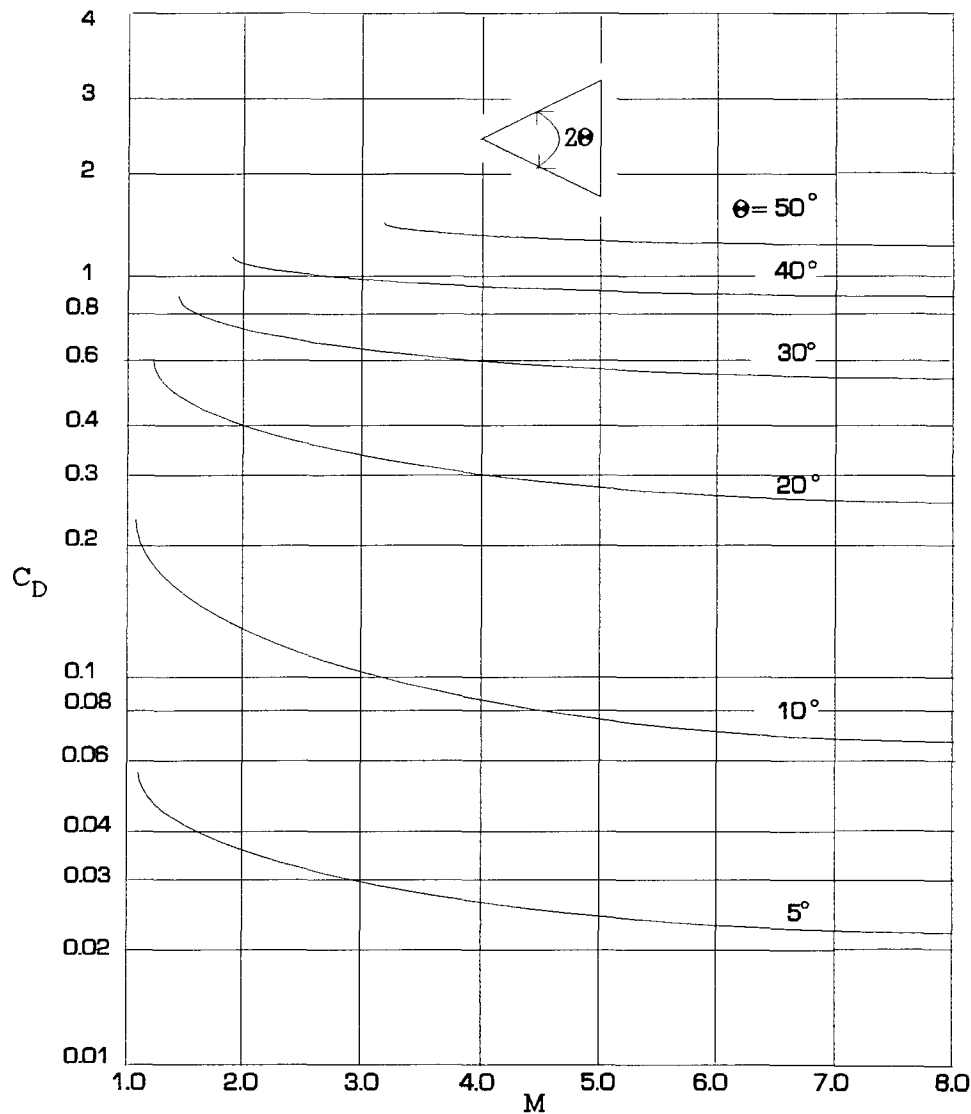


Figure A-1. Drag coefficients of cones at supersonic speeds

Directly behind the blunt base of the missile is a circulating region of fluid known as the dead water region with pressure  $p_b$ . Enclosing the dead water region is the boundary layer from the blunt base. Enclosing the boundary layer is the outer potential flow. The boundary layer increases in thickness as it mixes with the air in the dead water region. The boundary layer converges to a point on the centerline of the missile known as the reattachment point. The boundary layer then straightens out in the streamwise direction further downstream. In the discussion of the skin friction drag, the boundary layer was assumed to be turbulent. That assumption will continue in the evaluation of base pressure drag. The equation for base pressure drag is

$$D_b = \Delta P_B S(1) \quad (A.10)$$

where  $\Delta P_B$  is the change in the base pressure coefficient and  $S(1)$  is the area of the base of

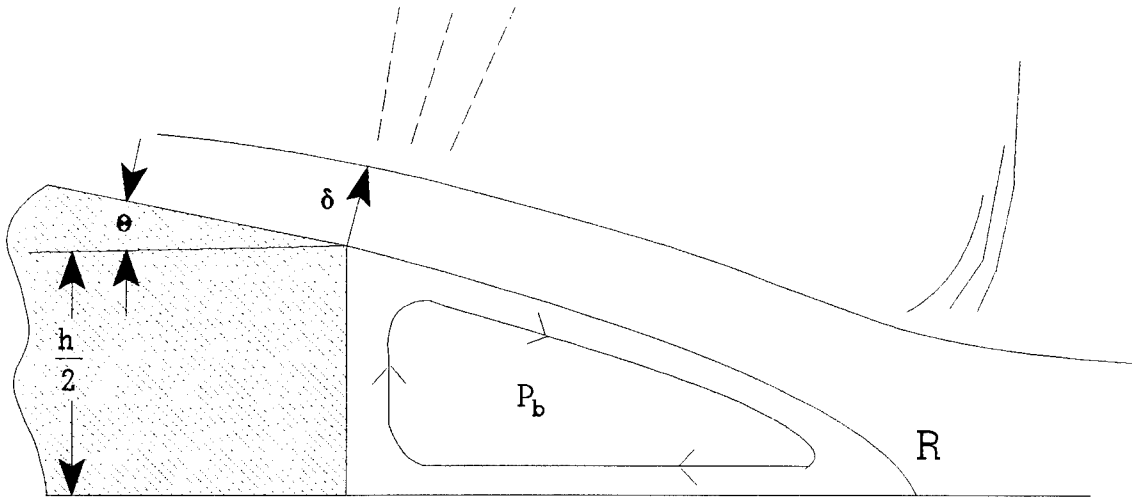


Figure A-2. Theoretical model of flow behind a blunt base

the missile. The change in the base pressure coefficient is defined as

$$\Delta P_B = \left(1 - \frac{p_b}{p_0}\right) \frac{1}{2} \gamma p_0 M_0^2 \quad (\text{A.11})$$

where  $p_0$  is the free-stream static pressure,  $p_b$  is the static pressure of the dead water region, and  $M_0$  is the free-stream Mach number. For a given missile at known flight conditions, the only unknown is the ratio  $p_b/p_0$ . The largest factor influencing this ratio is the Mach number.

Experimental results given in Reference A-2 expresses the ratio  $p_b/p_0$  as a function of Mach number for bodies of revolution with fully turbulent boundary layers. The results are seen in Figure A-3. By using the results in Figure A-3, a calculation of the base pressure drag can be found.

The last term to evaluate is the drag due to lift. Consider a missile in straight, unaccelerated, level flight. At this point in time, it is assumed that the angle of attack  $\alpha$ , and the angle of sideslip,  $\beta$  are zero. Consequently, the thrust of the missile is equal to the drag, and the lift is equal to the weight of the missile. For this flight attitude to change, a moment is created about one axis of the missile. This moment is typically achieved either by a vectoring thrust nozzle or by small winglets on the missile body. This moment will cause an angle to form between the longitudinal axis of the missile and the velocity vector, thus creating lift perpendicular to the velocity vector in accordance to either the angle of attack  $\alpha$  or the angle of sideslip  $\beta$ . The same pressure forces that cause the force of lift also have a component parallel to the velocity vector, which is the drag.

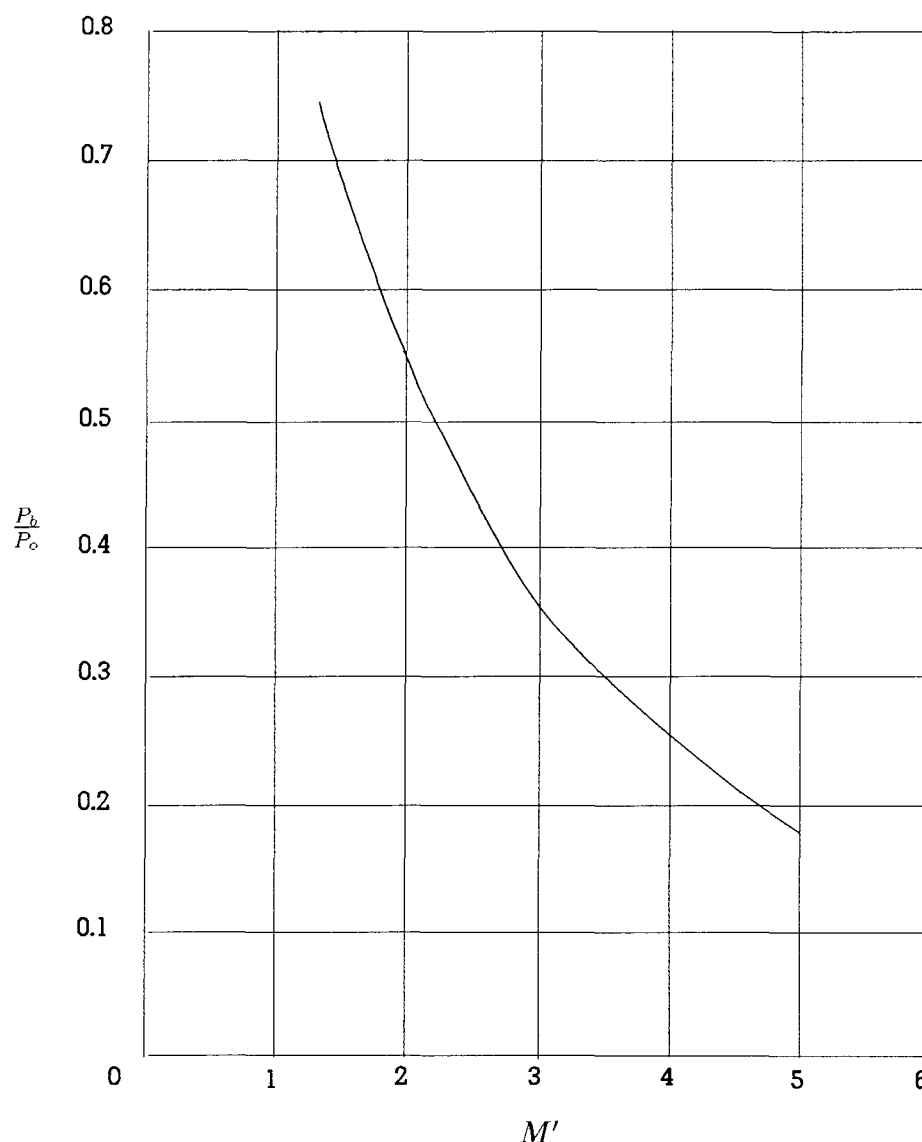


Figure A-3. Base pressure correlation for bodies of revolution with relatively thin turbulent boundary layers

For speeds in the supersonic regime, the coefficient of lift,  $c_l$  is defined as

$$c_l = \frac{4\alpha}{\sqrt{M_0^2 - 1}} \quad (\text{A.12})$$

This equation holds true regardless of the shape or the thickness of the airfoil in question. The coefficient of drag due to lift,  $c_{d_l}$  in the supersonic regime is defined to be

$$c_{d_l} = c_l \alpha \quad (\text{A.13})$$

Substituting Eq. (A.12) into Eq. (A.13), the coefficient of drag due to lift is calculated to

be

$$c_{d_{l\alpha}} = \frac{4\alpha^2}{\sqrt{M_0^2 - 1}} \quad (A.14)$$

These same equations can be used to calculate the drag due to the lift in the horizontal plane using the sideslip angle  $\beta$ . In this case, the angle  $\alpha$  is replaced with the angle  $\beta$ . It should be noted that the angle of roll is not used because that a missile with a symmetrical body does not roll to turn like an aircraft.

With all the terms now evaluated, the total force of drag in supersonic flow is

$$D = (c_{f_c} S_{f_c} + c_{d_w} S_{d_w} + (c_{d_{l\alpha}} + c_{d_{l\beta}}) S_{d_l}) \frac{\gamma}{2} p_0 M_0^2 + D_b \quad (A.15)$$

where  $S_{f_c}$  is the total surface area of the body,  $S_{d_w}$  is surface area of the missile nose cone, and  $S_{d_l}$  is the missile characteristic lifting body area.

## SUBSONIC FLOW

The force due to drag in subsonic flow is similar to the drag in supersonic flow, except effects due to compressibility are not applicable. The drag in subsonic flow is evaluated for each type of drag found on the missile.

The drag due to skin friction is dependent on the type of velocity boundary layer that is present (i.e., laminar or turbulent). The Reynolds number will determine the type of boundary layer present. The transition from laminar to turbulent will occur at a Reynolds number, as described in Eq. (A.6) of approximately  $1 \times 10^6$ . The determination of both the boundary layer and the Reynolds number will determine the skin friction coefficient. Skin friction within a laminar boundary layer is considered first.

In a laminar boundary layer, the particles of the fluid move along lines that are essentially parallel to each other, with velocities that are locally constant. The definitions of the skin friction coefficient and the Reynolds number are described in such a fashion that the coefficient of skin friction can be calculated, for a laminar boundary layer according to Reference A-1,

$$c_{f_i} = \frac{0.664}{\sqrt{Re}} \quad (A.16)$$

where  $Re$  is the Reynolds number calculated at the base of the missile. The Reynolds number is then calculated as

$$Re = \frac{\rho_0 V_0 L}{\mu_0} \quad (A.17)$$

where  $L$  is the surface length from nose cone tip to the base of the missile.

If the boundary layer is turbulent, the average skin friction coefficient can be determined by using the calculated Reynolds number and using the relationship of Prandtl-Schlichting, Reference A-1,

$$c_{fi} = \frac{0.455}{(\log Re)^{2.58}} \quad (A.18)$$

The Eqs. (A.16) and (A.18) are for the calculation of the skin friction drag coefficient in subsonic flow. The force due to skin friction drag in subsonic flow is then calculated as

$$D_{fi} = c_{fi} \frac{\rho_0}{2} V_0^2 S \quad (A.19)$$

where  $S$  is the total surface area of the missile.

The forebody pressure drag will be calculated for zero angle of attack to eliminate any type of crossflow pattern that may develop over the nose and body of the missile. This simplifies the calculation of the forebody pressure drag.

To help visualize the effect of the forebody pressure drag, consider a flat plate with area  $A$ . The force exerted on the plate is

$$F = \frac{\rho_0}{2} V_0^2 A \sin \psi \quad (A.20)$$

where  $\psi$  is the angle of incidence between the relative velocity and the plate. When the angle  $\psi$  is zero, the plate lays flat, and since the thickness of the plate is essentially zero, the force exerted on the plate is zero. The plate feels the full effect of the force exerted by the fluid when the angle  $\psi$  is 90 deg.

The same type of evaluation is used for the nose of the missile. The nose of the missile in question is assumed to be a cone with a circular base and a semi-apex angle of  $2\theta$ . The surface of the cone is at an angle of incidence to the fluid of  $\theta$ , or half of the semi-apex angle. Thus the drag force on the forebody of the missile is

$$D_{fb} = c_{fb} \frac{\rho_0}{2} V_0^2 S_c \quad (A.21)$$

where

$$c_{fb} = \sin \theta \quad (A.22)$$

and  $S_c$  is the frontal area of the cone.

At the base of the missile, the difference in pressure of the "dead water" region created behind the missile to the free-stream pressure creates a retarding force known as base



pressure drag. This particular force is difficult to analyze without the use of experimental results. Experiments for three dimensional bodies has been performed by Sighard Hoerner for his book Fluid-Dynamic Drag, Reference A-1. Through his experiments, he was able to approximate the coefficient of drag due to base pressure as a function of the coefficient of drag due to forebody pressure. This function is

$$c_{db} = \frac{0.029}{\sqrt{c_{fb}}} \quad (A.23)$$

The force of drag due to base pressure is then calculated as

$$D_{db} = c_{db} \frac{\rho_0}{2} V_0^2 S_c \quad (A.24)$$

The drag due to lift of a body of circular base is considered within the realm of slender body theory. The equation of drag due to lift is formulated to be

$$D_l = \frac{\alpha}{2} \bar{Z} \quad (A.25)$$

where  $\bar{Z}$  is defined as the force of lift on the missile. It is interesting to note that the drag on a slender body is one-half that for a flat plate. Therefore, to calculate the drag on the missile, the force of lift must also be calculated. The lift on a body with a circular base is given by

$$L_\alpha = 2\pi r_0^2 \alpha q_0 \quad (A.26)$$

where  $r_0$  is the radius of the circular base,  $\alpha$  is the angle of attack, and  $q_0$  is the dynamic pressure. Substituting Eq. (A.26) into Eq. (A.25) yields

$$D_{l_\alpha} = \pi r_0^2 \alpha^2 q_0 \quad (A.27)$$

where

$$q_0 = \frac{\rho_0 V_0^2}{2} \quad (A.28)$$

The same equations can be used for the lift in the horizontal plane due to a sideslip angle  $\beta$ . Since the missile is a symmetric body, the lift Eq. (A.26) is applicable. Thus the force of lift in the horizontal plane is

$$L_\beta = 2\pi r_0^2 \beta q_0 \quad (A.29)$$

Therefore the drag due to the lift in the horizontal plane is

$$D_{l_\beta} = \pi r_0^2 \beta^2 q_0 \quad (A.30)$$

where  $q_0$  is defined in Eq. (A.28).

The total force of drag in subsonic flow on the particular missile is the sum of all the components of the drag.

$$D = D_f + D_{fb} + D_{db} + D_{l_\alpha} + D_{l_\beta} \quad (A.31)$$

## TRANSONIC FLOW

An extended range of speeds in the vicinity of Mach 1 is called the transonic region. It is in this region that the fluid interacting with the body does not exhibit purely subsonic characteristics or purely supersonic characteristics. This region typically ranges from  $0.70 < M < 1.4$ . Depending on the shape and the dynamics of the body in question, the transonic region can include a larger or smaller region of speeds.

The missile in question is assumed to have a conical nose and a cylindrical body. The drag on the missile in the transonic region can be obtained by combining transonic cone theory and transonic base drag theory.

The pressure on the cone starts from a stagnation point on the tip of the cone and reduces along the length of the cone to values less than the ambient pressure at the cone's rim. Theoretical methods have been established that correlate the change in pressure along the length of the cone by means of several similarity functions. Most of these methods employ linearized terms that are accurate only for very small cone angles. Relying on Reference A-1, a statistical approach is taken. One of the similarity function components that is taken into account is the slope of the drag coefficient across Mach = 1

$$\frac{dc_d}{dM} = \left( \frac{4}{(\gamma + 1)} \right) (1 - 0.5c_{d_0}) \quad (A.32)$$

where  $c_{d_0}$  is the drag coefficient at Mach = 1. This empirical function is relatively accurate in comparison to experimental results obtained in Reference A-3. The drag coefficient of the conical nose reaches a peak soon after Mach = 1. After this peak is reached, the coefficient of drag on the missile reduces as a function of the Mach number until pure supersonic theory takes hold. This function is approximated by

$$c_{d_i} = \frac{c_{d_i}}{\sqrt{M^2 - 1}} \quad (A.33)$$

where  $c_{d_i}$  is the coefficient of drag if subsonic theory was applied to the missile for the given transonic velocity.

Because of the absence of truly supersonic flow in the transonic region, the base pressure drag is a result of viscous mixing that occurs in the wake of the missile, rather than the expected results of supersonic flow. The resultant wake is dependent on both the length of the missile and the diameter of the missile body. Statistical evaluations have been performed that relate the ratio of lift over diameter to evaluate the base pressure drag. However, there is currently no complete solution to the problem of base pressure drag, and theoretical examinations have been performed but they do not accurately compare to the experimental results.

For the case of a generic missile where experimental data from wind tunnel tests are not available, defining the transonic region becomes inherently difficult. Using data from other missiles and results in both Reference A-1 and Reference A-2, the transonic region in the interceptor simulation was defined to be the region of speeds from  $0.8 < M < 1.4$ .

It is in this transonic region that the value of the total coefficient of drag will take on a maximum. This maximum does not necessarily occur at  $M = 1$ . As is the case for conical flow, flow over the nose cone, the maximum will occur slightly higher than  $M = 1$ . The exact value of the Mach number at which this occurs is impossible to determine without experimentation. Thus a value for the Mach number at which the maximum occurs had to be estimated. Using the resources available, the Mach number for which the total coefficient of drag is a maximum is assumed to be  $M = 1.05$ .

For there to be a smooth transition from subsonic theory to transonic theory to supersonic theory, polynomial fitting was performed. This was executed by taking calculated data from both the subsonic and supersonic regions, where the theory is better defined, and also taking calculated data from the transonic region, this data is then executed through a polynomial fitting function, which calculates a sixth-order polynomial that will incorporate the given data. In doing this, the transitions from subsonic to transonic and from transonic to supersonic are "smooth".

## CALCULATION OF ANGLE OF ATTACK AND SIDESLIP

Both the angle of attack ( $\alpha$ ) and the angle of sideslip ( $\beta$ ) are necessary in the calculation

of drag on the missile. These angles are used to determine the drag due to lift and the drag due to yaw, and are based on the angles necessary to achieve a commanded acceleration. These angles are the angles between the body axis of the missile and the velocity vector. The body axis of the missile is defined as having the  $x$  axis pointing through the nose cone and its origin at the center of pressure. The  $z$  axis along with the  $x$  axis form a plane of symmetry about the missile.

It should be noted that the missile is assumed to be a symmetric body and unlike an aircraft does not have to "roll" large airfoils to turn. Typical means of turning are thrust vectoring and/or small fins symmetrically placed about the circumference of the missile, which cause an angle of attack or sideslip.

These angles are also different according to whether the missile is in subsonic or supersonic flow. For the calculation of these angles, the transonic region was omitted and the supersonic region was taken to be any speed above and including Mach 1.

For both subsonic and supersonic flow, the angles  $\alpha$  and  $\beta$  can be found by the incorporation of the lift coefficient. For subsonic flow, the relation between coefficient of lift and the angle  $\alpha$  is given in Reference A-3 as

$$\alpha = \frac{c_l}{\pi A} \quad (A.34)$$

where  $c_l$  is the coefficient of lift and  $A$  is the aspect ratio of the missile. The coefficient of lift is defined as

$$c_l = \frac{L}{\frac{1}{2} \rho_0 V_0^2 S} \quad (A.35)$$

where  $L$  is the lift and  $S$  is the characteristic area of the missile. For a flat plate, the aspect ratio is the span squared over the area of the plate, thus for a cylindrical missile, the aspect ratio is the circumference squared over the characteristic area,

$$A = \frac{(\pi d)^2}{S} \quad (A.36)$$

where  $d$  is the diameter of the missile. Substituting Eqs. (A.35) and (A.36) into Eq. (A.34) yields the following

$$\alpha = \frac{L}{\frac{1}{2} \rho_0 V_0^2 \pi^3 d^2} \quad (A.37)$$

Lift can be defined with respect to the commanded acceleration of the missile in the  $z$  direction of the body axis system, which requires an angle  $\alpha$ , and the commanded horizontal

acceleration, or yaw, in the  $y$  direction of the body axis system, requiring an angle  $\beta$ . For straight and level flight, the lift is equal to the weight of the missile. For a pitch up of four times the force of gravity, the magnitude of the lift is four times greater than the weight. Thus,

$$L = nm g = \left( \frac{\ddot{z}_v}{9.81} \right) m g = \ddot{z}_v m \quad (A.38)$$

where  $n$  is the number of "g's",  $\ddot{z}_v$  is the acceleration of the missile perpendicular to the velocity vector and in the  $x - z$  plane of the body axis system.

The velocity of the missile is also known

$$V_0^2 = \dot{x}^2 + \dot{y}^2 + \dot{z}^2 \quad (A.39)$$

Eqs. (A.39) and (A.38) are substituted into Eq. (A.37) to give the result

$$\alpha = \frac{\ddot{z}_v m}{\frac{1}{2} \rho_0 (\dot{x}^2 + \dot{y}^2 + \dot{z}^2) \pi^3 d^2} \quad (A.40)$$

This same evaluation can be done for the calculation of the angle  $\beta$  in subsonic flow. Substituting  $\ddot{y}_v$  in for  $\ddot{z}_v$ , which is the acceleration of the missile perpendicular to the velocity vector and in the  $x - y$  plane of the body axis system. The equation for the angle  $\beta$  is

$$\beta = \frac{\ddot{y}_v m}{\frac{1}{2} \rho_0 (\dot{x}^2 + \dot{y}^2 + \dot{z}^2) \pi^3 d^2} \quad (A.41)$$

For supersonic flow, the evaluation of the angles  $\alpha$  and  $\beta$  is only slightly different. In supersonic flow, the coefficient of lift, regardless of shape is

$$c_l = \frac{4\alpha}{\sqrt{M_0^2 - 1}} \quad (A.42)$$

where the lift is in the  $z_v$  frame described earlier. The coefficient of lift is also defined as, in supersonic flow,

$$c_l = \frac{L}{\frac{1}{2} \gamma p_0 M_0^2 S} \quad (A.43)$$

where  $p_0$  is the ambient air pressure,  $\gamma$  is the ratio of specific heats, and  $S$  is the characteristic lifting body area of the missile.

Incorporating the value of lift as defined in Eq. (A.38), and solving for the angle  $\alpha$  in Eq. (A.42) yields

$$\alpha = \frac{\bar{z}_v m \sqrt{M_0^2 - 1}}{2\gamma p_0 M_0^2 S} \quad (A.44)$$

This same evaluation can be done for the calculation of the angle  $\beta$  in supersonic flow. Once again, substituting  $\bar{y}_v$  in for  $\bar{z}_v$ . The equation for the angle  $\beta$  in supersonic flow is

$$\beta = \frac{\bar{y}_v m \sqrt{M_0^2 - 1}}{2\gamma p_0 M_0^2 S} \quad (A.45)$$

## REFERENCES

- A-1. Hoerner, Sighard F., *Fluid-Dynamic Drag*, Published by the Author, 1965, copyright in Great Britain.
- A-2. Nielson, Jack N., *Missile Aerodynamics*, McGraw-Hill Book Co., New York, NY, 1960.
- A-3. Anderson, John D., *Fundamentals of Aerodynamics*, McGraw-Hill Book Co., New York, NY, 1984.

## DISTRIBUTION

	<u>COPIES</u>		<u>COPIES</u>
<b>DOD ACTIVITIES (CONUS)</b>		ATTN PROF YAAKOV BAR SHALOM	1
ATTN DR RABINDER MADAN 1114SE	1	ESE DEPARTMENT U 157	
CHIEF OF NAVAL RESEARCH		260 GLENBROOK RD	
BALLSTON TOWER 1		STORES CT 06269-3157	
800 N QUINCY ST			
ARLINGTON VA 22217-5660		ATTN JOSEPH S PRIMERANO	1
		PLANNING CONSULTANTS INC	
ATTN GEORGE SOURIS	1	PO BOX 1676	
ASC ENSSC		DAHLGREN VA 22448	
WRIGHT PATTERSON AFB OH 45433		ATTN STEVE BAUGH	1
		1900 RANDOLPH SE	
ATTN B SCHEINER AMSRL SS SG	1	ALBUQUERQUE NM 87106	
PROJECT OFFICER RADAR BRANCH			
ARMY RESEARCH LABORATORY		ATTN LON CARPENTER	1
2800 POWDER MILL ROAD		FMC CORPORATION	
ADELPHI MD 20783-1145		1 DANUBE DR	
		KING GEORGE VA 22485	
ATTN CODE E29L			
(TECHNICAL LIBRARY)	1	ATTN PHILIP O WEST	1
COMMANDING OFFICER		GEORGIA TECH RESEARCH INSTITUTE	
CSSDD NSWC		ELECTRONIC SYSTEMS LABORATORY	
6703 W HIGHWAY 98		CONCEPTS ANALYSIS DIVISION	
PANAMA CITY FL 32407-7001		ATLANTA GA 30332-0800	
DEFENSE TECHNICAL INFORMATION CTR		ATTN MELVIN BELCHER JR	1
CAMERON STATION		MANAGER MISSILE DEFENSE SYSTEM	
ALEXANDRIA VA 22304-6145	12	GEORGIA TECH RESEARCH INSTITUTE	
		SENSORS AND ELECTROMAGNETIC	
		APPLICATIONS LABORATORY	
<b>NON-DOD ACTIVITIES (CONUS)</b>		ATLANTA GA 30332-0800	
ATTN DR GLENN M SPARKS	1	ATTN ED KAMEN	1
GOVERNMENT ELECTRONIC SYSTEMS		SCHOOL OF ELECTRONIC AND COMPUTER	
DIVISION		ENGINEERING	
GENERAL ELECTRIC COMPANY		GEORGIA TECH RESEARCH INSTITUTE	
MOORESTOWN NJ 08057		ATLANTA GA 30332	



**DISTRIBUTION (Continued)**

	<u>COPIES</u>		<u>COPIES</u>
ATTN SAM BLACKMAN HUGHES AIRCRAFT EO EI MAIL STOP B102 PO BOX 902 EL SEGUNDO CA 90245	1	ATTN DAN FRIEDMAN MARTIN MARIETTA GOVERNMENT ELECTRONICS SYSTEMS MISSILE SYSTEM DESIGN 199 BORTON LANDING RD MOORESTOWN NJ 08057-3075	1
ATTN DR KUO CHU CHANG DEPT OF SYSTEMS ENGINEERING SCHOOL OF INFORMATION TECHNOLOGY AND ENGINEERING GEORGE MASON UNIVERSITY FAIRFAX VA 22030-4444	1	THE CNA CORPORATION PO BOX 16268 ALEXANDRIA VA 22302-0268	1
		<b>INTERNAL</b>	
ATTN WALTER V DIXON CENTRAL SYSTEMS LABORATORY GENERAL ELECTRIC COMPANY BUILDING KW ROOM D214 PO BOX 8 SCHENECTADY NY 12301	1	A20 BEUGLASS A20 LUCAS B05 STATON B30 B32 B32 BLAIR B32 CONTE B32 GENTRY B32 GROVES B32 HELMICK B32 WATSON B35 BAILEY B35 FENNEMORE B35 HARTER E231 E282 SWANSBURG F21 F21 PARKER F21 RYAN F406 F41 F41 FONTANA F41 KNICELY F41 MARTIN F41 TANNER F42 F42 KLOCHAK G23 GRAFF N05 N05 GASTON N07	1 1 1 1 1 20 1 1 1 1 1 1 1 1 1 1 1 3 1 1 1 1 1 1 2 1 1 1 1 2 1 1 1 1 1 1
ATTN DR A T ALOUANI DEPARTMENT OF ELECTRICAL ENGINEERING TENNESSEE TECHNOLOGICAL UNIV TTU BOX 05004 COOKEVILLE TN 38505	1		
ATTN DR PAUL KALATA ECE DEPARTMENT DREXEL UNIVERSITY PHILADELPHIA PA 19104	1		
ATTN GLENN WOODARD SYSCON CORPORATION TIDEWATER DIVISION PO BOX 1480 DAHLGREN VA 22448-1480	1		
ATTN GIFT AND EXCHANGE DIVISION LIBRARY OF CONGRESS WASHINGTON DC 20540	4		

**DISTRIBUTION (Continued)**

	<u>COPIES</u>
N24	1
N24 BAILEY	1
N24 BOYER	1
N24 HANSEN	1
N234 MURREY	1
N24 MILLER	1
N74 GIDEP	1
N92	1
N92 HART	1
N92 LAMBERTSON	1
N92 MCNATT	1
N92 STAMPER	1
N92 FOSTER	1

REPORT DOCUMENTATION PAGE			Form Approved OBM No. 0704-0188	
Public reporting burden for this collection of information is estimated to average 1 hour per response, including the time for reviewing instructions, search existing data sources, gathering and maintaining the data needed, and completing and reviewing the collection of information. Send comments regarding this burden or any other aspect of this collection of information, including suggestions for reducing this burden, to Washington Headquarters Services, Directorate for Information Operations and Reports, 1215 Jefferson Davis Highway, Suite 1204, Arlington, VA 22202-4302, and to the Office of Management and Budget, Paperwork Reduction Project (0704-0188), Washington, DC 20503.				
1. AGENCY USE ONLY (Leave blank)	2. REPORT DATE February 1995	3. REPORT TYPE AND DATES COVERED Final		
4. TITLE AND SUBTITLE Target Tracking Filter Study for Command-All-The-Way Intercepts		5. FUNDING NUMBERS		
6. AUTHOR(s) S. A. Hoffman and W. D. Blair				
7. PERFORMING ORGANIZATION NAME(S) AND ADDRESS(ES) Commander Naval Surface Warfare Center, Dahlgren Division (Code B32) 17320 Dahlgren Road Dahlgren, VA 22448-5100		8. PERFORMING ORGANIZATION REPORT NUMBER NSWCDD/TR-94/343		
9. SPONSORING/MONITORING AGENCY NAME(S) AND ADDRESS(ES)		10. SPONSORING/MONITORING AGENCY REPORT NUMBER		
11. SUPPLEMENTARY NOTES				
12a. DISTRIBUTION/AVAILABILITY STATEMENT Approved for public release; distribution is unlimited.		12b. DISTRIBUTION CODE		
13. ABSTRACT (Maximum 200 words) In command-all-the-way (CAW) interceptor guidance, an interceptor missile receives all acceleration commands from guidance laws in the weapons system at the launch platform, where a radar is used to track both the missile and the target. Since the missile uses no terminal homing in CAW, highly accurate state estimates of both the interceptor missile and the target are needed for the guidance algorithms to provide acceleration commands to the interceptor missile that are sufficiently accurate to ensure intercept of the target. An Interacting Multiple Model (IMM) algorithm is considered for tracking highly maneuvering targets for support of CAW intercepts. The IMM algorithm uses multiple models with model switching governed by an underlying Markov chain to better represent the target dynamics than a single model filter. Thus, using the output state estimate from the IMM algorithm will result in better acceleration commands from the guidance algorithm to the interceptor missile than that of a single model filter. The performance of the IMM algorithm and a single model Kalman filter are compared for both maneuvering and non-maneuvering targets. The simulation was executed for varying intercept ranges. The impact of track filtering on the radar resources required for an intercept and adjusting the proportional navigation gain were also studied through simulation studies and the results are summarized. The IMM algorithm provides for lower miss distances while using less radar resources than that of single model filters.				
14. SUBJECT TERMS command-all-the-way, AEGIS, intercepts, time-to-go			15. NUMBER OF PAGES 86	16. PRICE CODE
17. SECURITY CLASSIFICATION OF REPORT UNCLASSIFIED			20. LIMITATION OF ABSTRACT SAR	
18. SECURITY CLASSIFICATION OF THIS PAGE UNCLASSIFIED		19. SECURITY CLASSIFICATION OF ABSTRACT UNCLASSIFIED		

## GENERAL INSTRUCTIONS FOR COMPLETING SF 298

The Report Documentation Page (RDP) is used in announcing and cataloging reports. It is important that this information be consistent with the rest of the report, particularly the cover and its title page. Instructions for filling in each block of the form follow. It is important to ***stay within the lines*** to meet ***optical scanning requirements***

**Block 1. Agency Use Only (Leave blank).**

**Block 2. Report Date.** Full publication date including day, month, and year, if available (e.g. 1 Jan 88). Must cite at least the year.

**Block 3. Type of Report and Dates Covered.** State whether report is interim, final, etc. \*If applicable, enter inclusive report dates (e.g. 10 Jun 87 - 30 Jun 88).

**Block 4. Title and Subtitle.** A title is taken from the part of the report that provides the most meaningful and complete information. When a report is prepared in more than one volume, repeat the primary title, add volume number, and include subtitle for the specific volume. On classified documents enter the title classification in parentheses.

**Block 5. Funding Numbers.** To include contract and grant numbers; may include program element number(s), project number(s), task number(s), and work unit number(s). Use the following labels:

<b>C</b> - Contract	<b>PR</b> - Project
<b>G</b> - Grant	<b>TA</b> - Task
<b>PE</b> - Program Element	<b>WU</b> - Work Unit Accession No.

**Block 6. Author(s).** Name(s) of person(s) responsible for writing the report, performing the research, or credited with the content of the report. If editor or compiler, this should follow the name(s).

**Block 7. Performing Organization Name(s) and address(es).** Self-explanatory.

**Block 8. Performing Organization Report Number.** Enter the unique alphanumeric report number(s) assigned by the organization performing the report.

**Block 9. Sponsoring/Monitoring Agency Name(s) and Address(es).** Self-explanatory.

**Block 10. Sponsoring/Monitoring Agency Report Number.** (If Known)

**Block 11. Supplementary Notes.** Enter information not included elsewhere such as: Prepared in cooperation with...; Trans. of ...; To be published in... . When a report is revised, include a statement whether the new report supersedes or supplements the older report.

**Block 12a. Distribution/Availability Statement.**

Denotes public availability or limitations. Cite any availability to the public. Enter additional limitations or special markings in all capitals (e.g. NOFORN, REL, ITAR).

**DOD** - See DoDD 5230.24, "Distribution Statements on Technical Documents"  
**DOE** - See authorities.  
**NASA** - See Handbook NHB 2200.2  
**NTIS** - Leave blank

**Block 12b. Distribution Code.**

**DOD** - Leave blank.  
**DOE** - Enter DOE distribution categories from the Standard Distribution for Unclassified Scientific and Technical Reports.  
**NASA** - Leave blank.  
**NTIS** - Leave blank.

**Block 13. Abstract.** Include a brief (*Maximum 200 words*) factual summary of the most significant information contained in the report.

**Block 14. Subject Terms.** Keywords or phrases identifying major subjects in the report.

**Block 15. Number of Pages.** Enter the total number of pages.

**Block 16. Price Code.** Enter appropriate price code (*NTIS only*).

**Block 17-19. Security Classifications.** Self-explanatory. Enter U.S. Security Classification in accordance with U.S. Security Regulations (i.e., UNCLASSIFIED). If form contains classified information, stamp classification on the top and bottom of this page.

**Block 20. Limitation of Abstract.** This block must be completed to assign a limitation to the abstract. Enter either UL (unlimited or SAR (same as report). An entry in this block is necessary if the abstract is to be limited. If blank, the abstract is assumed to be unlimited.